

Testing Hypotheses for Small-scale Beaded Depression Formation on Mars

Supervisor: Dr. Lawrence Plug

Submitted in partial fulfillment of the requirements for EARTH 4200.03.

Rebecca Brunt

B00126800

March 22, 2004

ABSTRACT

Circular to elliptical depressions connected by troughs, visible in Mars Orbiter Camera images, occur in association with small-scale polygons in Utopia Planitia. Possible terrestrial analogues –chains of depressions that occur in high latitude lowlands– are the result of thaw-derived subsidence over ice-wedges, especially at wedge intersections, linked by straight or angular water courses that follow ice wedge troughs. The similar plan-view shape and apparent connectivity between depressions support the hypothesis that Utopia patterns also may form by interactions between patterned ground, ice-rich sediment and flowing surface water. Alternatively, depressions might form by localized subsidence from sublimation of water or CO² ice that initiates randomly or randomly along troughs. To investigate hypotheses for the origin and patterning of depressions, I compare their distribution in Utopia to remote sensing data on topography, thermal inertia and hydrogen content of the shallow subsurface. In addition, the spacing and connectivity along troughs of 24 Mars patterns, each characterized by hundreds to thousands of individual depressions, are tested against three synthetic patterns in which depressions were distributed randomly and randomly along troughs. Mars depressions have diameter 4-100 m and broadly variably separation distances of 5-300 m, compared to ranges of 1-50 m and 5-50 m for beaded depression patterns in northern Alaska. Principally occurring along the SW margin of Utopia (280°W 40°N, 280°W 55°N, 260°W 40°N and 260°W 55°N) on surfaces of Hesperian age, Mars patterns occur in regolith classified as fine grained loose material with dispersed rocks and/or bedrock outcrops. Water ice content of the upper metre of regolith is low, <5% by weight. In comparison, fine grained perennially frozen soils in terrestrial settings typically contain 30-70% water ice, but this may be topped by a drier seasonally frozen layer. Mars features principally occur on shallow slopes, < 1deg, with broad SE exposure. The crisp morphology of meter-scale depressions suggests recent or ongoing formation. Comparisons with synthetic terrains indicate that depressions are not uniformly distributed across polygonal patterns, but instead preferentially occur along downsloping troughs, consistent with a surface flow or subterranean pipeflow connection between beads.

ACKNOWLEDGEMENTS

I realised, while finalizing this paper, that this is the closest I may ever get to being an astronaut. So for helping me achieve one of my dreams since I was small I would like to say my sincerest thank you to all of the people that helped me along the way. To Dr. Lawrence Plug who let me study one of the most interesting topics I've ever encountered and who never set deadlines, to my Mum and Dad who supported me through times, this year, when I thought things would never be brighter, to Lindsay and Aimee and all of the friends who I neglected while trying to stay on top of my work, to the rest of my family who rarely complained that I never visited, to Carl Helmick, because without him I probably would never have figured out how to log onto the computer and to Tracy for being my fellow astronaut.

TABLE OF CONTENTS

| | |
|---|----|
| Abstract..... | i |
| Acknowledgments..... | ii |
| Chapter 1: Introduction to Beaded Patterns on Mars and Definition of Objectives | |
| 1.1: General Statement..... | 1 |
| 1.3: Aims of this thesis: Scientific questions..... | 2 |
| Chapter 2: Permafrost Processes on Earth | |
| 2.1: Permafrost..... | 3 |
| 2.2: Ground ice..... | 3 |
| 2.3: Polygonal ice wedge patterns..... | 5 |
| 2.4: Thawing and depression initiation..... | 9 |
| 2.5: Beaded drainage patterns..... | 10 |
| Chapter 3: Geology, Atmosphere, Climate and Evidence for Water on Mars | |
| 3.1: The geology of Mars..... | 13 |
| 3.1.1: Martian stratigraphy..... | 13 |
| 3.1.2: The general geology of Mars..... | 14 |
| 3.1.3: The Martian regolith..... | 17 |
| 3.2: Evidence for water on Mars: Current climate and water cycle..... | 18 |
| 3.3: Permafrost and frozen ground on Mars..... | 21 |
| 3.4: Polygonal terrain on Mars..... | 24 |
| 3.5: Evidence for liquid water on Mars' surface..... | 25 |
| 3.6: Beaded depression patterns..... | 27 |
| Chapter 4: Methods | |
| 4.1: Mars Global Surveyor and Mars Odyssey..... | 29 |
| 4.2: Selection of regions..... | 30 |
| 4.3: Terrestrial and Martian images..... | 31 |
| 4.4: Extracting data from Martian and terrestrial images..... | 33 |
| 4.5: Models..... | 36 |

| | |
|---|-----|
| Chapter 5: Results and Discussion | |
| 5.1: Qualitative description..... | 37 |
| 5.2: Quantitative description..... | 50 |
| 5.3: Hypothesised mechanisms of formation..... | 54 |
| Chapter 6: Conclusions and Future work | |
| 6.1: Conclusions..... | 60 |
| 6.2: Future work..... | 60 |
| References..... | 62 |
| Appendix A: Aerial photographs used in study..... | 69 |
| Appendix B: Mars Orbiter Camera images used in study..... | 74 |
| Appendix C: Global stratigraphy of Mars..... | 99 |
| Appendix D: Graphs of Mars data..... | 121 |
| Appendix E: Graphs for terrestrial model..... | 134 |
| Appendix F: Graphs for synthetic model patterns..... | 139 |

LIST OF FIGURES

| | Page |
|--|------|
| Figure 1: Terrestrial ice wedge polygon networks..... | 6 |
| Figure 2: Growth of ice wedge..... | 7 |
| Figure 3: Terrestrial beaded drainage..... | 11 |
| Figure 4: Mars topographic shaded relief map..... | 15 |
| Figure 5: Mars thermal inertia map..... | 17 |
| Figure 6: Martian water sources and sinks..... | 20 |
| Figure 7: Mars epithermal neutron flux (hydrogen) distribution map..... | 23 |
| Figure 8: Polygonal networks in western Utopia Planitia..... | 25 |
| Figure 9: Martian gullies..... | 27 |
| Figure 10: Beaded depressions in western Utopia Planitia..... | 28 |
| Figure 11: Measurement method of beaded depression patterns..... | 36 |
| Figure 12: Stratigraphic map of Mars and geographic divisions in Utopia Planitia | 39 |
| Figure 13: Topographic map of study area..... | 40 |
| Figure 14: Deviant circular patterns..... | 41 |
| Figure 15: MOC images present in area 1..... | 42 |
| Figure 16: MOC images present in area 2..... | 43 |
| Figure 17: MOC images present in area 3..... | 45 |
| Figure 18: MOC images present in area 4..... | 46 |
| Figure 19: MOC images present in area 5..... | 47 |
| Figure 20: Martian and terrestrial distribution comparison..... | 52 |
| Figure 21: Graphs of Martian data..... | 53 |
| Figure 22: Schematic of pipeflow and depression growth on Mars..... | 56 |

LIST OF TABLES

| | |
|---|----|
| Table 1: Absolute age ranges of epoch boundaries..... | 13 |
| Table 2: Summary of slope data and morphology of beads..... | 48 |
| Table 3: Summary of beaded depression pattern types and their occurrence..... | 49 |

CHAPTER 1: INTRODUCTION TO BEADED DEPRESSION PATTERNS ON MARS AND DEFINITION OF OBJECTIVES

1.1: General Statement

The theory that water has been an important influence on the geomorphology of Mars, at least sporadically during the past, has been a persistent hypothesis despite difficulties in reconciliation with inferred past climate and geochemical evidence. Atmospheric measurement by the Viking orbiter in the 1970's suggest a small amount of water vapour is currently present in the Martian atmosphere (Jakosky and Farmer, 1982). However landforms seen in Viking images obtained at the same time suggest that water played a key role in surficial processes on Mars at one time. These features include canyon systems and patterned ground that are similar in morphology but orders of magnitude larger than those that form in high latitude regions on Earth (Carr and Schaber, 1979).

It was not until recently through high resolution imaging by the Mars Orbiter Camera (MOC), which can resolve features as small as 2m, that landforms comparable in size and morphology to water related landforms on Earth were discovered. These features include small-scale polygonal fracture networks and patterned ground consistent in size with those that form on Earth, as well as gullies located on crater walls, which suggest water related activity. Accompanying these discoveries is the gamma ray signatures from the Gamma Ray Spectrometer (GRS) aboard Mars Odyssey that have identified a near surface layer of ground ice, at least 1m thick, distributed unevenly around the planet.

In western Utopia Planitia, in the Northern Plains of Mars a regular pattern of depressions is associated with the small scale polygons observed in MOC images

(Costard and Kargel, 1995; Seibert and Kargel, 2001). Morphologically this pattern is similar to beaded drainage, a pattern of interconnected pools that form in periglacial regions on Earth. Beaded drainage occurs in periglacial regions due to accelerated melting at the intersection of two or more ice wedges, a ground ice structure characteristic of ice-rich permafrost soils.

Beaded depression patterns, observed in MOC images, present an opportunity for quantitative comparison of Martian and terrestrial patterns that are indicative of the interaction of near-surface water with ice-rich soils and for testing hypotheses for Martian beaded depression formation through comparison of terrestrial and synthetic models.

1.2 Aims of this thesis: Scientific questions

Aims of this thesis include; testing hypotheses for the formation of beaded depression patterns on Mars through comparison of Martian patterns with terrestrial and synthetic models, as well as providing the first quantitative analysis of terrestrial beaded drainage patterns that commonly occur in periglacial regions.

CHAPTER 2: PERMAFROST PROCESSES ON EARTH

2.1 Permafrost

Permafrost is defined as soil, unconsolidated deposit, or bedrock at variable depth beneath the surface of the earth in which temperature has been below freezing for more than 2 years (Muller, 1945). Permafrost is defined exclusively on the basis of temperature, irrespective of composition, texture, degree of induration, water content or lithological character and represents a thermal condition of negative heat balance at the surface of the Earth in which complete thawing of the ground frozen in the previous year does not occur. Between the permafrost and the ground surface lies a layer of soil that seasonally thaws and refreezes called the active layer. Thickness of the active layer varies in depth annually depending on climatic conditions (Muller, 1945). The bottom of permafrost occurs at a depth where internal heat compensates for the temperature difference between the ice and the melting point (Lachenbruch, 1968).

Permafrost occurs in periglacial regions where mean annual near-surface ground temperatures are below 0 °C (Muller, 1945). Regions that fulfill the temperature requirement are limited to the high latitude and high altitude regions of the Earth. Not all cold environments have perennially frozen ground, as permafrost represents the delicate balance of many dynamic factors (French, 1996).

2.2 Ground ice

In permafrost regions the water content of soil, primarily present as ice, influences landforms and relief. Ground ice is a general term that refers to a broad range of ice in the ground regardless of amount, configuration or genesis (ACGR, 1988). Ice may be contained in pores, cavities, voids and/or other openings in the soil. Ice structures can

range from small veins and flakes of ice to massive ice lenses that can be tens of meters wide (Mackay, 1972). Quantitative parameters to describe ground ice include the ice content, which is the weight of ice to dry soil expressed in a percentage, and excess ice contained within a soil. Excess ice is measured as the volume of supernatant water present if a vertical column of frozen sediment were thawed. Soils with less than 50% ice are considered to have low ice content. Soils with more the 50% ice are considered to have a high ice content (Murton and French, 1994).

Ground ice concentration is greatest near the permafrost table and generally decreases with depth, a distribution that arises because most ice-enrichment processes, described later, occur in the upper 2 to 10m of the soil. The high ice contents near the surface are sustained due to low vapour pressure of ice relative to water (Williams and Smith, 1989), which has little dependence on temperature. Ground ice principally occurs in northern latitudes and despite low annual precipitation in these areas, where most permafrost forms, ground ice is maintained because the low vapour pressure of ice means that minimal moisture is lost to the atmosphere.

Structures of frozen sediment and/or ice which exhibit specific characteristics are called cryostructures (Murton and French, 1994). There is, however, no standard classification of ground ice. One approach is to classify ground ice by the source and transportation mechanism of water to the site of the ground ice structure (Mackay, 1972). The source of the water is generally from the surface, with water percolating through the soil solely under the influence of gravity. Surface water is present when regional climate rises above the melting point. Water percolating through supersaturated soil must do so through cracks or other spaces in the soil forming what is called vein ice. Water may also be supplied to a freezing front by elevated hydrostatic pressure in adjacent soils which

squeezes the water into a central space. This process forms a relatively pure body of ice, called intrusive ice. Subsurface water may also be drawn to the ice-water interface by capillary action. This process, due primarily to frost heave, is actually caused by the lower pressure of water at the interface. In essence water is drawn down a thermal gradient, toward the freezing body. The ice formed by this movement is called segregation ice (Jumikis, 1966).

Another approach to classification of ground ice structures is based on morphology of the ice. The most recognizable ground ice structures are ice wedges, which form distinctive polygonal patterns. Other ground ice structures include pore ice, pingo ice, sill ice, vein ice, and open and closed cavity ice. A genetic classification of ground ice modified from Mackay (1972) relates these ground ice structures to the origin and transfer mechanism of water that was discussed above.

2.3 Polygonal ice wedge patterns

Periglacial regions in high latitude areas of Earth are characterised by the presence of permafrost and ground ice, which influences the surface relief and geomorphology (French, 1996). Polygonal patterns of ridges, created by the deformation of the surrounding soil by ice wedges, are typical in periglacial regions. Ridges created by the deformation of the soil provide the distinctive surface relief which make ice wedges one of the most readily identifiable ground ice structures in plan view (fig.1).

The formation of ice wedges takes place in areas where the surface is stable, forming epigenetic ice wedges, or where sediment is aggrading, forming syngenetic ice wedges (Dostovalov and Popov, 1966). In measurements of fracture in coexisting ice wedges in the western Canadian Arctic, crack formation occurred when the ground

surface temperature dropped by at least 1.8°C per day for 4 consecutive days (Mackay, 1993). Few measurements have been undertaken; these criteria for cracking probably are dependent on regional soil conditions and soil composition which may depress the freezing temperature and complicate the cracking process. Absolute temperature is also important because ice rich frozen ground is more brittle at low temperatures; in measurements cracking can occur if ground temperatures are below -3 to -4°C (Mackay, 1975).



Figure 1: Plan view of ice wedge polygon network in ice-rich permafrost soil, Arctic Coastal Plain, Alaska.

Saturated soil expands upon freezing until the majority of the water in the soil is frozen (Lachenbruch, 1962). It is at this point that thermal contraction occurs. With little elasticity in the frozen soil the tensile stress easily exceeds the tensional strength, which causes the soil to crack in a characteristic manner. Cracks propagate downward vertically

and in a normal direction to a horizontal plane. Planes of weakness created by the addition of ice to existing cracks allow seasonal reopening along the same plane rather than the formation of new cracks (Mackay, 1989).

The seasonal addition of melt water and hoarfrost in the cracks results in the growth of ice wedges horizontally as well as vertically. Expansion of the ice wedge puts pressure on the adjacent soils and vertical deformation of the soil occurs. Characteristic ridges are formed and a pseudo-depression evolves above the ice wedge (fig. 2) (Mackay, 1975). However not all ice wedges crack annually and therefore the size of the ice wedge does not necessarily correspond to relative age (Black, 1973).

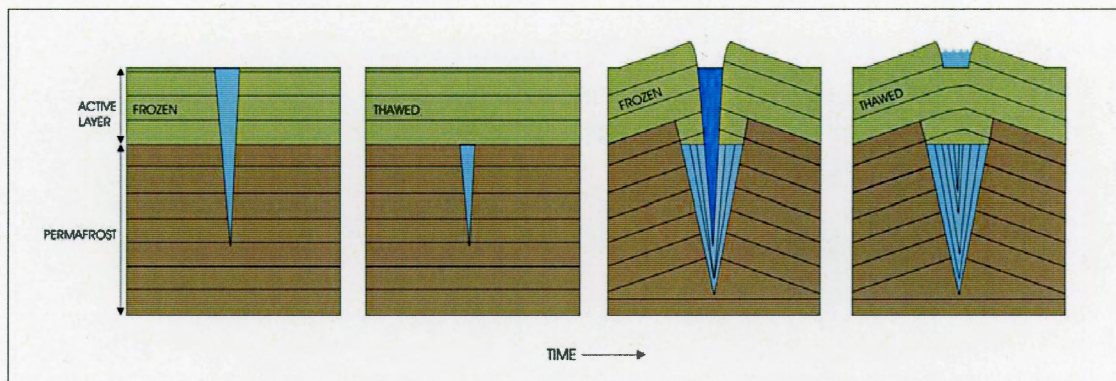


Figure 2: Schematic representation of growth and consequent deformation of the surrounding sediment through time of an ice wedge in ice-rich permafrost. Initiation of an ice wedge occurs by the creation of a tension fracture. Water then infiltrates into the fracture in the active layer and causes lateral compression as well as vertical growth vertically. Eventually the ice wedge reaches the permafrost where it is preserved until an upset in thermal equilibrium causes the active layer to migrate downward. Fractures are opened semi-annually along a plane of weakness created by the ice wedge and repeated addition of hoarfrost and precipitation into the fracture allows the ice wedge to continue growing (after Mackay, 1975; 1979).

At the surface ice wedges may reach 4m in width and typically extend vertically to depths of 3 to 4m (French, 1996). Wedges formed in constantly aggrading soil typically taper with depth and have near vertical, sub-parallel foliations defined by cleavage planes, air bubbles or sediment (Shumskiy and Vtyurin, 1963), the latter due to entrapment of sediment as water is drawn to ice through unconsolidated material.

In plan view at the ground surface, ice wedges form polygonal patterns because tension is released normal to cracks rather than parallel. Individual polygons range from 10m to 100m in diameter, depending on the strength of the soil (greater tensile strength gives larger polygons) and magnitude of stress from cooling (Lachenbruch, 1962, Plug and Werner 2001). Ice wedge intersections are predominantly orthogonal because secondary fractures adopt orientations perpendicular to the maximum residual stress around earlier cracks (Lachenbruch, 1962, Plug and Werner, 2001), however rectangles may form as a result of an initial asymmetry (Lachenbruch, 1962, 1966). The resulting pattern is orthogonal, hexagonal or intermediate between the two with relative proportions dependent on heterogeneity of stress and substrate properties. The spacing and intersection types of networks also vary as networks age over thousands of years, even under uniform conditions as the network explores permutations in the order of ice wedge fracturing (Plug and Werner, 2002)

Two morphologically distinct types of networks arise by differing differential movement between the active layer and the top of the permafrost: a high centered type and a low centered type (Mackay, 1980). Low centered polygons commonly have elevated rims created by deformation of sediment surrounding the growing wedge. Troughs, which run between the center and the rim of the polygon lie above the ice wedge and commonly fill with standing water in warmer months due to high water tables in active layers in most poorly drained lowlands. High centered polygons are thought to occur in areas with better drainage than areas where low centered polygons form making standing water pools ephemeral. The retention of standing water above ice wedges in low centred polygons make them more susceptible than high centred polygons to the formation of permanent drainage channels (Shumskiy and Vtyurin, 1966). Preferred

thawing occurs above ice wedge intersections creating small pools and integrated drainage between these pools forms beaded depression patterns (Hopkins et al., 1955).

2.4 Thawing and depression initiation

Thermokarst—the melting and subsequent collapse of permafrost soils— is an important contributor to the relief of both continuous and discontinuous permafrost regions (French, 1996). Melting of permafrost is initiated by disruption of thermal equilibrium and an increase in the depth of the active layer (Mackay, 1970). Mechanisms of thermal disruption include geomorphic changes such as slumping, the presence of standing water, climate amelioration, or as a result of a change in the vegetation due to fires. All of these mechanisms have a similar effect; the readjustment of the active layer due to ground temperature fluctuations which causes thermal disequilibrium and the thawing of permafrost. As a result of thawing, excess water is evacuated and the ground subsides. Evacuated water may pool in the derived depression, leading to enhanced thawing around the depression because water, which has relatively low albedo, is warmed by solar radiation (Williams and Smith, 1991).

The magnitude of morphological change associated with thawing, usually subsidence of permafrost, depends on the degree of super-saturation of permafrost and the new equilibrium depth of the active layer. The degree of super-saturation of soils is classified as thaw sensitive or thaw stable (Van Everdingen, 1979). Those soils which are thaw stable contain little to no excess ice and retain their mechanical integrity upon evacuation of melt water.

Disruption of thermal equilibrium in low-centred ice wedge polygon terrain favours accelerated melting at the intersection of 2 or more ice wedges due to the

relatively high concentration of ice and presence of standing water in the area (Hopkins et al., 1955). Growth of small pools creates a positive feedback system in which the water present in the pool preferentially absorbs solar insolation due to its low albedo, accelerates the melting of the ice wedge intersection which in turn supplies more water to the pool (Williams and Smith, 1991).

2.5: Beaded drainage patterns

The thermokarst of ice wedge intersections causes compaction of thaw sensitive soil and forms depressions which commonly contain standing water. The pools are hydrologically connected to one another as the material above the single ice wedge also thaws and subsides, though not to the extent as at the intersections. When pools are integrated into one drainage system it is called beaded drainage (fig. 3). These form characteristic patterns of minor streams in many lowland regions underlain by perennially frozen ice rich soil and ice wedges (Hopkins et al., 1955) in continuous to discontinuous permafrost regions on Earth. Though ice wedges may form in areas of varying grain size, beaded drainages appear to be restricted to those areas where near-surface permafrost is ice rich and the non ice component is composed of peat or silt. Often these features are the predominant low-order streams in a region and hold active flow during the thaw season (Hopkins et al., 1955).

Pools in beaded drainages typically are shallow, less than 3m in depth, and circular to elliptical in plan view with diameters of 3 to 200m (Hopkins et al., 1955). Pool margins are sharply defined by steep walls and this can be used as criteria to distinguish beaded drainage from a similar phenomenon called swamp drainages which occur in non-permafrost regions (Hopkins et al., 1955). Troughs which connect pools range in length

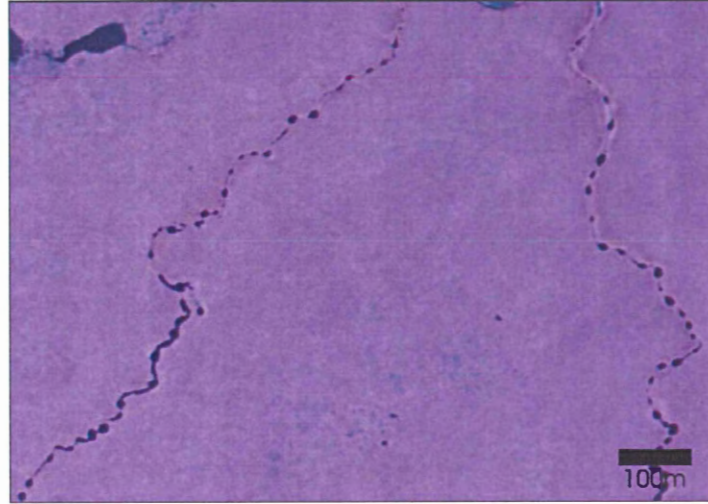


Figure 3: Beaded drainage in ice-rich permafrost soil, Arctic Coastal Plain, Alaska.

from 3 to 50m and because they follow the path of the ice wedges, are usually straight or sharply angled.

A distinguishing feature of beaded drainages is the non-random alignment of pools with the downslope dip of local topography and the clear interconnections between pools. In other forms of periglacial patterns, coordination between individual features is not evident. For example sorted circles display a high degree of ordering and pattern development with included circles, but little to no patterning at the larger scale of many sorted circles. Similarly features created by thermokarst of patterned ground are apparently random in distribution (i.e. thawlakes and retrogressive slumps). The patterning of beaded drainages, though not yet explored quantitatively, may be diagnostic of specific ice-thawing/flowing water processes that give rise to their formation.

Regularly ordered beaded drainage patterns observed in the Arctic Coastal Plain and North Slope of Alaska are a result of thermokarst of the ordered ground ice structures that compose ice wedge polygons. Though the thawing of structures such as lens ice may

form depressions similar in size and shape to individual beads, the pattern of regularly spaced beads, with interconnecting channels, can be best explained by the preferential melting of regularly spaced intersections of ice wedge polygons (Hopkins et al., 1955).

CHAPTER 3: MARTIAN GEOLOGY, ATMOSPHERE, CLIMATE AND EVIDENCE FOR THE PRESENCE OF WATER

3.1: The Geology of Mars

3.1.1 Martian Stratigraphy

The geological history of Mars has been divided into three epochs based on the crater density of specific areas of Mars' surface seen in images (Smith and Elston, 1971). During the early formation of the solar system the proto-planets underwent heavy bombardment by smaller planetesimals and debris still orbiting the proto-sun after the planets had coalesced. As planets and larger stellar bodies assembled through gravitational collapse, impacts on existing bodies decreased. Using the frequency of impacts as a measure of time, the history of Mars has been divided into three broad time periods or epochs representative of cratering history (Carr, 1996). Several different models for absolute time boundaries of these periods have been proposed based on the lunar impact record which is constrained by radiometric dates on returned samples (Table 1).

| Noachian-Hesperian boundary | |
|-------------------------------------|--|
| Crater densities | 200 > 5km in diameter/ 10^6 km ² 25 > 16km in diameter/ 10^6 km ² |
| Absolute age | 3.5 - 3.8 Gyr |
| Hesperian-Amazonian boundary | |
| Crater densities | 400 > 2km in diameter/ 10^6 km ² 67 > 5km in diameter/ 10^6 km ² |
| Absolute age | 1.8 - 3.5 Gyr |

Table 1: Absolute age range of epoch boundaries (after Carr, 1996).

The earliest of the Martian epochs is the Noachian, which defines the time between the formation of the planet to 3.5-3.8 billion years before present. During the

Noachian volcanic activity and crustal deformation was high. The Tharsis bulge may have been created through the static position of the crust over a hotspot and the elevated crust established a South to North sloped valley pattern (Phillips et al., 2001), still apparent in surficial features. Noachian surfaces that remain are characterised by heavily cratered terrains such as those in the Southern highlands (Tanaka et al., 1992).

The Hesperian epoch defines the time period between 3.5-3.8 and ~1.8 billion years before present and is predominantly represented by outcrops in the Northern plains (Scott and Condit, 1977). During the Hesperian volcanism and bombardment continued, followed by resurfacing of the planet and tectonic features emerged due to uplift hypothesised to be associated with inter-layered sedimentary and volcanic units (Tanaka et al., 1992).

The Amazonian, the most recent Martian Epoch, represents the time from ~1.8 billion years before present to the current time. During the Amazonian epoch volcanism gradually decreased and erosional processes dominated (Tanaka et al., 1992). Impacts also decreased in frequency, as in the rest of the solar system, creating the relatively smooth Amazonian surfaces visible today. The Northern plains are hypothesised to be the youngest large surface on Mars due to the small number of craters present on its surface (Smith and Elston, 1971).

3.1.2: The General Geology of Mars

Separating the relatively flat Northern lowlands and the cratered Southern highlands is a striking global scale feature called the dichotomy boundary, an approximately 6km change in mean elevation (Smith and Zuber, 1996). Speculation about the relationship between the two hemispheres centres on two opposing theories; the

concept of a relic Martian ocean (Head et al., 1999) and the loss of material due to large impacts early in Martian history (Wilhelms and Squyres, 1984).

High resolution images from Mars Orbiter Camera show evidence that the heavily cratered terrain in the Southern hemisphere has been modified throughout history by wind, water and volcanic activity (Hynek and Phillips, 2001). The northern hemisphere is predominantly composed of flat plains that contain features such as Hesperian volcanic flows and tectonic ridges (Withers and Neumann, 2001), indicative of sediment transport which is also suggested by the recent identification of buried craters in northern lowlands using Mola derived topography (Frey et al., 2001).

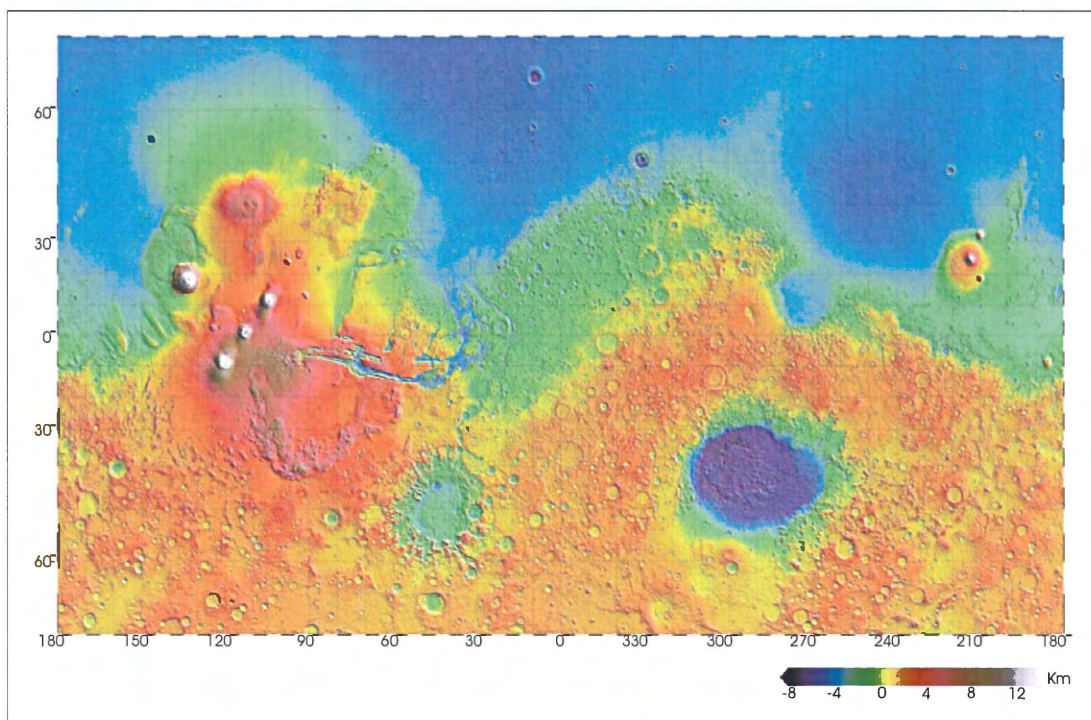


Figure 4: Topographic shaded relief map derived from MOLA data (after Smith et al. 2001)

Though no volcanoes exist in the lowland regions of Mars the Southern highlands, near the dichotomy boundary, contain some of the largest volcanoes in the

solar system (Cattermole, 2001). Volcanoes such as Olympus Mons comprise small parts of large volcanic provinces spread around Mars. Volcanic provinces near the dichotomy boundary, such as the Tharsis and Elisium complexes, may have been sources of lava that once flowed into the Northern plains (Zuber, 2001). The Tharsis complex is approximately 400km from north to south and 3000km from west to east and lies an average of 10km above datum (lacking a sealevel, Mars' datum is defined as 0.06 MPa atmospheric pressure). Significant mass imposed on the crust by the Tharsis volcanic province probably has caused crustal flexure in the surrounding areas, which has been accommodated by large scale tectonic features such as the Valles Marineris canyon complex, a graben structure extending >4500km around Mars' equator. Many of these tectonic features show extensive erosion and are heavily cratered indicating an origin during the Noachian epoch of Martian history.

The topography of Mars has recently been imaged by the Mars Orbiter Laser Altimeter (MOLA) aboard Mars Global Surveyor (Smith et al., 2001). High resolution topographic maps from MOLA (fig. 4) allow small scale features to be resolved as well as the subtle subsurface expression of features that were not previously resolvable, such as buried impact craters in the Northern plains (Frey et al., 2001). Through the use of MOLA data it has been possible to quantify the relief of the Mars' surface and constrain the processes through which it has been shaped. Although MOLA data, limited by a footprint of 128 pixels per degree, cannot resolve features on the scale of beaded drainages or thermokarst pits, it can be used to derive local slope angles down to a scale of 1m vertically and 300m horizontally (Smith et al., 2001). In the relatively flat Northern plains small scale variation in the slope of an area may have a great effect on the preferred orientation direction of the patterns. I return to this issue in the Methods and

Discussion chapters.

3.1.3: The Martian regolith

The composition of the Martian surface layer, resolved through bulk composition data retrieved from spectral analysis on the Viking missions, has been reconciled with iron rich rocks such as hematite as well as possible carbonates and silicates (Singer et al., 1979; McSween, 1994). Thermal Emission Spectrometer (TES) aboard MGS has provided a detailed description of the composition of the Martian regolith. Spectral analyses from TES are consistent with a Martian regolith composed of detritus of pristine basalt and andesite as well as their intermediates (Banfield et al., 2000).

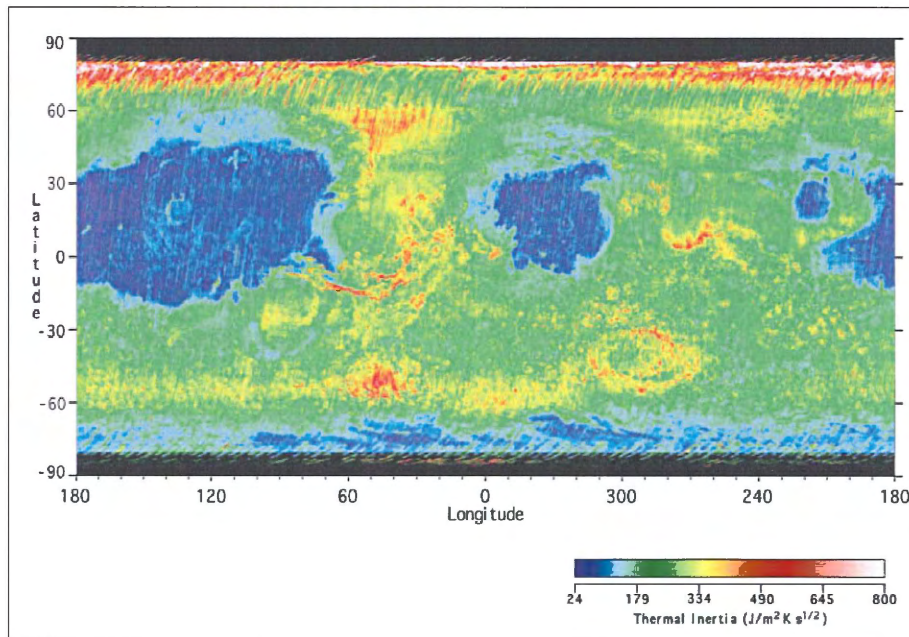


Figure 5: Global thermal inertia map. Lowest thermal inertia (purple to dark blue) represents loose, fine surface dust and very few rocks. Medium thermal inertia (green to yellow) represents a combination of coarser loose particles, crusted fines, a fair number of scattered rocks, and/or perhaps a few scattered bedrock outcrops. High thermal inertia (red to white) could be a combination of: coarse sand, dune sand, strongly-crusted fines, abundant rocks, and/or scattered bedrock exposures (after Putzig et al., 2003; Mellon et al., 2002).

TES also provides global data on the grain size of the top 3 centimetres of regolith (fig. 4). Grain size measurements are derived from thermal inertia, and comprehensive maps of grainsize distribution now exist (fig. 5). The distribution patterns of the regolith on the Martian surface show complex relationships still not fully understood. However small scale variability in grain size distribution has revealed that what was once thought to be a relatively homogeneous surface layer is actually a complex mosaic of fine to very coarse grained mixtures of sediment that reflects origin of regolith in specific areas (Jakosky et al., 2000).

Though planetesimal impacts occur infrequently on Mars now, the lack of plate tectonics and widespread volcanism over the last ~3.5 billion years means that both crater and ejecta from early impacts are still present on Mars' surface as a mantling layer, much like Earth's moon. Current thought holds that large scale erosion and extensive modification of uplifted areas of Mars, such as the Southern highlands, have also contributed to the regolith present on the Martian surface, particularly in the Northern Plains (Smith et al., 1999).

3.2: Evidence for water on Mars: Current Climate and Water Cycle on Mars

Recently questions concerning the presence of water on Mars have turned from if there is water, to how much and in what form does it exist? Atmospheric measurements by the Viking orbiter (1976) and remote sensing of visible polar ice caps makes the presence of water on Mars undeniable (Farmer et al., 1977). However the volume, distribution, sinks and sources of modern global water throughout the polar caps, regolith and atmosphere remain pertinent questions. Moreover there is strong evidence that liquid water played a key role in shaping Martian landscapes in the recent past

(Malin and Edgett, 2000). Determining the mechanisms for, and duration of a warm and wet early Mars remains a research focus.

At present a column of Martian atmosphere contains, on average, an amount of water equivalent to a layer 10 μ m thick, as estimated by the Mars Atmospheric Water Detector on the 1976 Viking mission (Farmer et al., 1977) and more recently by TES aboard MGS (Jakosky et al., 2000). Above the Northern cap, which holds significant water ice, the atmospheric column contains an amount of water equivalent to 100 μ m compared to 13 μ m over the Southern CO₂ rich cap (Jakosky and Farmer, 1982).

Springtime increases in water vapour near the equator are greater than can be supplied by the northern seasonal cap suggesting the regolith also acts as a seasonal source and sink for water vapour (Carr, 1996). Seasonal and spatial variation of water vapour content in the Martian atmosphere show that exchange occurs seasonally (fig. 6) between reservoirs of water vapour (Jakosky and Phillips, 2001). Reservoirs include the shallow subsurface of the regolith as well as the polar caps and atmosphere. Exchange between the regolith and the atmosphere necessitate the presence of an active layer, analogous to seasonally frozen and thawed terrestrial active layers, which is seasonally enriched and depleted in water vapour and/or ice (Carr, 1996).

Over long time scales, water may exchange between the atmosphere and regolith owing to climate changes induced by variations in Mars' orbit and axial tilt (Toon et al., 1980 and Ward and Rudy, 1991). Recent destabilisation of ground ice and consequent release of water vapour may be associated with climate changes accompanying the obliquity changes from 15° to 35° during the past (Ward and Rudy, 1991), which operate on time scales of 10⁵ to 10⁶ years (Ward, 1979). During higher obliquity, atmospheric pressures and temperatures on Mars may rise from present values

making the short term existence of liquid water at the surface possible with mid to northern latitudes as areas where melting would be most intense (Costard et al., 2002). Thawing of subsurface reservoirs would release liquid water which would flow from

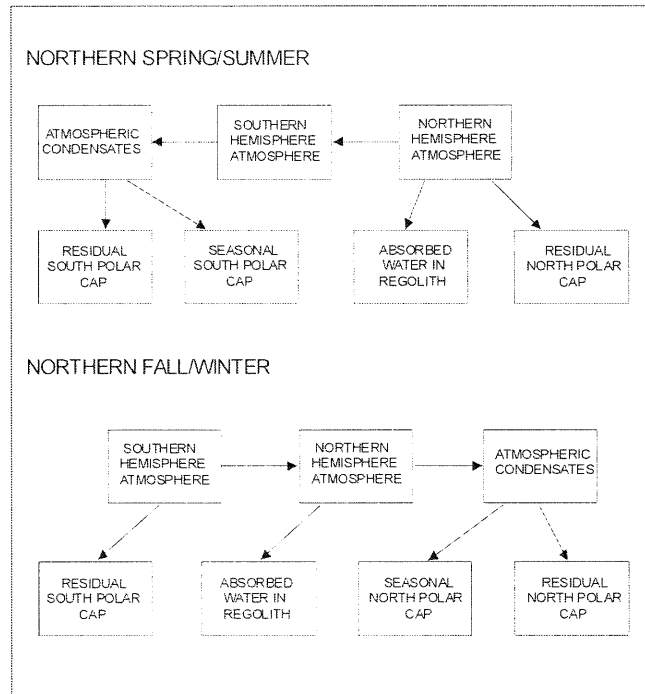


Figure 6: Hypothesised sources and sinks of Martian water. Arrows indicated hypothesised exchange of water vapour between reservoirs currently occurring on Mars (after Carr, 1996).

areas nearest to the cryosphere interface in a process called sapping or seepage (Malin and Edgett, 2000). Although some groundwater recharge models have been proposed for the Martian subsurface, such as hydrothermal convection (Squyres and Kasting, 1994), the lack of hydrogen in some areas suggests that no recharge has occurred since recent obliquity highs. Along with melting ground ice, during high obliquity, sublimation of the Northern and Southern polar caps would have created a much warmer Mars in the past by supplementing the Martian atmosphere with small concentrations of CH_4 and NH_3 (Squyres and Kasting, 1994).

3.3: Permafrost and frozen ground on Mars

The current search for water on Mars has gone underground. The reservoirs on Mars which can be directly analysed including the atmosphere and Northern polar ice caps hold little water (Carr, 1996). Therefore, if Mars retains significant water the reservoir must be beneath the surface. Short of physical exploration of the Martian subsurface, surficial evidence of subsurface processes must substitute for boreholes and seismic data. One line of recent evidence for the presence of ground ice comes from the gamma ray spectrometer aboard the Mars Global Surveyor, which measures hydrogen concentration in the upper metre of Martian regolith (Boynton et al., 2002). Another line of evidence is Martian surface features with analogues from ice-rich periglacial regions of Earth (Carr and Schaber, 1979).

On Mars most landforms used as evidence for the presence of ground ice occur at latitudes polewards of 40°, where ice is expected to be stable (Fannale et al., 1986). In these areas patterns such as lobate debris aprons, softened terrain, rampart craters, outflow channels, valley systems and patterned ground suggest the former presence of ground ice or water (Squyres and Carr, 1986). Lobate debris aprons are the accumulation of erosional debris at the base of steep escarpments and they occur wherever steep slopes are present in the appropriate latitudinal range (Squyres, 1979). Debris aprons have been attributed to gelifluction and/or frost creep due to the presence of entrained ice (Carr, 1996). One hypothesis for the presence of ice is that it is derived from the atmosphere through ice-dust interactions (Luchitta, 1984); another is that ice derives from ground ice by sapping or scarp collapse (Squyres, 1978). Viscous flow of material with entrained subsurface ice is also believed to be the mechanism responsible for the degradation of surface features ('terrain softening') which creates the rounded

features found in the mid to high latitudes, a mechanism which requires subsurface material with the rheology of ice-rich frozen ground (Squyres and Carr, 1986).

Martian crater ejecta display morphology distinct from comparably sized craters on the moon, a distinction hypothesised to arise because of ice or water-saturated Martian regolith. Small craters, <20km in diameter, have lobes with low ridges or escarpments at the outer edge. These are called rampart craters and appear to form by fluidized transport of ejecta material (Carr et al., 1977). Not all craters of this size have rampart morphology, and those with a diameter less than a few kilometres never have rampart morphology. Variability in morphology of large craters may be due to variable distribution of ground ice in Mars' subsurface and smaller craters are not large enough to penetrate the cryosphere and release sufficient liquid into the atmosphere or subsurface (Carr et al., 1977)

Networks of anastomosing valleys are prevalent in the Southern highlands, while the dichotomy boundary is characterised by large outflow channels and retreating erosion. Small branching valleys in which tributaries merge downstream are common in the southern plains. Characteristic morphology includes U shaped valleys with flat floors and steep walls. Small valley networks typically do not exceed 200km in length and a few kilometres in width (Pieri, 1976). Longitudinal ridge-like features on valley floors are interpreted as resulting from the removal of material from the channel by mass wasting aided by groundwater seepage into the mass wasted debris (Carr, 1995).

Remote sensing instruments on Mars Global Surveyor (MGS) and Mars Odyssey, which reached mapping orbit in 1997 and 2001 respectively, have supported inferences on composition of the shallow subsurface including the proportion of water ice. Hydrogen abundance has been estimated by the Gamma Ray Spectrometer (GRS)

(fig. 7). Deficiencies of epithermal neutrons indicate that hydrogen is abundant in the top 1 to 2 metres of the subsurface (Boynton et al., 2001). Terrain pole-ward of 60°, in both the Northern and Southern hemispheres, are identified as hydrogen rich

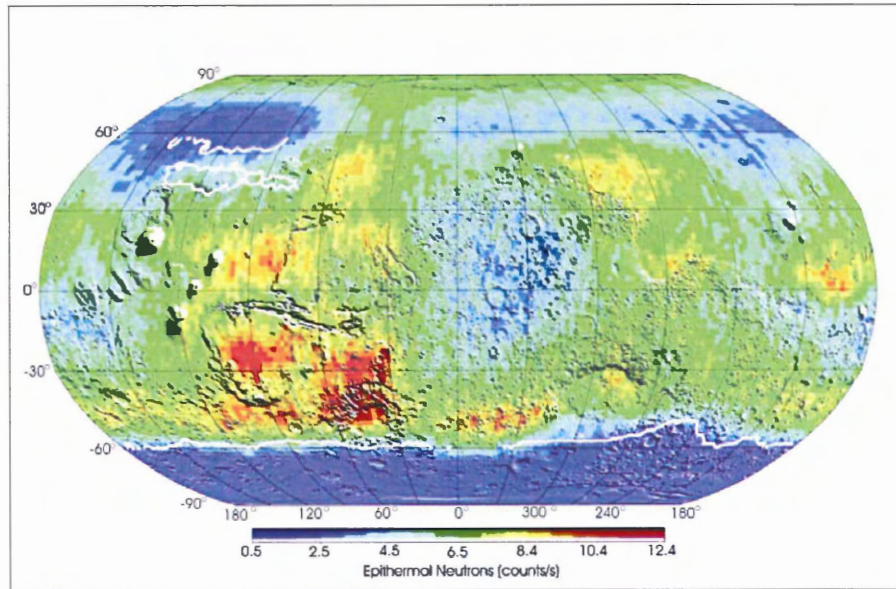


Figure 7: Map of epithermal neutron flux from the GRS. Low epithermal neutron flux is indicative of high hydrogen content (after Boynton et al., 2002).

(Mitrofanov et al., 2002; Feldman et al., 2002). Abundant hydrogen is believed to be present in the form of buried ground ice or ice-rich permafrost beneath a layer of ice-poor soil (Boynton et al., 2002). H₂O content of the lower ice-rich layer is estimated as approximately 35 +/- 15% by weight (Boynton et al., 2001). Hydrogen is expected to be present in the form of water ice because the amount of measured hydrogen is too large to be accommodated by the alteration of most rock forming minerals, and alteration does not account for the observed contrast between concentrations in upper and lower layers. Moreover, the consistency of observed hydrogen with areas where water ice is expected to be stable suggests that hydrogen is present in the form of water ice rather than

chemically bound in minerals (Boynton et al., 2001).

3.4: Polygonal terrain on Mars

Giant polygons were first observed on the Martian surface in Mariner 9 and Viking Orbiter images. The diameter of giant polygons is in the range of 30km (Lucchitta et al., 1986), while the width and depth of the troughs reach dimensions of 2km and 30m respectively (Hiesinger and Head, 1999). Although analogous in shape to those that form in the periglacial regions of earth, they are, on average, several magnitudes of order larger in diameter than the terrestrial examples (Hiesinger and Head, 2000). Originally found in Utopia Planitia, in the Northern plains of Mars, giant polygons are believed to have formed during the late Hesperian as a result of outflow channels (Lucchitta et al., 1986). Their anomalously large size was interpreted to reflect thermal contraction mechanisms (Carr and Schaber 1979), however the size of Martian examples is probably too great to be accounted for by thermal contraction. Crack depth, which sets minimum spacing by reducing stress in a zone proportional to depth (Plug and Werner, 2001), would need to be up to 100km-far beyond the depth that a seasonal temperature change or even climate change would penetrate.

Early high resolution Viking Orbiter and Viking Lander 2 images also showed polygons of much smaller scale ranging in diameter from 10m (small-scale polygons) to 300m. Original explanations for small scale polygons included lava cooling, desiccation of wet sediments and thermal contraction of ice rich soils analogous to permafrost regions on Earth (McGill and Hills, 1992). Comparison of small scale polygons on Earth and on Mars suggest the morphology of small-scale polygons is analogous to terrestrial polygons which form through permafrost processes (Mellon,

1997; Seibert and Kargel, 2001; Yoshikawa, 2001). Unlike giant polygons, the dimensions of smaller polygons are consistent with a thermal contraction theory (Mellon, 1997).

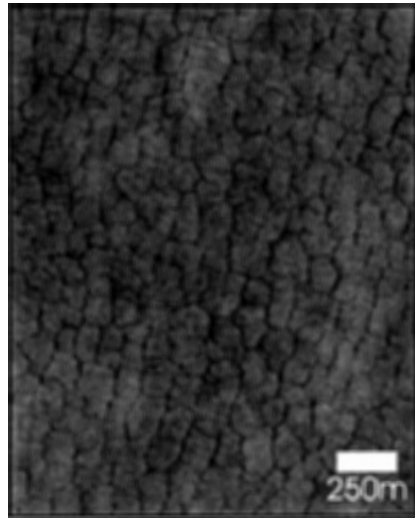


Figure 8: Polygonal networks in western Utopia Planitia. MOC image E02-01703.

Other mechanisms proposed for the formation of small scale polygons includes desiccation and shrinking of a muddy substrate. However the close association of the observed small scale polygons with other features interpreted as permafrost structures suggests that ice wedges are responsible for their formation (Seibert and Kargel, 2001).

3.5: Evidence for liquid water on Mars' surface

Since the first images beamed back by Mariner 9, images of Mars' geology and geomorphology have presented increasingly strong evidence that Mars has undergone extensive shaping by liquid water at least sporadically during its history.

Advances in remote sensing have provided some constraints on the volume and fluxes for some reservoirs thought to currently store water, including the atmosphere, shallow regolith and polar caps are measured by Mars Odyssey and Mars Express. Moreover discovery of youthful-appearing landforms, hypothesised to form only through fluid transport, has stirred interest in the possibility of recent or current presence of liquid water on Mars.

Channels and valleys were first identified in Mariner 9 images of Martian surface (Pieri, 1976). Outflow channels present near the dichotomy boundary may reach tens of kilometres across and hundreds to thousands of kilometres in length (Kieffer et al., 1992). A variety of bedforms are prevalent on the floors of many outflow channels and are proposed to be indicative of the stripping away of surface materials due to high velocity turbulent fluid flow (Baker and Milton, 1974). Craters and softening of the margins of the channels implies that these features were formed early in Mars history, when impacts occurred more frequently. Based on these features alone, the possibility of liquid water on Mars is restricted to the very distant past.

Liquid-water related landforms on Mars were observed in MOC images that suggested the more recent activity of liquid water (Malin and Edgett, 2000). The gullies (fig. 8) observed in 120 locations, mostly in the mid latitudes of the southern hemisphere, are located on isolated slopes, usually on crater walls. Gullies consist of head alcoves, main and secondary channels and depositional aprons, all interpreted as evidence of fluid flow. Due to the lack of visible evidence of overland flow feeding the gullies, it was suggested that the gully systems are fed by fluid seepage from aquifers truncated by crater walls. Superposition of these features on youthful surfaces, such as crater rims, and their uncratered appearance suggests gully systems are presently or recently active (Malin

and Edgett, 2000).

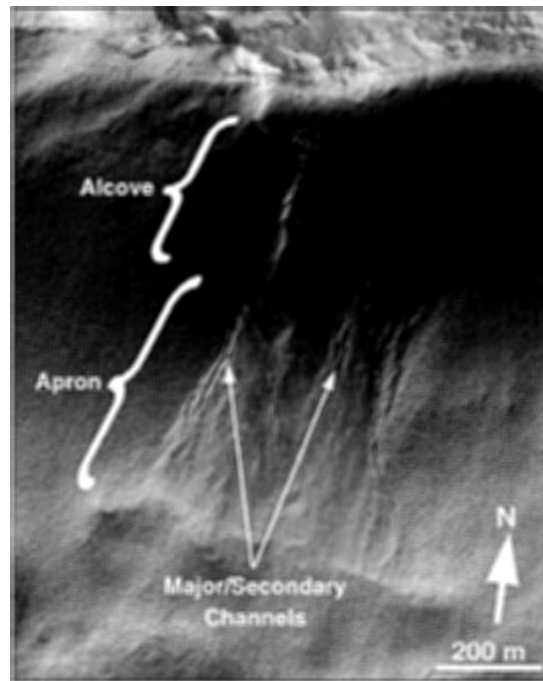


Figure 9: Gullies hypothesised to have formed recently through sapping of subsurface aquifers (after Malin and Edgett, 2000).

Recent investigation of gullies in MOC images suggests that the tapered appearance of the gullies is due to the presence of water-rich snow upslope (Christensen, 2003). Snow transported to mid latitudes during periods of high obliquity is present on cold, pole facing slopes in the mid latitudes. During periods of low obliquity, when temperature at mid latitudes increases sufficiently to cause melting (Costard et al., 2002), gullies are incised downslope from the snow deposits (Christensen, 2003).

3.6: Beaded depression patterns

Closed depressions seen in Viking Orbiter images in the northern plains of Mars have been interpreted as the result of random /unorganised thermokarst processes,

with possible glacial or periglacial origins (Costard and Kargel, 1995). These are distinguished from impact craters through their lack of raised rims and their tendency

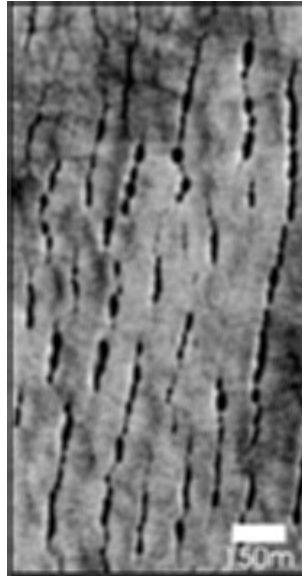


Figure 10: Beaded depressions in western Utopia Planitia. MOC image E02-00880.

toward an elliptical shape. The depressions range in length from 130 to 3000m and have a uniform depth of approximately 30m, estimated using shadows cast under known angles of incident light. In MOC images, depressions under 100m in length were resolved (fig. 10) in Utopia Planitia (Seibert and Kargel, 2001). These depressions are suggested as anomalously forming in areas of polygonal terrain on the northern lowlands. However termination of polygon troughs at the edges of the depressions suggests that the pits form at the same time or possibly after the polygons (Seibert and Kargel, 2001).

Chapter 4: Methods

4.1: Mars Global Surveyor and Mars Odyssey

Mars Global Surveyor (MGS) was launched in 1997 and inserted into orbit around Mars later that year. In 1999 MGS obtained circular orbit with an average elevation of 348km above the Martian surface. Scientific instruments carried onboard MGS include the Mars Orbiter camera (MOC), Thermal Emission Spectrometer and Mars Orbiter Laser Altimeter (MOLA) which measures topographic elevation using infrared light. MOLA provides a standard reference frame for elevation measurements as distance between shots is measured from the spacecraft rather than an arbitrarily chosen surface datum. Since 1999 MOLA has mapped the entire planet with a vertical accuracy of 1m (Smith et al., 2001). Using MOLA data the first high resolution map of Mars topography has been produced (fig. 4) making it possible to characterize the topography of small geographic areas in detail. The lower limits of MOLA resolution are limited by its footprint, presently at 128 pixels/degree.

The Thermal Emission Spectrometer (TES) has multiple applications, including measuring the global grain size distribution of the top 3cm of the Martian surface (Mellon et al., 2000, Christensen et al., 2001). Grain size measurement is accomplished by using TES-derived thermal inertias (the rate of heat loss) of the Martian surface layer (Mellon et al., 2000). Surface materials such as rocks, sand, dust and bedrock contribute to diurnal temperature fluctuations and the thermal inertias derived from them. The surface temperature variations are sensitive only to the upper few centimeters of the surface as are the resultant thermal inertias (Mellon et al, 2000) Thermal inertia (I) is derived from the equation: $I = (k\rho C)^{1/2} [\text{Jm}^{-2}\text{K}^{-1}\text{s}^{-1/2}]$

where K is the bulk thermal conductivity [$\text{Wm}^{-1}\text{K}^{-1}$], P is the bulk density of the material [Kkgm^{-3}] and C is the specific heat capacity [$\text{Jkg}^{-1}\text{K}^{-1}$]. Global maps of grain size distributions are continually improving as TES continues to record thermal inertias (fig. 5).

Mars Odyssey was launched in 2001 and reached Mars later in the year. Odyssey began mapping the planet in early 2002 and is scheduled to finish its mission late in 2005. Odyssey carries with it instruments specific to atmospheric and geological studies of Mars including the Gamma Ray Spectrometer (GRS) which is currently mapping the occurrence of subsurface water (Boynton et al., 2002).

GRS measures the emission of gamma rays, on Mars, produced by the interaction of secondary neutrons with a surface layer 1 to 2 metres thick. Each element has a specific gamma ray line and the subsurface compositions are characterised based on the gamma ray lines measured (Mitrevanov et al., 2002). High energy neutrons that collide with hydrogen atoms lose significant amounts of energy compared to collisions with other atoms and deficits of high energy neutrons suggests that hydrogen is present in the subsurface (Masarik and Reedy, 1996). Large amounts of hydrogen measured in some locations as well as the dependence of hydrogen content on latitude indicate that hydrogen is present in the form of physically and/or chemically bound H_2O within the regolith (Boynton et al., 2002). Further inverse models from measured epithermal neutron flux are consistent with concentration of water in a subsurface layer beneath a water-poor layer of varying thicknesses at the surface (Boynton et al., 2002).

4.2: Selection of regions

Regions under study were selected on Mars and Earth as potentially containing

beaded depressions based on previous observation and conditions suspected to be favorable to their formation. Conditions that would promote the formation of beaded depressions include the presence of a fine-grained substrate, possibility of the presence of water and temperature conditions conducive to permafrost formation at least sporadically during the past (Hopkins et al., 1949). On Earth, regions that fulfill these criteria are limited to high latitudes such as Northern Canada and Alaska. On Mars, regions that are predicted to support stable near-surface ground ice, and fulfill other criteria are limited to regions pole-wards of 40° (Fanale et al., 1986).

The primary region selected for study on Mars is located in Utopia Planitia in the northern plains. In this area grain size measurements, derived from Thermal Emission Spectrometer (TES) data show that at least the top three centimeters of sediment are fine to medium grained, possibly interspersed with infrequent boulders and/or outcrops of bedrock (fig. 5)). Gamma Ray Spectrometer (GRS) readings are interpreted to indicate that the upper metre of regolith in Utopia Planitia presently contains 4% by weight water ice (Boynton et al., 2002). Substantial work has been done in Utopia Planitia on patterned ground, specifically polygons, and suspected water related landforms (Costard and Kargel, 1995; Heisenger and Head, 2000; Seibert and Kargel, 2001) and the presence of water is suggested by all as a probable cause of these features. The relatively high density of MOC images in the area also makes Utopia Planitia an appropriate site for investigation.

4.3: Terrestrial and Martian images

Comparison of beaded depressions that range in diameter from less than 5m to 300m, on the surface of Mars and Earth, comprise the basis for this study. High

resolution images of Utopia Planitia, Mars, and the Northern Alaska coastal plain, were selected based on their representation of beaded depressions.

Mars Global Surveyor (MGS) is currently in orbit around Mars and carries onboard the Mars Orbiter Camera (MOC), which is designed to acquire high resolution images of the Martian surface (narrow angle camera) as well as lower spatial resolution images of the Martian surface and atmosphere (wide angle camera). MOC acquires images through progressive scanning and subsequent compilation of surface data as the craft passes over the targeted site. Using this method image resolutions as high as 1.55m per pixel are obtained and individual pictures may cover areas up to 70.56km² (Albee et al., 2001).

MOC images used in this study were acquired through 2 databases available through public access websites. The Malin Space Science Systems website (www.msss.com) offers a gallery of all archived MOC images as well as publicly targeted MOC images. MOC images are referenced to assigned MOC numbers (related sequentially to the order in which they were taken) and are retrievable through an interactive map that allows images to be selected by geographic region. MOC images also are available through the Planetary Data System (PDS) atlas (<http://pds-imaging.jpl.nasa.gov/Atlas/>), NASA's database for all publicly available mission data. The PDS atlas contains all archived MOC images and accompanying metadata. Images can be retrieved using MOC number, geographic coordinates or through an interactive map.

24 MOC images were selected from a distinct region of beaded depressions in Utopia Planitia (Appendix B). This region is defined by a rectangle whose corner coordinates are: 280°W 40°N (northwest corner), 280°W 55°N (northeast corner), 260°W

40°N (southwest corner) and 260°W 55°N (southeast corner). Images are distributed unevenly throughout the area (fig. 11) with minimal coverage in the northwest and southeast corners. 41 additional images cover a larger area in Utopia Planitia, however not at the resolution required for this study.

The majority of the selected images contained in excess of 500 depressions. In 6 images, with relatively homogenous topography at the scale of observation, depressions covered the entire area (i.e. Fig. B.1). In the remaining 18 images beads were contained in confined regions of similar topography (i.e. fig. B.21) or grouped in other patterns (i.e. Fig. B.9).

Aerial photographs of the Alaskan coastal plain are at a scale of 1:60000 and when converted into digital format have a resolution of 1.341m per pixel. All aerial photos used are in colour infrared and were acquired through the Geodata centre at the University of Alaska (<http://www.gi.alaska.edu/services/geodata/>).

The northern Alaska coastal plain is a lowland region in the northwest corner of Alaska. 9 aerial photos were selected for study and cover an approximate area of 2000km². Vegetation is mesic tundra and dwarf shrubs. Soils in the area are fine-grained, predominantly aeolian silt, overlain by ice rich organic soils that reach depths of 1m in low areas and <30cm in relatively well drained interfluves (L. Plug, personal communication, March 15, 2004). Permafrost in the area is continuous and mean annual air temperature is ~-8°C (<http://www.wrcc.dri.edu/>, 2004).

4.4: Extracting data from Martian and Terrestrial images

All studied patterns are present in separate image files, produced by digitising individual forms on separate layers in a computer graphics package. The outer rims of

depressions were traced along the greatest colour contrast, interpreted as edges of depressions (fig.11). Chains of depressions, in which connective troughs could be resolved, were traced from the top of the first depression in the chain to the bottom of the last depression in the chain following the troughs (fig. 11). The end/beginning of a single chain is defined as the first/last depression that is connected to the previous depression by a visible trough (fig. 11). Both the digitised depressions and connective troughs were exported as raster files. Accuracy and subjectivity of this method was tested by re-digitising specific images and comparing derived values.

For all terrestrial and Mars patterns, the following characteristics were measured: 1) area and perimeter of each depression; 2) length of the major and minor axes of each depression, used to calculate an eccentricity, a ratio of ellipticity; 3) orientation of the major axis of each depression with respect to north; 4) distances from the weighted center of each depression to all other depressions measured in metres; 5) the angle between the weighted centre of the nearest neighbouring depressions, also measured with respect to north; 6) length of complete chains; 7) sinuosity of those chains. For all measurements, scaled image pixel width and the aspect ratio are converted to metres, so all measurements are produced in SI units.

The area of individual depressions is measured in square metres by calculating the number of pixels enclosed by the digitized perimeter. Major and minor axes are selected by fitting an ellipse over each feature. Eccentricity (e) is defined in terms of semi-major a and semi-minor axes b by $e = (1 - b^2/a^2)^{1/2}$. The range of e is $0 < e < 1$. $e = 0$ denotes no elongation (a circle) and $e = 1$ is maximum elongation (a line). The angle between nearest neighbouring depressions is measured as the deviation angle of the connective trough from a line that defines the shortest distance between their centers (fig. 11). The shortest

distance between the centers of 2 neighbouring depressions is also used to define the separation distance between nearest neighbouring depressions. The length or reach of single chains is measured in metres as the distance, from the perimeter of the first depression to the perimeter of the last depression in the chain. In measuring sinuosity of chains, the scheme of Friend and Sinha (1993), developed to describe planform of river channels, is used. Sinuosity ratio is defined as follows: $S = Lc_{max}/LR$ where Lc_{max} is the mid-channel length for the same reach and LR is the overall length of the channel reach.

Automatic selection of depressions and connective troughs was attempted by selecting all pixels within a specified colour range. Selected pixels were cropped from the image and exported as image files. This method was not used on every image as the colour tolerance range allowed pixels to be selected that are not part of the beaded depression patterns. Selection of pixels not associated with the beaded depressions made this method unsuitable for pattern recognition.

Measurements described above are collected for each depression and each trough within a patterned region. For Mars patterns, regions included between approximately 100 to 4600 individual depressions, with number depending on size of the region and on the density of depressions (beads/m²). For each region summary statistics of pattern characteristics are derived from measures of all individual depressions and chains. For example, depressions can be characterised by a mean area of depressions and standard deviation for that region. Histograms showing depression area, eccentricity and length of chains also are generated and compared between regions. The automated extraction of measurements from patterns, and their binning into distributions, was done using scripts that use Matlab and the image processing toolbox (www.Mathworks.com, 2003).

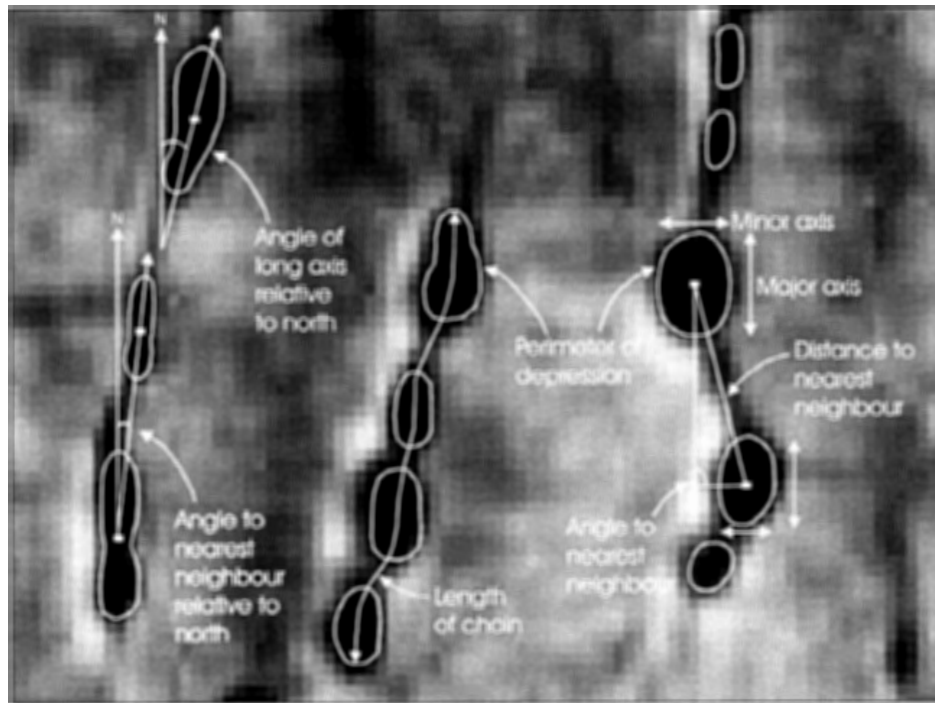


Figure 11: Measurements of beaded depression patterns.

4.5 Models

To test hypotheses for mechanisms that form beaded depression patterns on Mars, Martian patterns are compared with terrestrial patterns and with synthetic patterns. For terrestrial patterns, digitised aerial photos of the Northern Alaskan Coastal Plain were used (Figure A.1 to A.4). Beaded drainages digitised from this area are assumed to be representative of organized chains whose morphology forms by flowing water between thaw derived depressions with spacing dependent on shape and spacing of the polygonal network that preceded beaded drainage development. These were processed and analysed in the same way as the Martian images and data was extracted from the digitised images using the same approach.

Synthetic models were generated by distributing depressions into featureless and polygonal regions using known, simple rules. Models were prepared for every image using the area of the image and the number of beads in the image to generate various patterns of distribution. Two categories of synthetic patterns were used;

- 1) Depressions are placed at random locations, representing the hypothesis that depressions initiate at random and there is no deterministic relationship between individual depressions.
- 2) Polygons are placed into a polygonal network with location of each depression randomly selected from sites along polygonal troughs, representing the hypothesis that depressions are thaw and/or sublimation features that initiate along troughs but that there is no deterministic relationship between individual depressions.

All of the models are individually used to compare to each Mars network; in each comparison beaded depressions drawn from the original image are used. The aerial coverage and number of depressions placed is uniform between all models and identical to the Mars patterns; only the arrangement of depressions varies.

CHAPTER 5: RESULTS AND DISCUSSION

5.1: Qualitative Description

The MOC images present in the sub-region of Utopia Planitia, selected for study, are distributed unevenly. Therefore the sub-region and distribution of MOC images has been divided into 5 geographically distinct regions (Figure 12). Region 3 lies in the mottled member of the Vastitas Borealis Formation, which is characterized by crater-ejecta blankets that have higher albedo than adjacent terrain, giving a mottled appearance. In places, gently rolling, closely spaced hills averaging 5 km in diameter can be distinguished. Possible origins of this layer include lava flows erupted from fissures, alluvial or aeolian deposition (Scott and Tanaka, 1987). Region 5 lies in the grooved member of the Vastitas Borealis Formation which is characterized by curvilinear and polygonal patterns of grooves and troughs. Possible origins of the patterns that typify the region include compaction, tectonism, or periglacial processes (Scott and Tanaka, 1986). Regions 1, 2 and 4 lie in the Knobby member of the Vastitas Borealis Formation which is similar in appearance to mottled member but generally has higher albedo and abundant small, dark, knoblike hills. Possible explanations for the small hills that characterize the region include small volcanoes, remnants of highland terrain, crater rims or pingos (Scott and Tanaka, 1986). Regions 1, 2 and 4 are separated by 300km (region 1 and 2) and 850km (region 1 and 4). Division of the region into separate regions also reflects the variation in average/local slope resolved in MOLA topography (Figure 13).

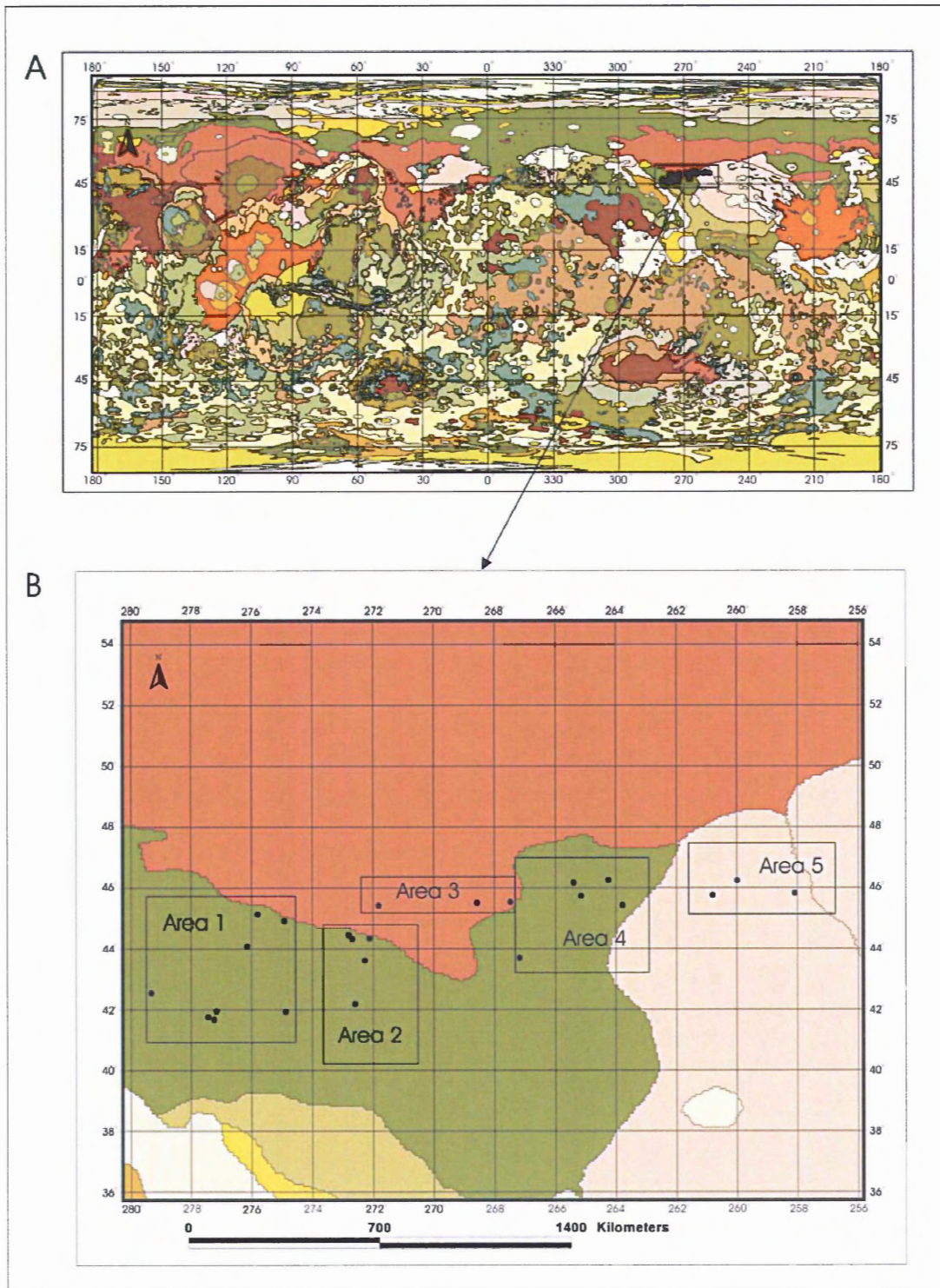


Figure 12: A- Global stratigraphic map of Mars, showing location of Utopia Planitia beaded depression patterns (after Scott and Tanaka, 1986; Greeley and Guest, 1987). B- Divisions of MOC images based on geology and topography and morphology of depressions in Utopia Planitia. Legend and explanation are located in appendix C.

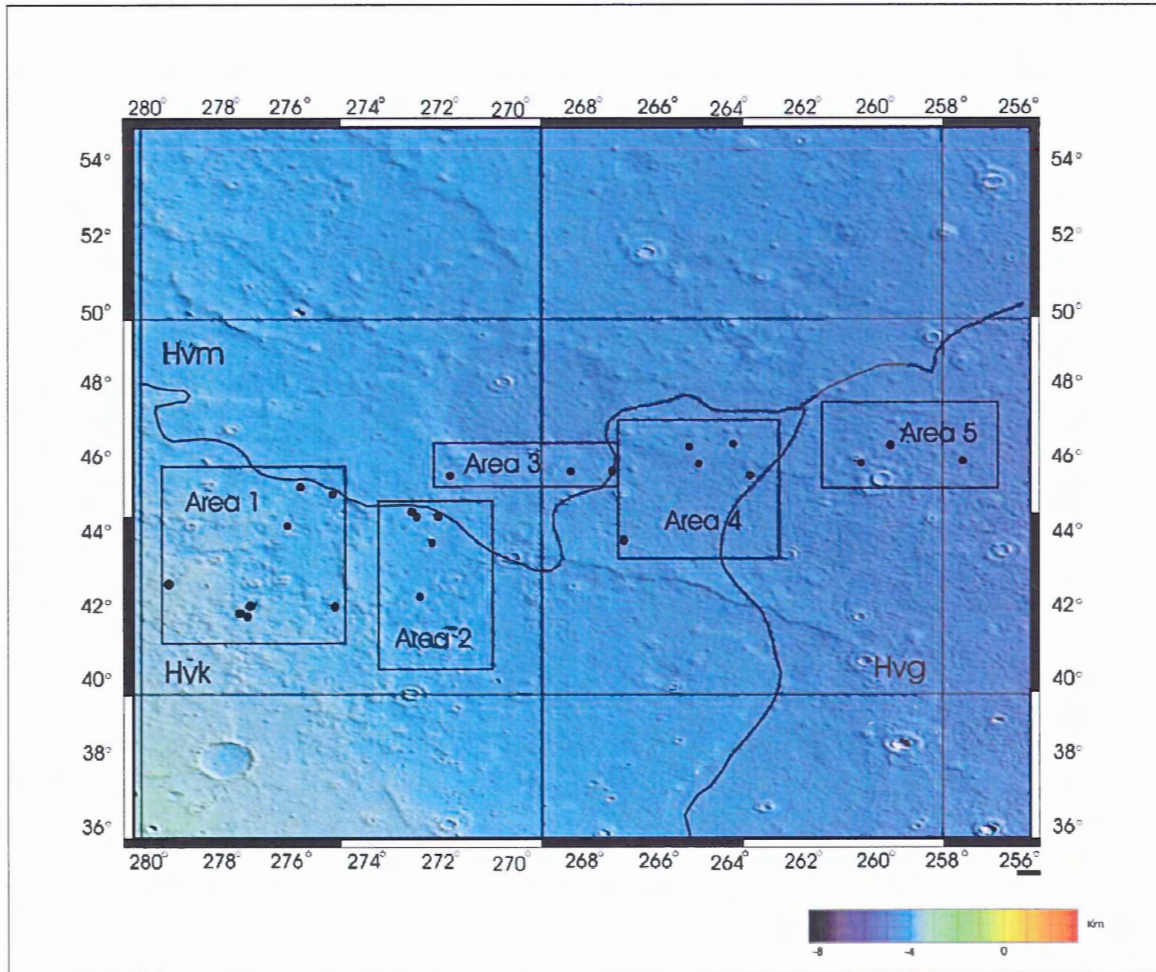


Figure 13: Top – MOLA derived shaded topographic map (after Smith et al., 2001) with overlay of regional divisions assigned on stratigraphic map (after Scott and Tanaka, 1986; Greeley and Guest, 1987). Legend and explanation are located in Appendix C.

REGION 1

At the scale of observation, depressions in region 1, occur exclusively on relatively smooth, homogenous surfaces (Figure 15). Individual depressions do not exceed 50 meters in diameter with the lower limit of diameter at the threshold of resolution (approximately 6m in these images). In the majority of chains, depression diameter has a bimodal distribution with smaller diameter depressions dominating chains.

Depressions are moderately elongate, with major axes parallel to the reach of the chain. Chains of depressions are linked by visible troughs which rarely exceed 100m in length. What appear to be coalesced depressions form wide troughs that parallel the curvature of chains. The total length of individual chains exceeds 1000m in some cases, however the average length of chains is less than 400m. Chains have low curvature, however some irregular circular patterns occur in all images within the region (Figure 14), in which depressions deviate from straight orientations that dominate in the region. Polygonal networks are present in most regions that contain depressions, except near those chains composed of coalesced depressions. In all cases where both polygonal networks and beaded depressions are present, depressions occur at the termini of polygonal network troughs.

Elevation in region 1 ranges from -3 to -5 km below datum (Figure 13) and slope shows small scale variations in degree and direction. Regional slope trends 0.2km per degree towards 043°. Images that contain beaded depression patterns appear to be present in local topographic lows within the regional gradient (Table 2).



Figure 14: Deviant patterns that occur exclusively on smooth terrain in all regions.

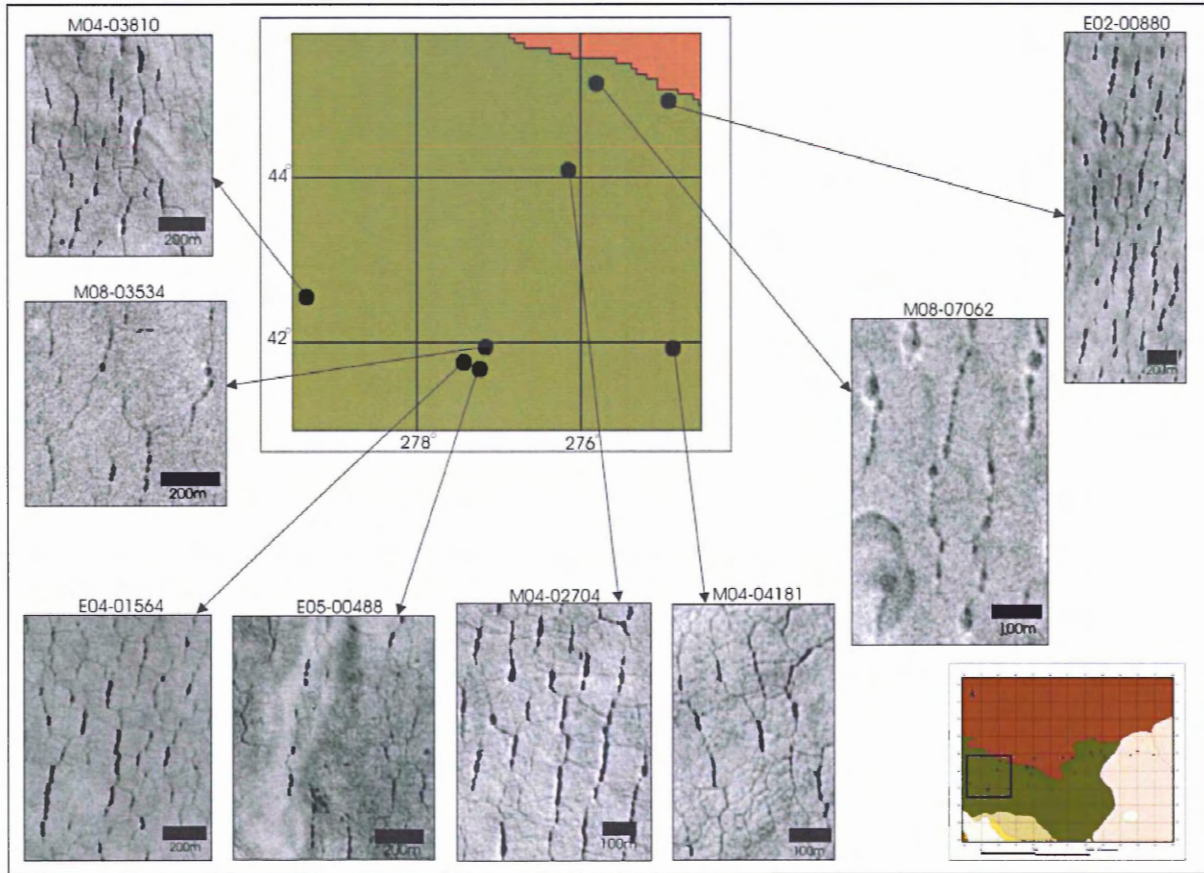


Figure 15: Locations of MOC images present in region 1. Small map in right hand corner shows location in regional map (Figure 12).

REGION 2

In region 2, topography is variable, but generally smooth (Figure 17). Depressions are dispersed throughout the images and are less concentrated in chains than in region 1. Diameters range from the limit of resolution (approximately 3m) to 30m. Elliptical depressions, in which the major axes parallels the reach of the chain, are prevalent and circular patterns that are common in region 1 are not present. Within single chains there is a rough bimodal distribution of depression diameter, however large depressions occur relatively infrequently when compared to region 1. Troughs are visible in all chains and

trough length is significantly less than 50m. Chains display no large curvature and total length of chains is also considerably shorter than in region 1, with chains longer than 300m rare. Polygonal networks are visible in all images, however there are regions where polygons are present without beaded depressions. Irregular circular patterns superimposed on chains are absent in some images and occur less frequently than in region 1.

Elevation in region 2 ranges from -4 to -4.7 km below datum however this elevation change spans only $\sim 3^\circ$ making the slope approximately 0.23km per degree. Approximate direction of slope is 051° (Table 2).

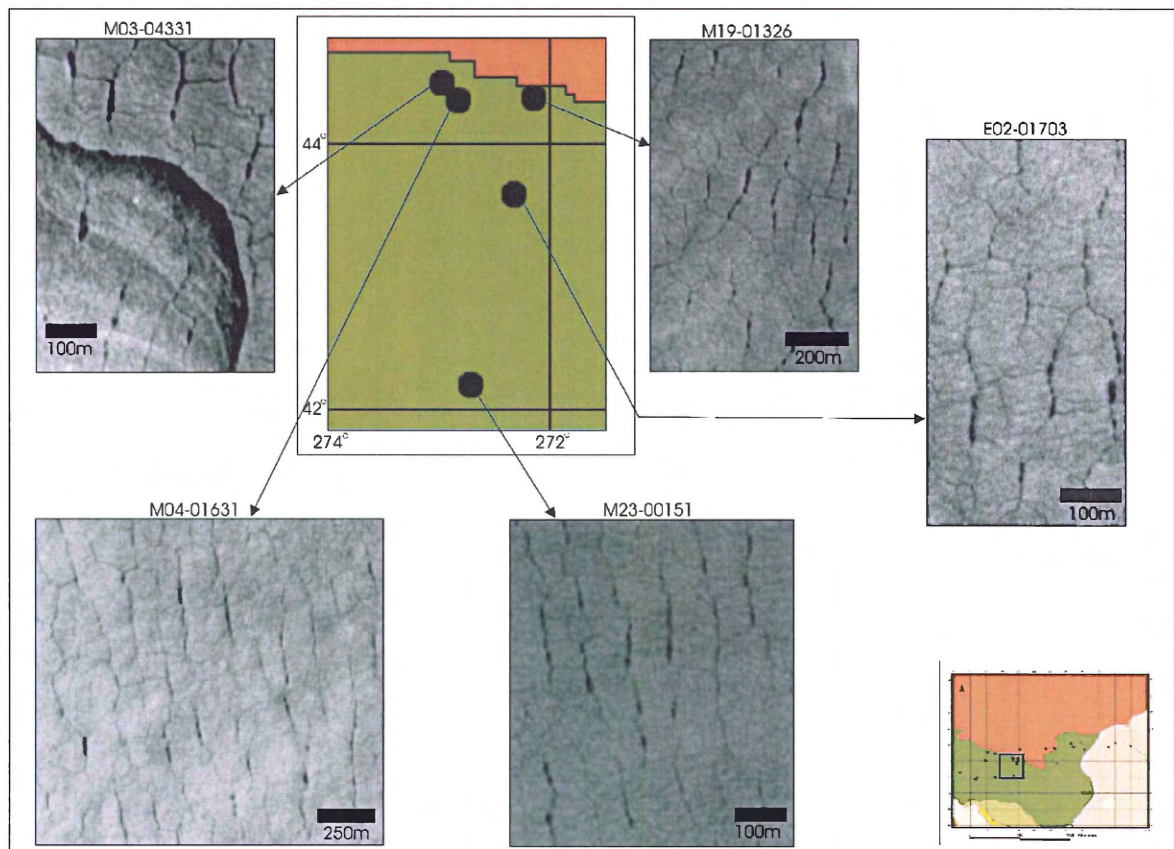


Figure 16: Locations of MOC images present in region 2. Small map in right hand corner shows location in regional map (Figure 12).

REGION 3

Two types of surface are present in region 3 images; a cratered, rough terrain and a smooth terrain that is characterised by scarp-like features (Figure 17). Depressions and polygonal patterns occur predominantly in the smooth terrain. Diameter of individual depressions range from the limit of resolution (1.55m/pixel) to 30m and tend toward extreme ellipticity. Diameter of depressions is uniform within individual chains. Chains composed of coalesced depressions are common. Few troughs are visible and those that are rarely exceed 30m. Single chains are much shorter than those present in regions 1 and 2 and generally do not hold more than 6 depressions. Rare circular patterns are present in one image and are located on the smooth terrain.

Elevation in region 3 ranges from -4 to -4.2 km below datum at an average approximate slope of less than 0.5km per degree. The direction of slope is 051° , very similar to region 2 and 4 which bound either region to the southeast and west side respectively (Table 2).

REGION 4

Variable topography is associated with region 4. Depressions occur exclusively on the smooth terrain (Figure 18). Of the 5 images present in this region, 3 contain unique patterns of parallel chains of depressions of constant diameter. Length of the parallel chains exceeds 1000m in all cases and diameter of individual depressions remains constant, near 20m. Depressions do vary widely between circular to highly elliptical forms between individual chains. Troughs are frequently visible connecting the depressions and trough length varies over only a small range, 20 to 35m. Between all sets

of parallel chains there is a visibly different surface that appears smoother than the surface outside of the set. Polygonal networks are visible in only one of the three images of long chains, however images without long chains contain abundant polygons with interspersed depressions and short chains reminiscent of region 1.

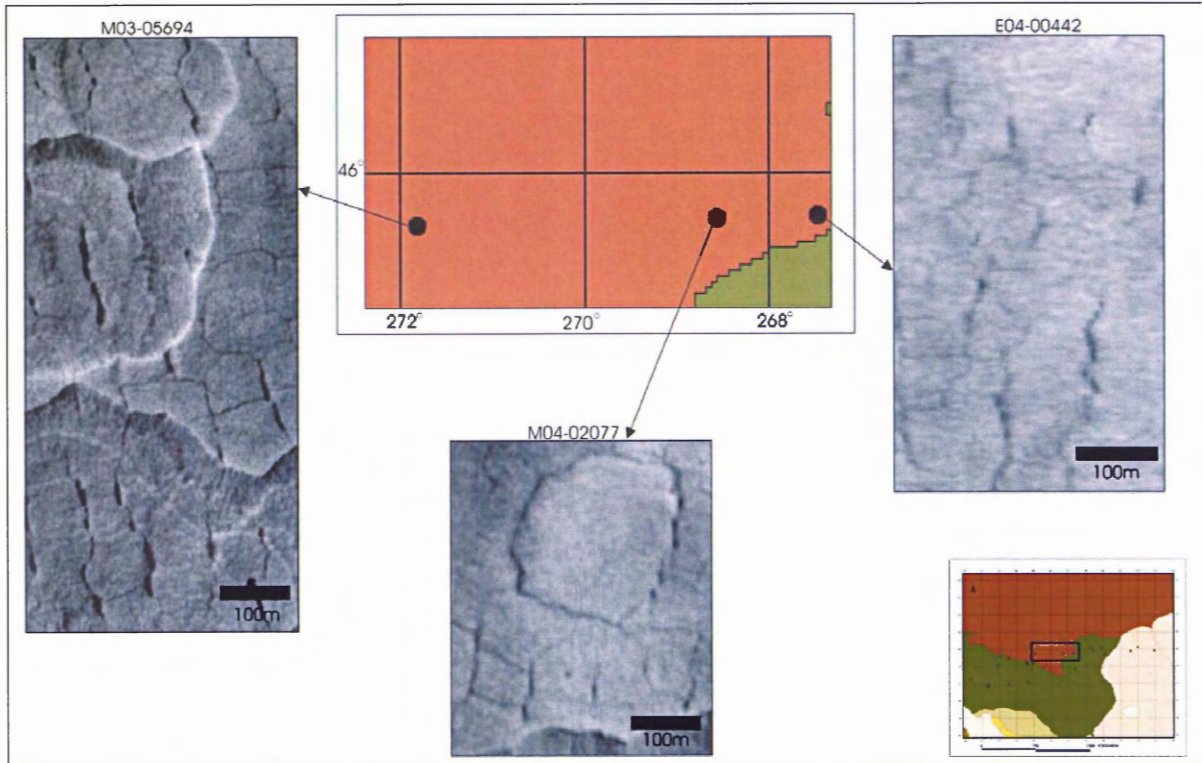


Figure 17: Locations of MOC images present in region 3. Small map in right hand corner shows location in regional map (Figure 12).

Elevation of region 4 differs little from region 3 and 5 which bound region 3 on its east and west sides. A shallow slope of approximately 0.2km per degree faces 051° toward the northeast (Table 2).

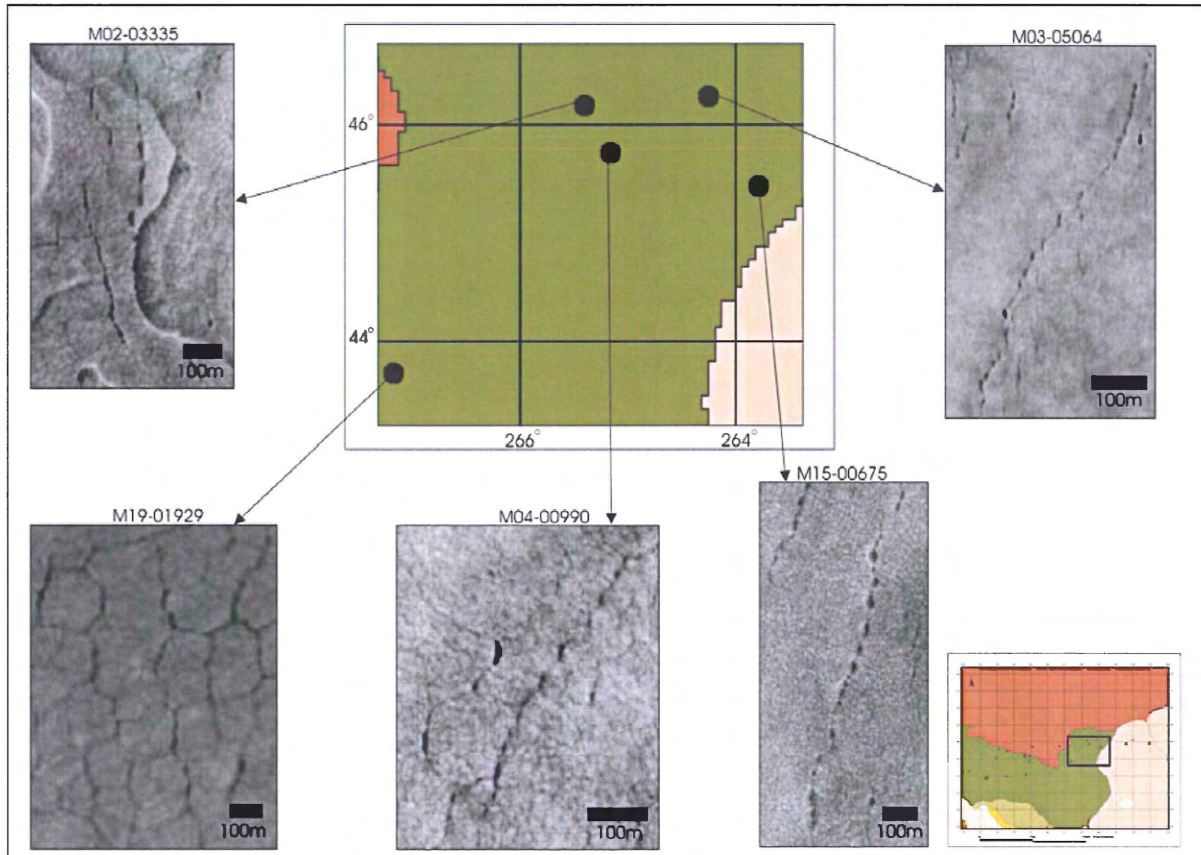


Figure 18: Locations of MOC images present in region 4. Small map in right hand corner shows location in regional map (Figure 12).

REGION 5

Terrain in region 5 ranges from regions of smooth surfaces with little topographic variation to regions that contain scarp-like features with seemingly rough surfaces (Figure 19). Chained depressions occur predominantly on smooth surfaces, though scattered depressions are present on all surfaces. Chains in this region fall into two categories. The first have lengths of 400 to 600m and are composed of circular depressions with constant diameter, as in region 4, however the length is significantly shorter; The second have lengths of 200m and are composed of depressions of varying diameter, as in region 1. A separate pattern from those occurring in other regions is one

that consists of elongate depressions that form discontinuous and irregular chains.

Polygons are not present in any of the images and coalesced depressions are present but are not as widespread as in other regions.

Elevation of region 5 differs little from region 3 and 4. A shallow slope of approximately 0.2km per degree faces 051° toward the northeast (Table 2).

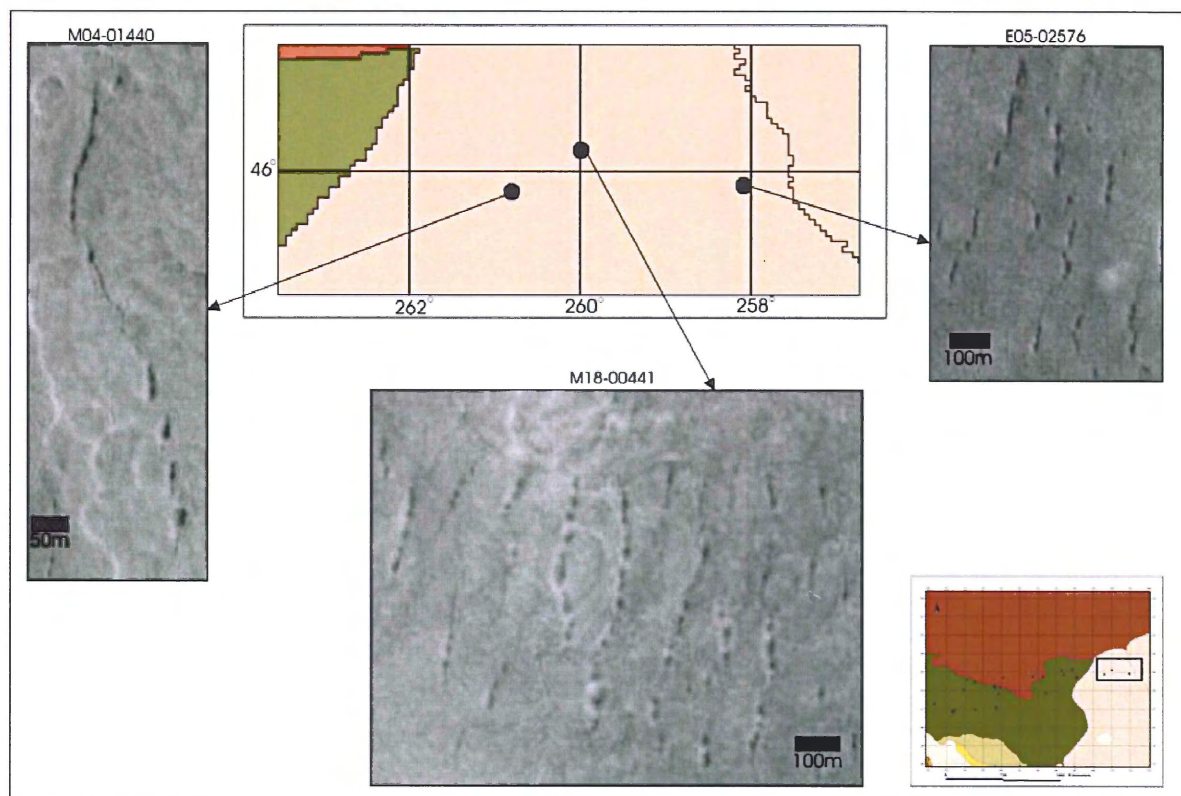


Figure 19: Locations of MOC images present in region 5. Small map in right hand corner shows location in regional map (Figure 12).

| Region | Unit | Elevation range (km) | Width of region (degrees) | Slope (km/°) | Slope Aspect (degrees) | Type of pattern (1-4) |
|--------|---|----------------------|---------------------------|--------------|------------------------|-----------------------|
| 1 | Knobby member (Hvk) of the Vastitas Borealis Formation | -3 to -5 | 5° | 0.4 | 43° | 2 & 4 |
| 2 | Knobby member (Hvk) of the Vastitas Borealis Formation | -4 to -4.7 | 3° | 0.23 | 51° | 3 & 4 |
| 3 | Mottled member (Hvm) of the Vastitas Borealis Formation | -4 to -4.2 | <0.5° | ~0.2 | 51° | 3 & 4 |
| 4 | Knobby member (Hvk) of the Vastitas Borealis Formation | -4 to -4.2 | <0.5° | ~0.2 | 51° | 1, 2 & 4 |
| 5 | Grooved member (Hvg) of the Vastitas Borealis Formation | -4 to -4.2 | <0.5° | ~0.2 | 51° | 1, 3 & 4 |

Table 2: Summary of slope data and morphology of beads (Table 3).

Morphology of beads within Utopia Planitia is variable. Components of the general morphology include the size or region of the depressions, spacing between individual depressions, which are connected by troughs that are wider than the nearby polygon troughs, the angle between adjacent depressions which defines the curvature of the chains and the length of single chains. Four distinct types of beaded depression patterns emerge from qualitative analysis. These include 1) Extremely long chains which are composed of equally spaced circular to sub-circular depressions of consistent region not typically associated with the presence of polygons. 2) Chains of low curvature and moderate length comprised of unequally spaced circular to elliptical depressions of bimodal size distribution that are always associated with the presence of polygons. 3) Chains of medium length that are composed of tightly spaced elliptical depressions of bimodal size distribution, frequently associated with polygonal patterns. Individual types of beaded depression patterns occur within distinct regions sometimes represented by more than 1 image. A fourth type of pattern consists of coalesced depressions of varying

length and width that form widened troughs. Coalesced depressions occur in conjunction with all three types of beaded depression patterns.





| Type | Description | Example | MOC image # | Occurrence |
|------|--|---|-------------|-------------------------|
| 1 | Extremely long chains which are composed of equally spaced circular to sub-circular depressions of consistent area not typically associated with the presence of polygons. |  | M15-00675 | region 4 |
| 2 | Chains with low curvature and moderate length comprised of unequally spaced circular to elliptical depressions of bimodal size distribution that are typically associated with the presence of polygons. |  | M08-07602 | region 1 |
| 3 | Chains of medium length that are primarily composed of tightly spaced elliptical depressions of bimodal size distribution, frequently associated with polygonal patterns. |  | E02-01703 | region 2 and 3 |
| 4 | Consists of coalesced depressions of varying length and width that form widened troughs |  | M03-05694 | region 1, 2, 3, 4 and 5 |

Table 3: Summary of beaded depression pattern types and their occurrence.

Measurement of surficial grainsize inferred from TES (Figure 4) reports a

homogenous distribution of fine grained material with interspersed boulders and/or outcrops throughout Utopia Planitia (Putzig, 2003). However variation too subtle to be accurately measured may account for the variation of morphology. Finer grained regolith that is more susceptible to compaction may support the formation of more coherent chains, such as type 1, whereas a larger quantity of pebble to gravel sized material would create more variation within the chains, such as type 2 and 3. Small scale topographic variability, not reflected in MOLA measurements may also be responsible for subtle differences in the shape of the beads and the coherency of the chains.

The morphology of the individual depressions, which varies from circular to elliptical, may be indicative of a high concentration of ice present beneath the depression, perhaps at the intersection of ice wedges. The termination of multiple polygon troughs in depressions also suggests that these depressions overlie at least the junctions of polygonal networks.

5.2: Quantitative Analyses

Comparison of the eccentricity and area of individual depressions shows no correlation (Figure 20A). The number of beads per m^2 in most cases decreases with increasing mean area of individual depressions (Figure 20B). Comparison of the area of individual depressions in each image with sinuosity of the chains suggests that sinuosity is relatively similar in all cases, deviating little as depressions become larger or as chains become longer (Figure 20C and 20D). The comparison between the length of the chains and depression density also shows a strong correlation, as chain length increases the number of depressions per m^2 also increases (Figure 20E). Distribution and orientation

plots of all Mars patterns are located in Appendix D.

Terrestrial models produced distributions of depression area and chain length similar to Martian patterns (Mars patterns: Appendix D, terrestrial patterns: Appendix E). Area of individual depressions is concentrated in the smaller size bins and tapers off toward a maximum area (Figure 20A). Depressions in Martian patterns tends to be larger than terrestrial depressions, occasionally by 2 to 3 orders of magnitude. Length of the chains in the terrestrial models also shows a similar distribution, with large concentrations of relatively short chains which tapers to a low concentration of very long chains. Chain length appears to be similar; however maximum terrestrial chain length far exceeds the maximum chain length on Mars.

Type 1 models (random distribution of the same quantity of depressions over an equal area) showed completely random distributions (Figure F.1.a to F.7.a) of every parameter measured. This was also the case for type 2 models (random distribution of an equal number of depressions along troughs of a polygonal network). Distributions produced by type 2 models show no preferential “clustering” along troughs and no trends are evident that would suggest any type of ordered pattern formation.

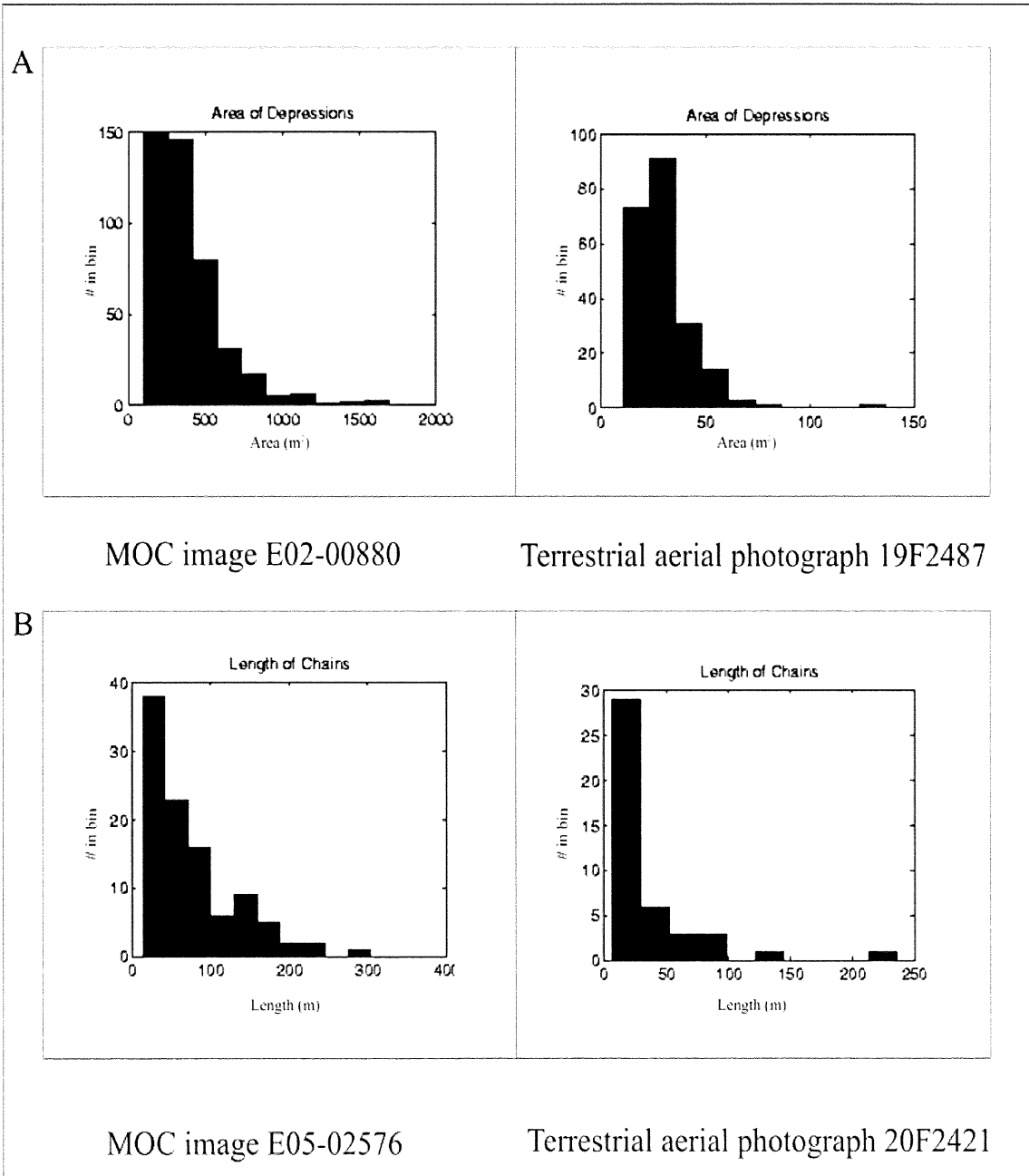


Figure 20: A: Comparison of distribution of depression area in Mars patterns and terrestrial patterns. B: Comparison of distribution of chain length in Mars patterns and terrestrial patterns.

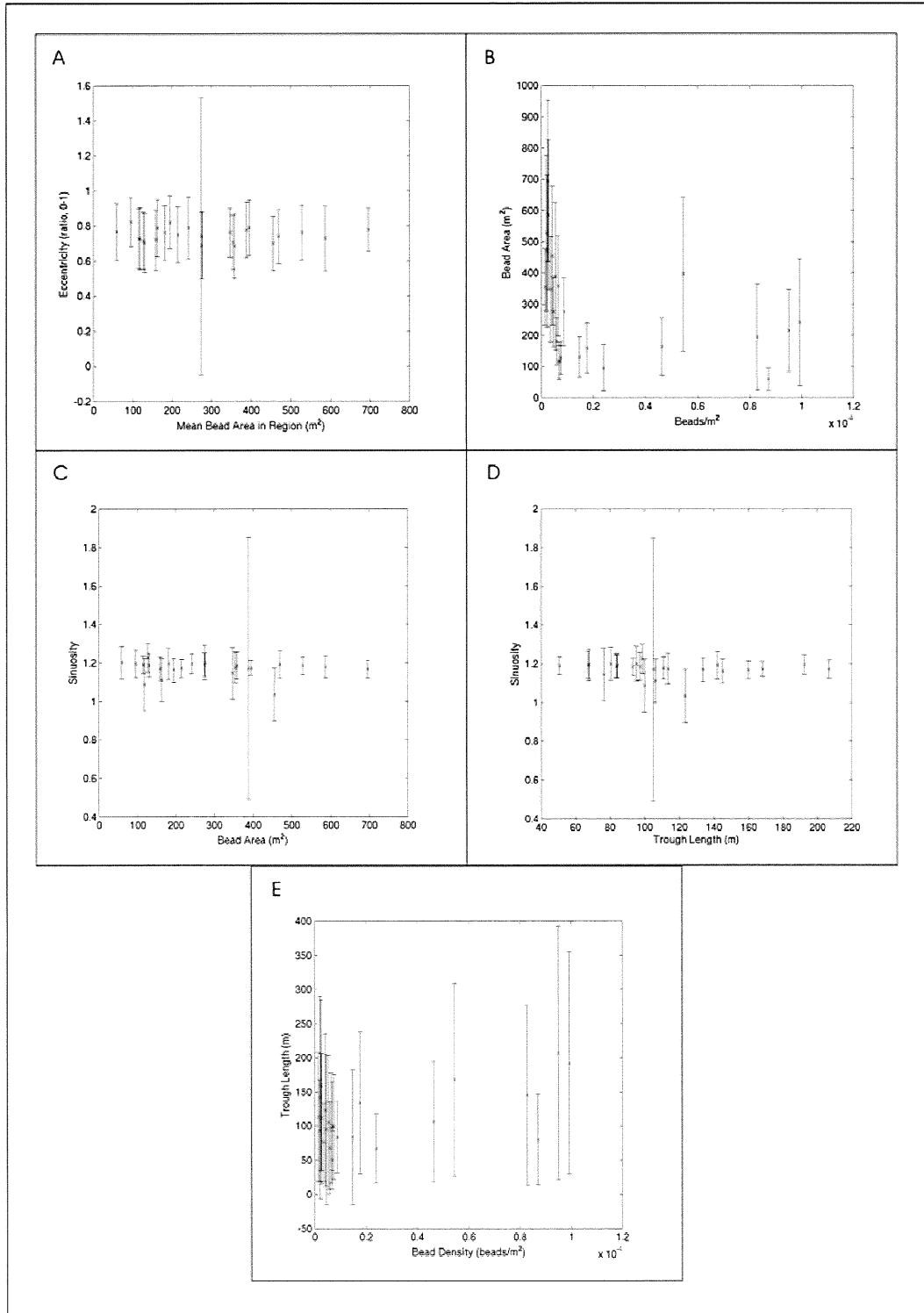


Figure 21: Graphs of depression and chain measurements. A) Eccentricity (ellipticity of depressions) vs. mean area of individual depressions (m^2). B) Area of individual depressions (m^2) vs. depression density (depressions per m^2). C) Sinuosity vs. area of individual depressions (m^2). D) Sinuosity vs. mean chain length (m). E) Chain length (m) vs. depression density (depressions per m^2)

5.3: Hypothesised Mechanisms of Formation

Comparison of Martian beaded depression patterns with terrestrial and synthetic models show that Mars depression patterns most closely resemble terrestrial patterns, rather than the synthetic models which simulate random depression formation (Figure 20 A and B; Appendix E; Appendix F). Terrestrial patterns form organized chains of depressions clustered along troughs rather than random distributions of depressions. These findings suggest Martian patterns may form in the same manner as those on Earth which are created by thawing and subsidence above intersections of two or more ice wedges.

Beaded depression patterns in Utopia Planitia are strongly segregated into 4 types of patterns (Table 3), each representing a different stage in pattern evolution. The evolution of chains of depressions proceeds from early equally spaced, circular depressions (type 1), through stages of increasing coalescence of depressions (type 2 and 3), to the final stage of active pipe flow represented by widened troughs, which have altered morphologies from the original patterns of multiple depressions within 1 chain (type 4). Here, this conceptual model is described and implications for Mars climate and substrate highlighted.

In my conceptual model, initiation of beaded depressions occurs during obliquity highs, characterized by strong seasonality. Warmer summer climate induces thawing of a subsurface reservoir of ice within the regolith. Thawing is concentrated on pole-facing slopes, which receive the most solar energy at high obliquity (Costard et al., 2002; Head et al., 2003). Although atmospheric pressure may have been much higher in the distant past (Noachian to early Hesperian), allowing the persistence of liquid water at the surface

during these times, no mechanisms have been proposed for increased surface pressure on Mars in the recent past (last million years). Therefore, any liquid water exposed to the atmosphere at the surface or near-surface, during recent obliquity highs, would have been lost via sublimation.

Sublimation of water vapour in the top few centimeters to metres of Mars' surface desiccates the upper layer of the Martian regolith and concentrates salts present in sublimating water in soil pore space. This process creates a crust of indurated sediment with low permeability to water vapour, thus slowing or halting loss of water to the atmosphere. Protective cover provided by impermeable sediments and continued thawing of ice rich regolith and ice wedges creates conditions conducive to the persistence and gravity driven flow of near surface water (Zent, 2003). Water occurs in a confined layer between the underlying ice-rich regolith and the desiccated regolith above (Figure 21).

High concentrations of relatively pure ice in ice wedges, suspected to be present in mid latitudes (Zent, 2003), would produce larger amounts of water upon thawing than adjacent regolith containing only pore ice. Larger volumes of water present above ice wedges would, in turn, accelerate melting due to higher heat retention of water. The area of enhanced melting, confined above ice wedges, creates a preferred or primary course for gravity driven flow (pipe flow).

Selection of primary channels by enhanced melting would depend on slope, with primary channels being those that run down dip rather than along strike as has been observed in troughs of terrestrial ice wedge networks (Mackay, 1995).

Heat is conducted and advected to the walls of the still-frozen regolith and floor of the space surrounding the intersection, causing the melting front to propagate radially,

as proposed

by Hopkins (1949) for terrestrial thaw patterns. Because of the concentration of ice in ice wedge intersections, evacuation of water following thawing causes localized subsidence of ground over the intersection. Shallow basins appear over underlying wedge intersections.

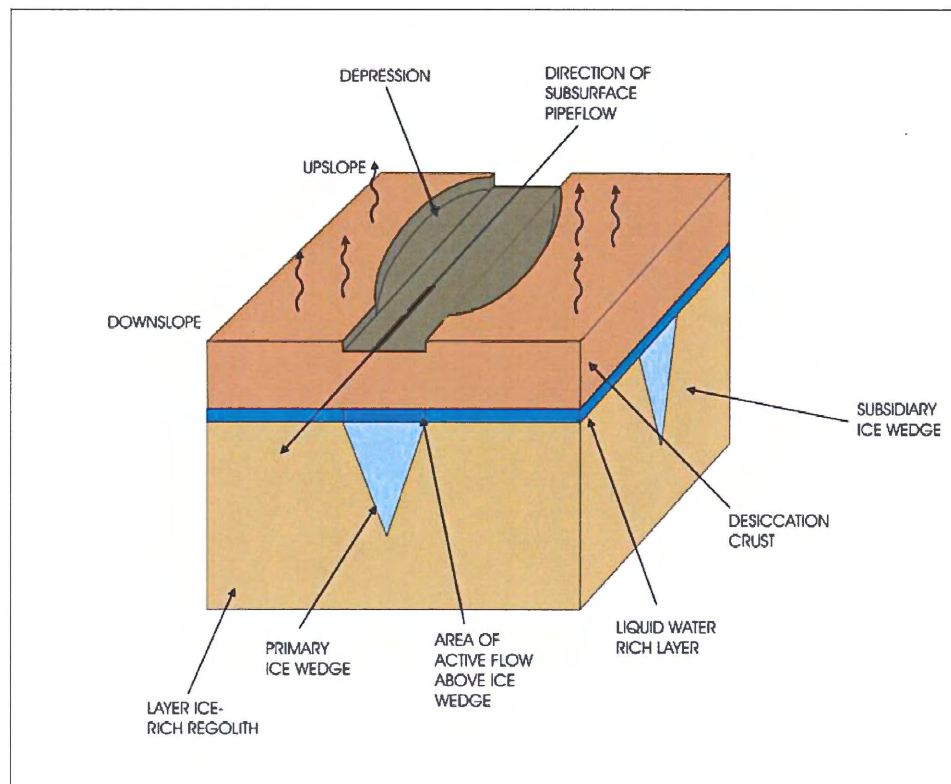


Figure 22: Schematic representation of depression growth in Martian beaded depression patterns. After thawing has been initiated propagation of the melting front parallel to the subsurface flow direction creates elliptical subsidence rather than radial subsidence associated with other ground ice structures.

Thawing due to the preferred path of the water above the primary ice wedge causes the melting front to propagate faster in the direction parallel to the primary reach, along which subsurface flow (pipe flow) is occurring (Figure 22). Other areas surrounding the intersection are poor in ice relative to the junctions of the ice wedges. Relatively ice-poor areas include secondary intersecting ice wedges and regolith that

surrounds the intersection, which contains only pore ice. Ice-poor areas melt more slowly and generate less subsidence than intersections and primary ice wedge. Progression of the melting front radially from the intersections of ice wedges and preferentially parallel to the reach of the preferred flow path causes the elongation of the initially circular depression. Through time, as melting occurs preferentially in the direction of flow, the depression acquires a progressively more elliptical shape.

Propagation of the chain and initiation of new depressions occurs downslope with additional depressions forming wherever secondary ice wedges intersect the primary wedge.

As water flows downslope above the primary wedge pooling occurs above intersections where enhanced melting occurs, initiating a new depression. This hypothesis is supported by the correlation between increasing chain length and increasing number of depressions, which suggests that chain growth is dependent on depression formation.

When neighbouring depressions along the same chain grow sufficiently large they coalesce to form larger, more elliptical depressions typical of type 2 and 3 (Table 3). Area of the depression at the time of coalescence depends on the initial separation of ice wedge intersections and resulting depressions. Eccentricity (ellipticity of individual depressions) shows no specific dependence on bead size (Figure 21A) however it is difficult to normalize if original depression size is not known. Also, as multiple depressions coalesce the number of associated depressions decrease; therefore depressions that have merged have less effect on the mean area of depressions.

When the majority of depressions in a chain have merged, morphology of the chain is significantly altered (type 4). Individual depressions are not evident and

polygonal troughs are typically absent (Table 3). Though morphology of widened troughs is altered from the original identifiable state of beaded depressions, their occurrence in conjunction with all other beaded depression pattern types suggests that the widened troughs are a direct consequence of coalescing depressions. The relationship between chain length and depression density (Figure 21E) also suggests that enlargement of depressions is a direct consequence of the reduction in the number of depressions present and therefore the growth of depressions is accompanied by coalescence of neighbouring depressions.

It has been suggested that the morphology of Martian polygonal networks in Western Utopia Planitia, compared to terrestrial networks is more highly ordered and displays preferred orientations in large areas (Allen, 2004). Beaded depression patterns resulting from thawing and subsidence above regularly spaced ice wedge intersections would exhibit consistent sinuosity. Pattern organisation and consistency combined with strong dependence of primary flow direction on slope, suggests sinuosity of individual chains should be similar in all beaded depression patterns. Evolution of a chain of depressions, from circular to more elliptical depressions and finally to widened troughs, would not affect the sinuosity of the chain because propagation of the melting front occurs preferentially parallel to a single ice wedge. Results are consistent with this hypothesis as sinuosity of all Mars patterns shows small variation around a mean sinuosity of 1.5 to 2 (Figure 20C), independent of the number of beads or chain development.

Variation in the types of patterns associated with geographic region suggests that the timing of initiation of depressions has varied due to local orientation of slopes with

respect to Mars' rotational poles, where more intense heat was present during periods of higher obliquity (Costard et al., 2002). Different amounts of thawing may also affect the propagation of the chain as higher heat input would cause faster development of depressions and chain, which would result in a more uniform distribution of bead area like that in type 1. Those chains on slopes receiving less heat input would experience slower growth and morphology of individual depressions would be more dependent on the propagation of the melting front parallel to the reach of the chain. This scenario would create morphologies consistent with type 2 and 3.

CHAPTER 6: CONCLUSIONS AND FUTURE WORK

6.1: Conclusion

Beaded depression patterns, observed in southwest Utopia Planitia resemble terrestrial thermokarst structures called beaded drainage that forms in high latitude regions on Earth. The hypothesis that Martian beaded depression patterns represent the interaction between ice wedge intersections and active pipe flow, initiated by thawing during obliquity highs, is supported by similar curvature of all beaded depression pattern types, the correlation of chain length and mean bead area, indicating chains elongate by adding depressions and a correlation between bead area and number of beads which suggests that depression growth occurs by subsidence as well as coalescence with neighbouring beads.

6.2: Future Work

Resolution of the hypothesis that there is a near-surface water layer affecting morphology of beaded depression patterns on Mars depends on more quantitative testing of Martian patterns, such as dependence of chain orientation on local slope and the distribution of depression area down individual chains. Using my hypothesis I predict that the orientation of the chains run down dip with respect to a regional slope and small variation due to local topography. Depression area would show a decrease along the chain in the direction of flow, which is dependent on the length of the chain, due to simultaneous growth of depressions and initiation of new depressions causing elongation of the chain. Another pertinent question raised by the hypothesis that beaded depression

patterns form on Mars as a direct result of subsurface pipe flow above ice wedges, is the thickness of the desiccated layer at the surface and how thickness is constrained by the beaded depression patterns that have been studied. This hypothesis provides no constraints for prediction of desiccation layer depths, however desiccation of the upper layer of Martian regolith may be centimeters thick if an impermeable layer develops due to the precipitation of salts from sublimating water. Without the indurated crust the depth to which water sublimates into the atmosphere may be too great for heat to effect ice rich regolith. Future work might also focus on modeling of heat and mass transfer through the desiccated layer to constrain its depth and composition, as well as qualitative comparisons of Mars and terrestrial patterns. Moreover, hydrodynamics and heat transfer remain poorly studied in terrestrial examples, despite their relatively widespread occurrence in permafrost lowlands.

REFERENCES

- Albee, A. L., R. E. Arvidson, F. Palluconi, and T. Thorpe, The Mars Global Surveyor Mission. *Journal of Geophysical Research E Planets*, 106, pp. 23291- 23316, 2001.
- Allen, T., Polygonal fracture networks in Utopia Planitia, Honours thesis, 150 pp., Dalhousie University, Halifax, 2004.
- Associate Committee on Geotechnical Research, *Glossary of Permafrost and related ground ice terms*, Permafrost subcommittee, National Research Council of Canada, Ottawa, Technical Memorandum 142, 1988.
- Baker, V. R., and D. J. Milton, Erosion by catastrophic floods Mars and on Earth. *Icarus*, 23, pp. 27-41, 1974.
- Bandfield, J. L., and V. E. Hamilton, and P. R. Christensen, A global view of Martian surface compositions from MGS-TES. *Science*, 287, pp. 1626-1630, 2000.
- Black, R. F., Growth of patterned ground in Victoria Land, Antarctica, in *Permafrost; North American Contribution, 2nd International Permafrost Conference*, pp. 193-203, National Academy of Science, publication 2115, Washington, D.C., 1973.
- Boynton, W. V., W. C. Feldman, S. W. Squyres, T. H. Prettyman, J. Brückner, L. G. Evans, R. C. Reedy, R. Starr, J. R. Arnold, D. M. Drake, P. A. J. Englert, A. E. Metzger, Igor Mitrofanov, J. I. Trombka, C. d'Uston, H. Wänke, O. Gasnault, D. K. Hamara, D. M. Janes, R. L. Marcialis, S. Maurice, I. Mikheeva, G. J. Taylor, R. Tokar, and C. Shinohara, Distribution of hydrogen in the near-surface of mars: evidence for subsurface ice deposits, *Science*, 297, pp. 81-85, 2002.
- Carr, M. H., The Martian drainage system and the origin of fretted channels, *Journal of Geophysical Research*, 100, pp. 7479-7507, 1995.
- Carr, M. H., *Water on Mars*, Oxford University Press, New York, 1996.
- Carr, M.H., L.S. Crumpler, J.A. Cutts, R. Greeley, J.E. Guest & H. Masursky, Martian impact craters and emplacement of ejecta by surface flow. *Journal of Geophysical Research*, 82, pp. 4055-4065, 1977.
- Carr, M.H., and G. G. Schaber, Martian Permafrost Features, *Journal of Geophysical Research*, 82, pp. 3985-4015, 1979.
- Cattermole, P., *Mars the Mystery Unfolds*, Oxford University Press, England, 2001.
- Christensen, P. R., J. L. Bandfield, V. E. Hamilton, S. W. Ruff, H. H. Kieffer, T. N. Titus, M. C. Malin, R. V. Morris, M. D. Lane, R. L. Clark, B. M. Jakosky, M. T. Mellon, J. C. Pearl, B. J. Conrath, M. D. Smith, R. T. Clancy, R. O. Kuzmin, T. Roush, G. L. Mehall, N. Gorelick, K. Bender, K. Murray, S. Dason, E. Greene, S. Silverman, and M. Greenfield,

Mars Global Surveyor Thermal Emission Spectrometer experiment; investigation description and surface science results, *Journal of Geophysical Research E planets*, 106, pp. 23823-23871, 2001.

Christensen, P. R., Formation of recent Martian gullies through melting of extensive water-rich snow deposits, *Nature*, 422, pp. 45-48, 2003.

Costard, F. M., and J. S. Kargel, Outwash plains and thermokarst on Mars. *Icarus*, 114, pp. 93-112, 1995.

Costard, F., F. Forget, N. Mangold, and J. P. Peulvast, Formation of recent Martian debris flows by melting of near-surface ground ice at high obliquity, *Science*, 295, pp. 110-113, 2002.

Dotovalov, B. N. and A. Popov, Polygonal Systems of ice wedges and conditions of their development, in *Proceedings, 1st international conference on permafrost*, pp. 102-105, National Academy of science, National Research Council of Canada, Publication 1287, Ottawa, 1966.

Fanale, F. P., J. R. Salvail, A. P. Zent and S. E. Postawko, Global distribution and migration of subsurface ice on mars, *Icarus*, 67, pp. 1-18, 1986.

Feldman, W. C., W. V. Boynton, R. L. Tokar, T. H. Prettyman, O. Gasnault, S. W. Squyres, R. C. Elphic, D. J. Lawrence, S. L. Lawson, S. Maurice, G. W. McKinney, K. R. Moore, and R. C. Reedy, Global Distribution of Neutrons from Mars: Results from Mars Odyssey, *Science*, 297, pp.75-78, 2002.

Friend, P. F. and R. Sinha, Braiding and meandering parameters, in *Braided Rivers*, Best, J.L., and C. S. Bristow (eds.), pp. 105-111, Geological Society Special Publication No. 75, 1993.

French, H. M., *The periglacial environment*. 2nd ed. Addison Wesley Longman, England, 1996.

Frey, H., K. M. Shockey, E. L. Frey, J. H. Roark, and S. E. H. Sakimoto, A very large population of likely buried impact basins in the Northern lowlands of Mars revealed by MOLA data. Lunar Planetary Science Conference XXXII, abstract 1680, 2001.
<http://www.lpi.usra.edu/meetings/lpsc2001/pdf/1680.pdf> 2001.

Greeley, R., and J. E. Guest, Geologic map of the eastern equatorial region of Mars, *USGS Misc. Inv. Ser., map I-1802B*, 1987.

Head, J. W., H. Hiesinger, M. A. Ivanov, M. A. Kreslavsky, S. Pratt, and B. J. Thomson, Possible ancient oceans on Mars: Evidence from Mars Orbiter Laser Altimeter data. *Science*, 286, pp. 2134-2137, 1999.

Head, J. W., J. F. Mustard, M. A. Kreslavsky, R. E. Milliken, and D. R. Marchant, Recent Ice Ages on Mars, *Nature*, 426, pp. 797-802, 2003.

Hiesinger, H., and J. W. Head, Characteristics and origin of polygonal terrain in southern Utopia Planitia, Mars: Results from Mars Laser Altimeter and Mars Orbiter Camera data, *Journal of Geophysical Research*, 105, pp. 11999 – 12022, 2000.

Hopkins, D. M., Thaw lakes and thaw sinks in the Imuruk Lake area, Seaward Peninsula, Alaska, *Journal of Geology*, 57, pp. 199-131, 1949.

Hopkins, D. M., T. N. V. Karlstrom, R. F. Black, J. R. Williams, T. L. Pewe, A. T. Fernold, and E. H. Muller, *Permafrost and Ground Permafrost in Alaska, A shorter Contribution to the General Geology*. Geological Survey Professional Paper 264-F, Washington, 1955.

Hynek, B. M., and R. J. Phillips, Evidence for extensive denudation of the Martian highlands. *Geology*, 29, pp. 407-410, 2001.

Jakosky, B. M., and C. B. Farmer, The seasonal and global behaviour of water vapour in the Mars atmosphere, complete results of the Viking atmospheric water detector experiment, *Journal of Geophysical Research*, 87, pp. 2999-3019, 1982.

Jakosky, B.M., M. T. Mellon, H. H. Kieffer, P. R. Christensen, E. S. Varnes, and S. W. Lee, The thermal inertia of Mars from the Mars Global Surveyor Thermal Emission Spectrometer, *Journal of Geophysical Research*, 105, pp. 9643-9652, 2000.

Jakosky, B. M., and R. J. Phillips, Mars' volatile and climate history, *Nature*, 412, pp. 237 – 244, 2001.

Jumikis, A. R., *Thermal Soil Mechanics*, N.J. RutgersUniversity Press, Canada, 1966.

Kieffer, H.H., B. M. Jakosky, C. W. Snyder, and M. S. Matthews, (eds.) *Mars*, University of Arizona Press, Tucson, 1498 pages, 1992.

Lachenbruch, A. Mechanics of thermal contraction cracks and ice wedge polygons in permafrost, Geological Society of America, Special Paper 70, Washington, 1962.

Lachenbruch, A., Contraction theory of ice wedge polygons; a qualitative discussion. Proceedings, 1st international conference on Permafrost, pp. 63-71, National Academy of Science, National research council of Canada Publication 1287. Ottawa, 1966.

Lachenbruch, A., Permafrost, in *Encyclopedia of Geomorphology*, R. W. Fairbridge (ed.), pp. 833-838, Reinhold Book Co., New York, 1968.

Lucchitta, B. K., Ice and debris in the fretted terrain, Mars, *Journal of Geophysical Research*, 89, pp. 409–418, 1984.

Lucchitta, B. K., H. M. Ferguson, and C. Summers, Sedimentary deposits in the northern lowland plains, Mars. *Journal of Geophysical Research*, 91, pp. 166-174, 1986.

Malin, M. C., G. E. Danielson, A. P. Ingersol, H. Masursky, J. Veverka, M. A. Ravine, and T. A. Soulanille, The Mars Observer Camera. *Journal of Geophysical Research*, 97, pp. 7699-7718, 1992.

Malin, M. C. and K. S. Edgett, Evidence for Recent groundwater seepage and surface runoff on Mars, *Science*, 288, pp. 2330–2335, 2000.

Malin, M. C., K. S. Edgett, Global Surveyor Mars Orbiter Camera; interplanetary cruise through primary mission. *Journal of Geophysical Research E planets*, 106, pp. 23429-23570, 2001.

Mackay, J.R., The stability of permafrost and recent climatic change in the Mackenzie valley, N.W.T., Geological Survey of Canada, Paper 75-1B, Ottawa, 1947.

Mackay, J.R., The world of underground ice, in *Annals of the Association of American Geographers*, 62, pp. 1-22, 1972.

Mackay, J.R., The closing of ice-wedge cracks in permafrost, Garry Island, Northwest Territories, *Canadian Journal of Earth Sciences*, 12, 1668-1674, 1975.

Mackay, J. R., Ice-wedge cracks, western arctic coast, *The Canadian Geographer*, 33, 365-368, 1989.

Mackay, J. R., Deformation of ice-wedge polygons, Garry Island, Northwest Territories, Geological Survey of Canada, Paper 80-1A, pp. 287-291, 1980.

MacKay, J. R., Ice wedges on hillslopes and landform evolution in the late Quaternary, western Arctic coast, *Canada Canadian Journal of Earth Sciences*, 32, pp.1093-1105, 1995.

Masarik, J. and R. C. Reedy, Gamma ray production and transport in Mars, *Journal of Geophysical Research Planets E*, 101, pp. 18891-18912, 1996.

McGill, G. E., and A. M. Dimitriou, Origin of the Martian global dichotomy by crustal thinning in the late Noachian or early Hesperian. *Journal of Geophysical Research*, 95, pp. 12595-12605, 1990.

McSween, H. Y. Jr., What have we learned about Mars from SNC meteorites? *Meteoritics*, 29, pp. 757-779, 1994.

Mellon, M. T. Thermal contraction cracks in Martian permafrost: implications for small-scale polygonal features, in *Proceedings of the Lunar and Planetary Science Conference XXVIII*, Lunar and Planetary Science Institute, Houston, 1997.

Mellon M. T., B. M. Jakosky, H. H. Kieffer, and P. R. Christensen, High Resolution Thermal Inertia Mapping From the Mars Global Surveyor Thermal Emission Spectrometer, *Icarus*, 148, pp. 437-455, 2000.

- Mellon, M. T., K. A. Kretke, M. D. Smith, and S. M. Pelkey, A global map of thermal inertia from Mars Global Surveyor mapping-mission, in *Lunar and Planetary Science XXXIII*, Abstract 1416, Lunar and Planetary Institute, Houston, 2002.
- Mitrofanov, D. A., D. Anfimov, A. Kozyrev, M. Litvak, A. Sanin, V. Tret'yakov, A. Krylov, V. Shvetsov, W. Boynton, C. Shinohara, D. Hamara, and R. S. Saunders, Maps of subsurface Hydrogen from the high-energy neutron detector, Mars Odyssey, *Science*, 297, pp. 78-81, 2002.
- Muller S. W., Permafrost or Permanently Frozen Ground and Related Engineering Problems, 2nd Ed., US Geological Survey Special Report 62, MI. 1945.
- Murton, J. B., and H. M. French, Cryostructures in Permafrost, Tuktoyaktuk coastlands, western Arctic, Canada, *Canadian Journal of Earth Sciences*, 31, pp. 737-747, 1994.
- Phillips, R. J., M. T. Zuber, S. C. Solomon, M. P. Golombek, B. M. Jakosky, W. B. Banerdt, D. E. Smith, R. M. E. Williams, B. M. Hynek, O. Aharonson, and S. A. Hauck II, Ancient Geodynamics and global-scale hydrology on Mars, *Science*, 291, pp. 2587 – 2591, 2001.
- Pieri, D., Distribution of small channels on the Martian surface, *Icarus*, 27, pp.25-50, Jan 1976
- Plug, L. J., and B. T. Werner, Fracture networks in frozen ground, *Journal of Geophysical Research*, 106, pp. 8599-8613, 2001
- Putzig, N. E., M. T. Mellon, and R. E. Arvidson, Thermophysical properties of the Martian south polar region, in 6th *International Mars Conference*, Abstract 3173, Lunar and Planetary Institute, Houston, 2003.
<http://lasp.colorado.edu/~than/research/lpsc2003/talk/>
- Scott, D. H. and C. D. Condit, Correlations; Martian stratigraphy and crater density. U.S. NASA Technical Memorandum, no.X-3511, pp.56-58, 1977.
- Scott, D. H., and K. L. Tanaka, Geological map of the western equatorial region of Mars, *USGS Misc. Inv. Ser., I-1802-A*, 1986.
- Seibert, N. M. and J. S. Kargel, Small-scale Martian polygonal terrain: Implications for liquid surface water, *Geophysical research letters*, 28, pp. 899-902, 2001.
- Shumskiy, P.A., and B.I. Vtyurin, Underground ice, in *Proceedings of the Permafrost International Conference*, pp. 108-113, National Academy of Sciences, NRC Publication 1287, Washington D. C., 1966.
- Singer, R. B., T. B. McCord, and R. N. Clark, Mars surface composition from reflectance spectra: a summary. *Journal of Geophysical Research*, 84, pp. 8415-8426. 1979.

Smith, D. E., M. T. Zuber, S. C. Solomon, R. J. Phillips, J. W. Head, J. B. Garvin, W. B. Banerdt, D. O. Muhleman, G. H. Pettengill, G. A. Neumann, F. G. Lemoine, J. B. Abshire, O. Aharonson, C. D. Brown, S. A. Hauck, A. B. Ivanov, P. J. McGovern, H. J. Zwally, and T. C. Duxbury, The global topography of Mars and implications for surface evolution, *Science*, 284, 1999.

Smith, D. E., M. T. Zuber, H. V. Frey, J. B. Garvin, J. W. Head, D. O. Muhleman, G. H. Pettengill, R. J. Phillips, S. C. Solomon, H. J. Zwally, W. B. Banerdt, T. C. Duxbury, M. P. Golombek, F. G. Lemoine, G. A. Neumann, D. D. Rowlands, O. Aharonson, P. G. Ford, A. B. Ivanov, C. L. Johnson, P. J. McGovern, J. B. Abshire, R. S. Afzal, and X. Sun, Mars Orbiter Laser Altimeter; experiment summary after the first year of global mapping of Mars, *Journal of Geophysical Research E planets*, 106, pp. 23689-23722, 2001.

Smith, D. E. and M. T. Zuber, The shape of Mars and the topographic signal of the hemispheric dichotomy. *Science*, 271. pp. 184-188. 1996.

Smith, E.I. & Elston, W. E. Martian stratigraphy and terrain classification; a basis for the geological mapping of Mars. *Eos Transactions American Geophysical Union*, 52, pp.263, 1971.

Squyres, S. W. Martian Fretted Terrain: Flow of erosional debris. *Icarus*, 34, pp. 600, 1978.

Squyres, S. W., Distribution of lobate debris aprons and similar flows on Mars, *Journal of Geophysical Research*, 84, pp. 8087-8096, 1979.

Squyres, S. W. & Carr, M. H. Geomorphic evidence for the distribution of ground ice on Mars, *Science*, 231, pp. 249-253, 1986

Squyres, S. W. & Kasting, J. F., Early Mars: How warm and how wet? *Science*, 265, pp. 744 - 749, 1994.

Tanaka, K. L., D. H. Scott, and R. Greeley, Global Stratigraphy, in *Mars*, H.H. Kieffer, B.M. Jakosky, C.W. Synder, and M.S. Matthews (eds.), pp. 354-382, University of Arizona Press, Tucson, 1992.

Van Everdingen, R. O., *Potential interactions between pipelines and terrain in a Northern environment*,. National Hydrology Research Institute, Inland Waters Directorate, Environment Canada, Paper 8, 1979.

Ward, W. R., Present obliquity oscillations of Mars: fourth order accuracy in orbital E and I, *Journal of Geophysical Research*, 84, pp. 237-241, 1979.

Ward, W. R. & Rudy, D. J. Resonant obliquity of Mars? *Icarus*, 94, pp. 160-164, 1991.

Williams, P. J., and M. W. Smith, *The Frozen Earth: Fundamentals of Geocryology*. Cambridge University Press, England, 1989.

Withers, P. and G. A. Neumann, Enigmatic northern plains of Mars. *Nature*, 410. pp. 651, 2001.

Yoshikawa, K., Origin of the polygons and the thickness of Vastitas Borealis Formation in Western Utopia Planitia on Mars, *Geophysical Research Letters*, 30, pp. 1-4, 2003.

Zent, A., Unfrozen water in the Martian regolith, AGU Eos Trans 84 (46), San Francisco, 2003.

Zuber, M.T., The crust and mantle of mars, *Nature*, 412, 2001.

APPENDIX C – Global stratigraphy of Mars

APPENDIX A – Aerial photographs used in study

19F2487

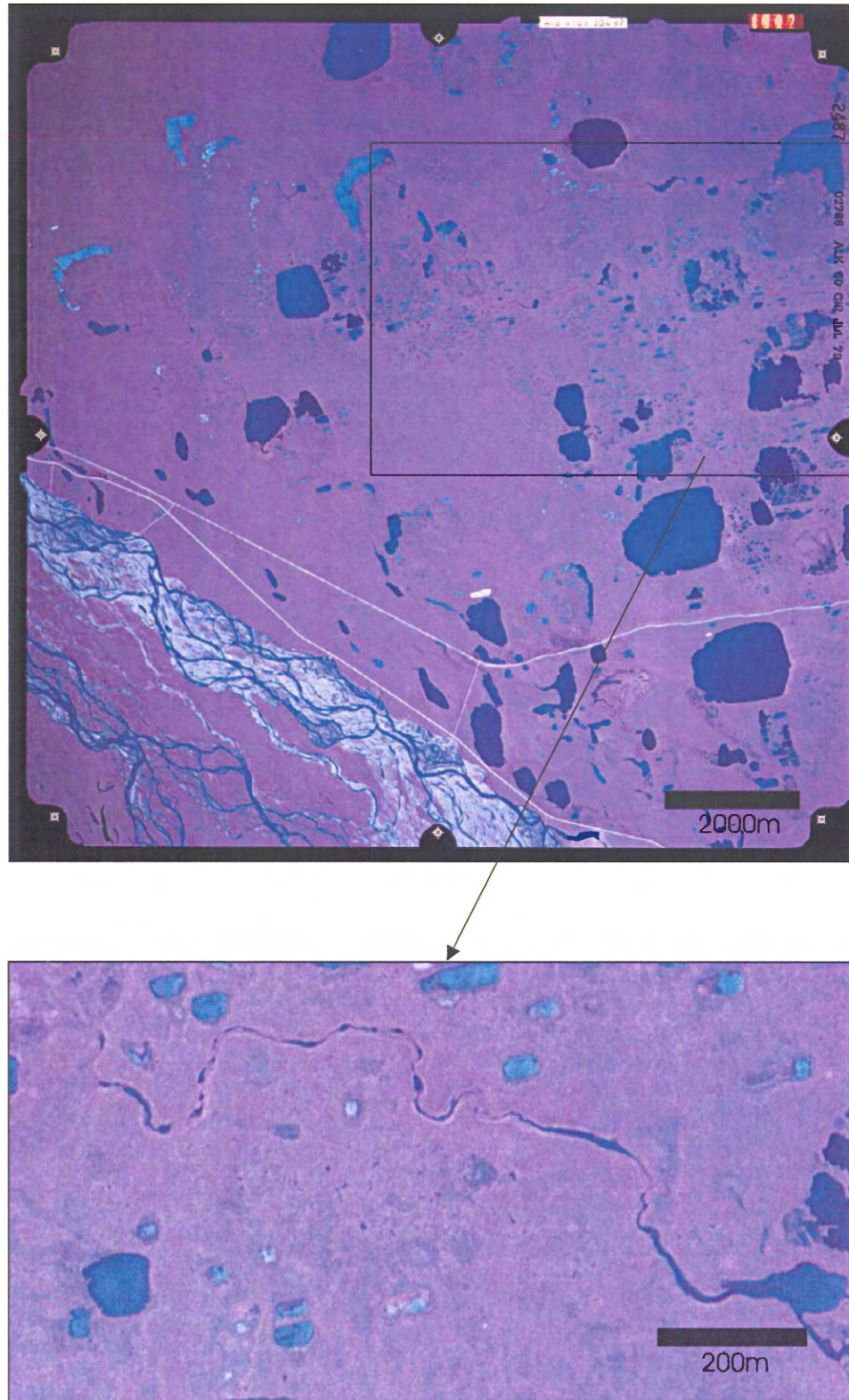


Figure A.1: Aerial photograph 19F2487. Northern Coastal Plain, Alaska. 1:60000. Box in upper image indicates the area digitised for modeling.

20F2421

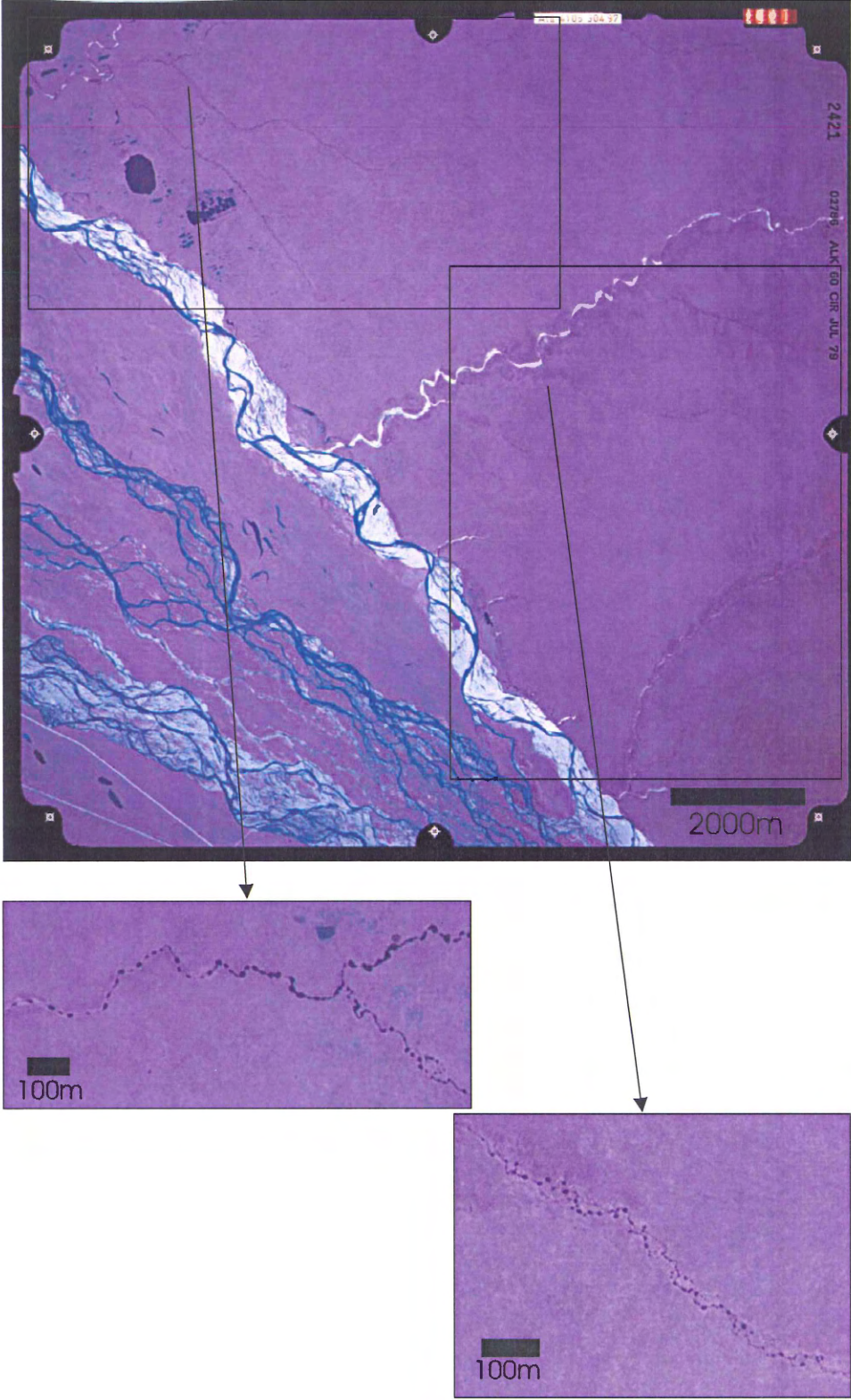


Figure A.2: Aerial photograph 20F2421. Northern Coastal Plain, Alaska. 1:60000. Box in upper image indicates the area digitised for modeling.

20F2423

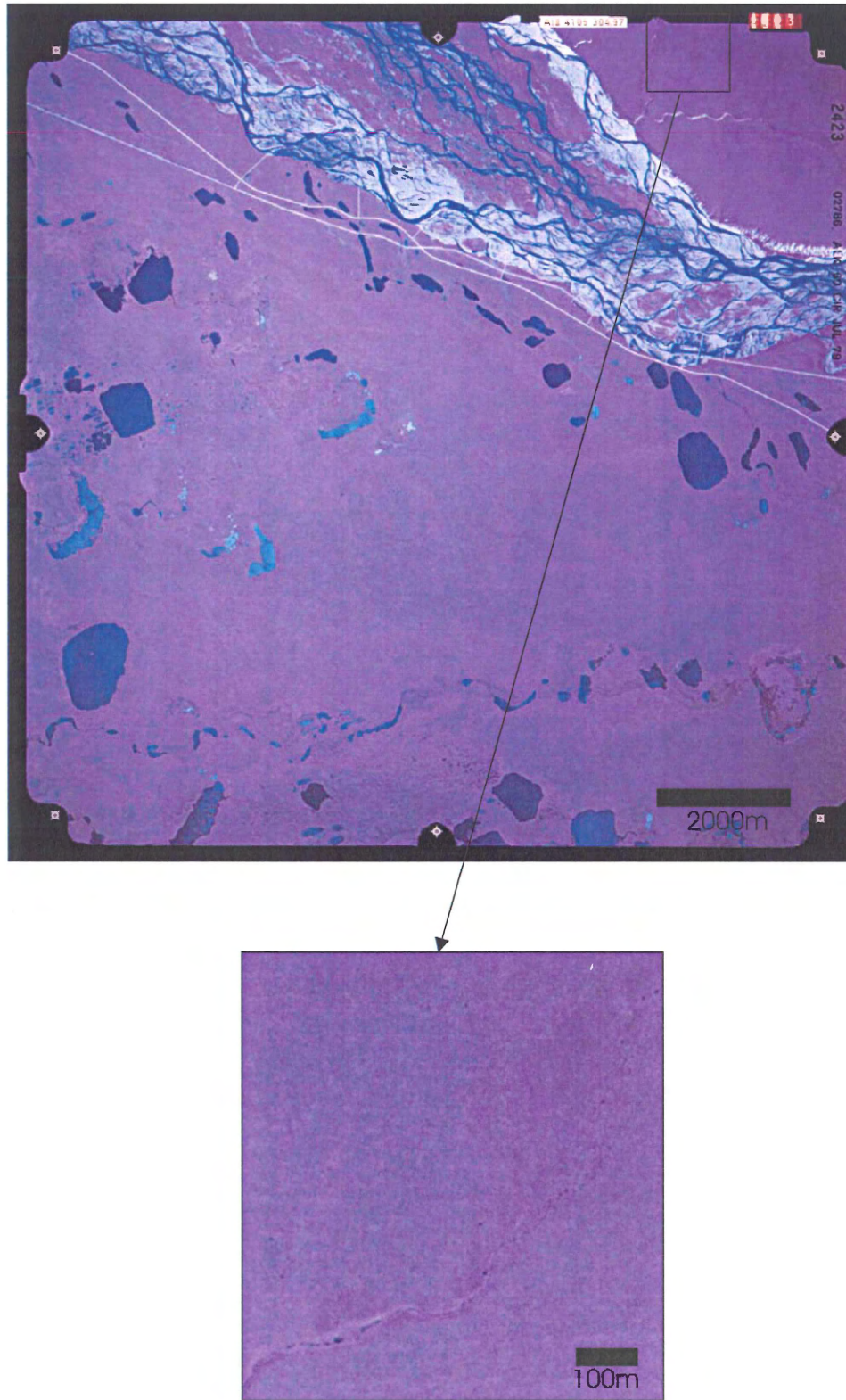


Figure A.3: Aerial photograph 20F2423. Northern Coastal Plain, Alaska. 1:60000. Box in upper image indicates the area digitised for modeling.

23F5766

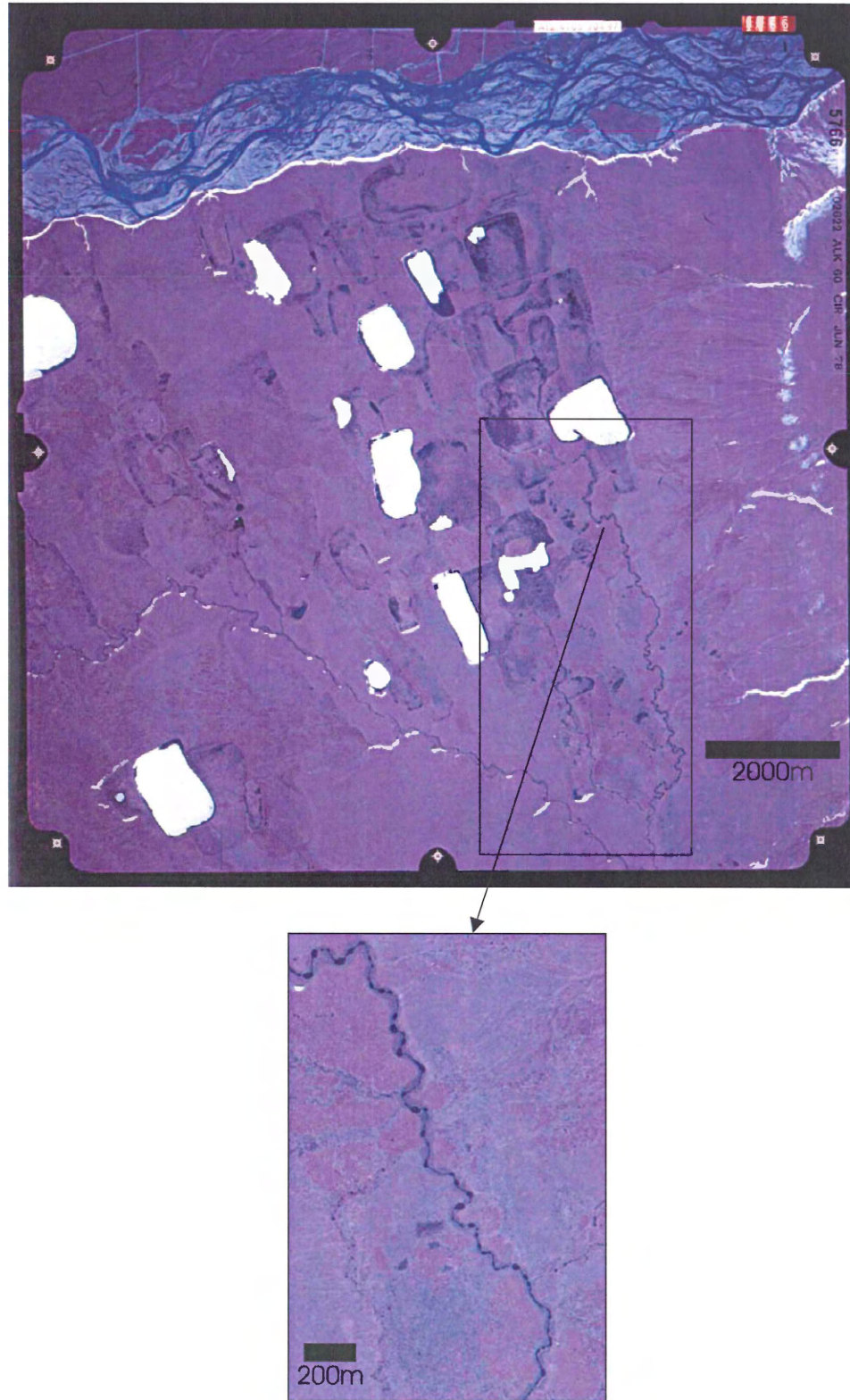
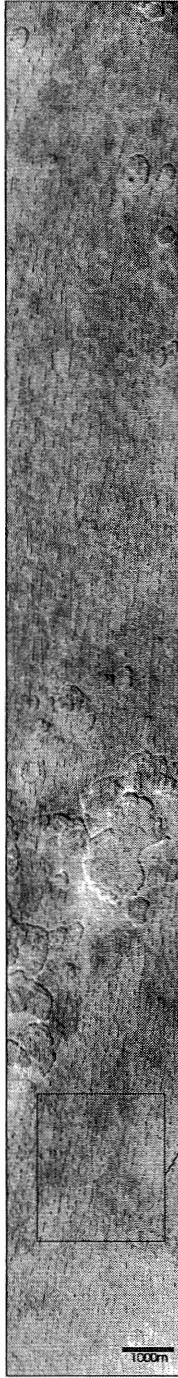


Figure A.4: Aerial photograph 23F5766. Northern Coastal Plain, Alaska. 1:60000. Box in upper image indicates the area digitised for modeling.

APPENDIX B – Mars Orbiter Camera images used in study

- Metadata included with each image includes the centre latitude and longitude which refer to the position at weighted centre of the image and upper and lower latitude and longitude define the corners of the image.
- Pixel aspect ratio is the height of each pixel in relation to the scaled pixel width, which provides the scaled width of a pixel at a given reticle point within an image. Scaled pixel width is defined as the width on the surface of the target of the projection of a pixel onto the surface.
- Emission angle provides the value of the angle between the surface normal vector at the intercept point and a vector from the intercept point to the spacecraft. The emission angle varies from 0° when the spacecraft (MGS) is viewing the sub-spacecraft point (nadir viewing) to 90° when the intercept is tangent to the surface of the target body. Thus, higher values of emission angle indicate more oblique viewing of the target.
- Incidence angle provides a measure of the lighting condition at the intercept point. Incidence angle is the angle between the local vertical at the intercept point (surface) and a vector from the intercept point to the sun. The incidence angle varies from 0 degrees when the intercept point coincides with the sub-solar point to 90 degrees when the intercept point is at the terminator (i.e., in the shadowed or dark portion of the target body). Thus, higher values of incidence angle indicate the existence of a greater number of surface shadows.

MOC IMAGE # E02-00880



Center latitude: 44.93°
Center longitude: 274.91°
Upper left latitude: 44.76°
Upper left longitude: 274.84°
Upper right latitude: 44.76°
Upper right longitude: 274.91°
Lower left latitude: 45.11°
Lower left longitude: 274.90°
Lower right latitude: 45.11°
Lower right longitude: 274.98°
Scaled pixel width: 4.69m
Pixel aspect ratio: 0.92
Emission angle: 0.19°
Incidence angle: 37.97°

Comments: Relatively flat topography, some raised/lowered features.
1 circular pattern

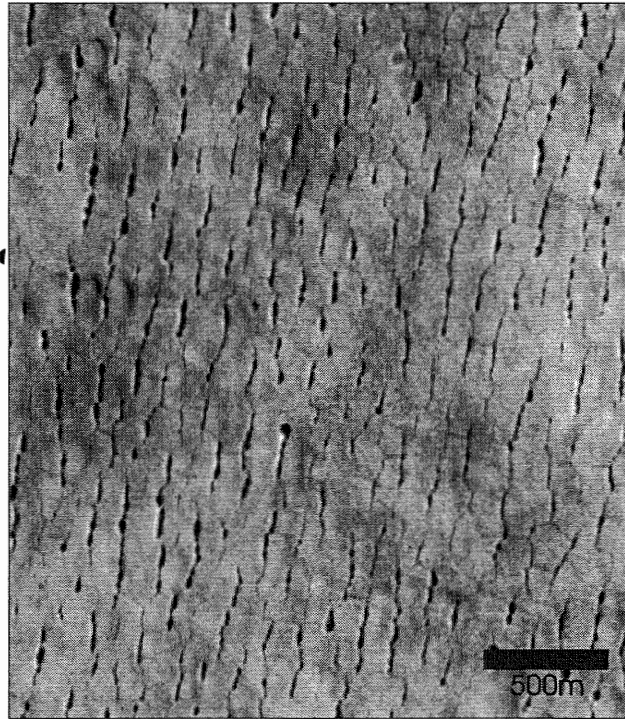


Figure B.1: Mars Orbiter Camera image E02-0080.

MOC IMAGE # E02-01703



Center latitude: 43.63°
Center longitude: 272.26°
Upper left latitude: 42.23°
Upper left longitude: 272.16°
Upper right latitude: 43.23°
Upper right longitude: 272.23°
Lower left latitude: 44.02°
Lower left longitude: 272.30°
Lower right latitude: 44.02°
Lower right longitude: 272.37°
Scaled pixel width: 4.67m
Pixel aspect ratio: 1.16
Emission angle: 0.26°
Incidence angle: 38.60°
Comments: Beads are in low-lying flat terrain. 1 double circular pattern.

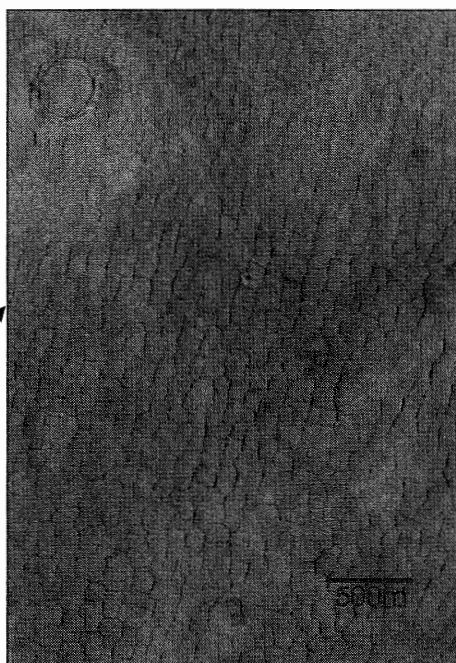


Figure B.2: Mars Orbiter Camera image E02-01703.

MOC IMAGE # E04-00442



Center latitude: 45.54°
Center longitude: 267.46°
Upper left latitude: 45.09°
Upper left longitude: 267.37°
Upper right latitude: 45.09°
Upper right longitude: 267.38°
Lower left latitude: 46.00°
Lower left longitude: 267.54°
Lower right latitude: 45.99°
Lower right longitude: 267.55°
Scaled pixel width: 4.68m
Pixel aspect ratio: 0.92
Emission angle: 0.19°
Incidence angle: 48.19°
Comments: Relatively flat topography

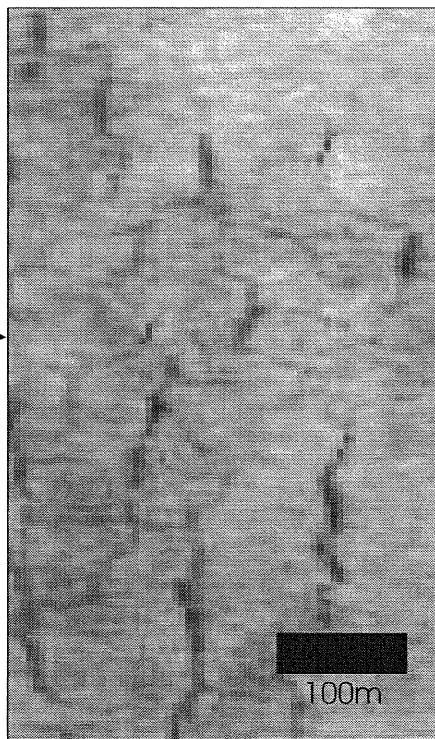
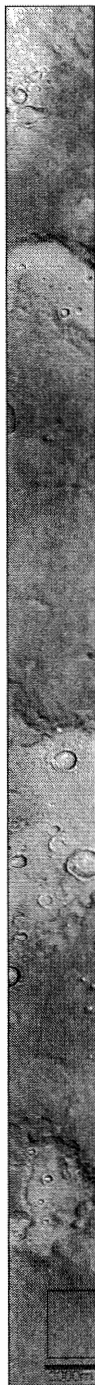


Figure B.3: Mars Orbiter Camera image E04-00442.

MOC IMAGE # E04-01564



Center latitude: 41.77°
Center longitude: 277.42°
Upper left latitude: 41.30°
Upper left longitude: 277.30°
Upper right latitude: 41.29°
Upper right longitude: 277.37°
Lower left latitude: 42.24°
Lower left longitude: 277.46°
Lower right latitude: 42.24°
Lower right longitude: 277.54°
Scaled pixel width: 6.22m
Pixel aspect ratio: 0.93
Emission angle: 0.21°
Incidence angle: 48.13°

Comments: Raised/lower topography. Impact craters present, no beads or polygons within. Some circular patterns do form around raised crater rims. 13 circular patterns.

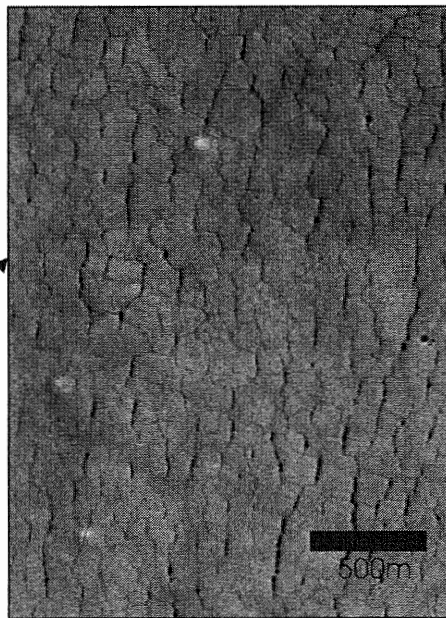
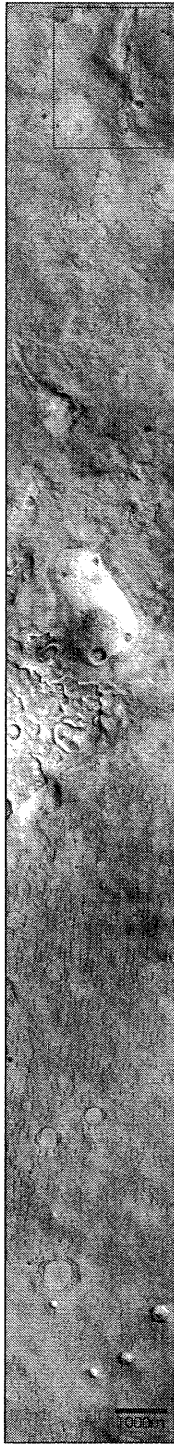


Figure B.4: Mars Orbiter Camera image E04-01564.

MOC IMAGE # E05-00488



Center latitude: 41.68°
Center longitude: 277.23°
Upper left latitude: 41.46°
Upper left longitude: 277.16°
Upper right latitude: 41.45°
Upper right longitude: 277.23°
Lower left latitude: 41.90°
Lower left longitude: 277.23°
Lower right latitude: 41.90°
Lower right longitude: 277.30°
Scaled pixel width: 4.65m
Pixel aspect ratio: 1.17
Emission angle: 0.15°
Incidence angle: 51.37°

Comments: Some raised/lowered features, smooth and rough terrain.
17 circular patterns.

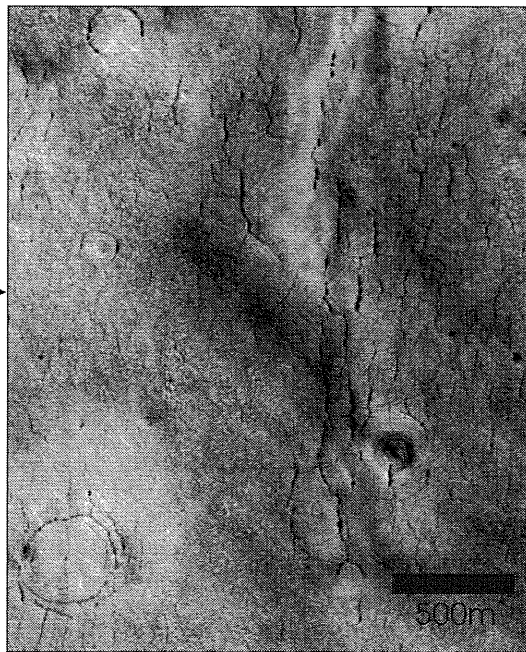


Figure B.5: Mars Orbiter Camera image E05-00488.

MOC IMAGE # E05-02576



Center latitude: 45.84°
Center longitude: 258.07°
Upper left latitude: 45.42°
Upper left longitude: 257.95°
Upper right latitude: 45.42°
Upper right longitude: 258.03°
Lower left latitude: 46.26°
Lower left longitude: 258.11°
Lower right latitude: 46.25°
Lower right longitude: 258.18°

Scaled pixel width: 4.67m

Pixel aspect ratio: 1.16

Emission angle: 0.15°

Incidence angle: 58.01°

Comments: beads dispersed through smooth and rough terrain.
6 circular patterns.

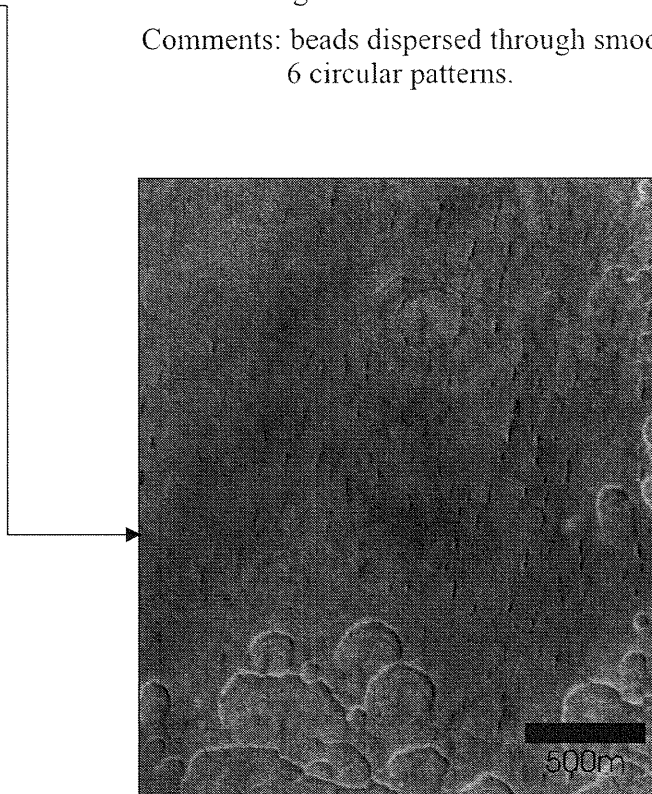


Figure B.6: Mars Orbiter Camera image E05-02576.

MOC IMAGE # M02-03335



Center latitude: 46.19°
Center longitude: 265.39°
Upper left latitude: 46.08°
Upper left longitude: 265.33°
Upper right latitude: 46.07°
Upper right longitude: 265.41°
Lower left latitude: 46.31°
Lower left longitude: 265.37°
Lower right latitude: 46.31°
Lower right longitude: 265.45°

Scaled pixel width: 3.11m

Pixel aspect ratio: 1.39

Emission angle: 0.18°

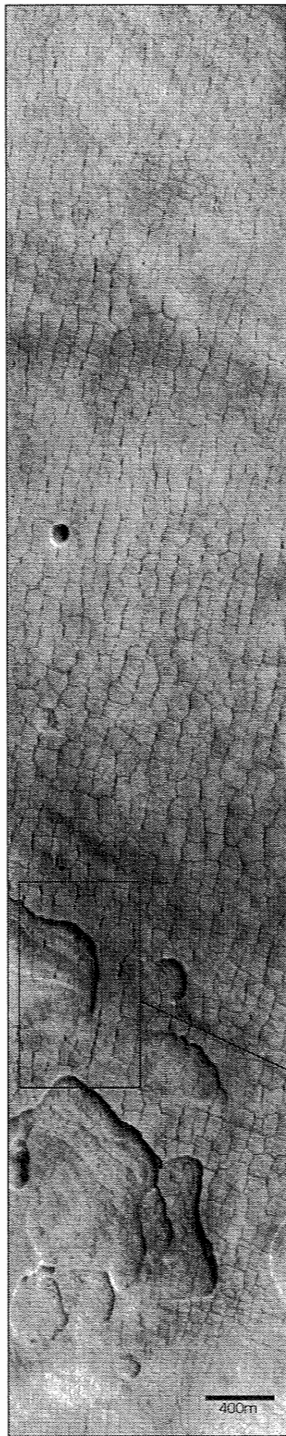
Incidence angle: 48.51°

Comments: Some raised/low features.



Figure B.7: Mars Orbiter Camera image M022-03335.

MOC IMAGE # M03-04331



Center latitude: 44.46°
Center longitude: 272.8°
Upper left latitude: 44.41°
Upper left longitude: 272.77°
Upper right latitude: 44.40°
Upper right longitude: 272.80°
Lower left latitude: 44.52°
Lower left longitude: 272.79°
Lower right latitude: 44.52°
Lower right longitude: 272.83°
Scaled pixel width: 3.09m
Pixel aspect ratio: 0.94
Emission angle: 0.16°
Incidence angle: 53.56°

Comments: Relatively flat topography, some raised/lowered features.

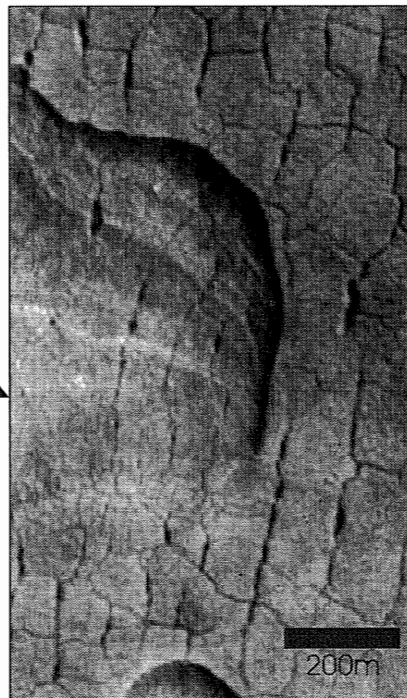


Figure B.8: Mars Orbiter Camera image M03-04331.

MOC IMAGE # M03-05604



Center latitude: 46.27°
Center longitude: 264.24°
Upper left latitude: 45.57°
Upper left longitude: 264.07°
Upper right latitude: 45.56°
Upper right longitude: 264.15°
Lower left latitude: 46.98°
Lower left longitude: 264.34°
Lower right latitude: 46.98°
Lower right longitude: 264.41°

Scaled pixel width: 6.2m

Pixel aspect ratio: 1.40

Emission angle: 0.19°

Incidence angle: 55.56°

Comments: Relatively flat topography, some raised/lowered features.



Figure B.9: Mars Orbiter Camera image M03-05064.

MOC IMAGE # M03-05694



Center latitude: 45.43°
Center longitude: 271.80°
Upper left latitude: 45.21°
Upper left longitude: 271.74°
Upper right latitude: 45.21°
Upper right longitude: 271.76°
Lower left latitude: 45.65°
Lower left longitude: 271.83°
Lower right latitude: 45.65°
Lower right longitude: 271.85°
Scaled pixel width: 1.55m
Pixel aspect ratio: 1.4
Emission angle: 0.14°
Incidence angle: 55.67°

Comments: Beads at the bottom of the image. Relatively flat topography, some raised/lowered features.

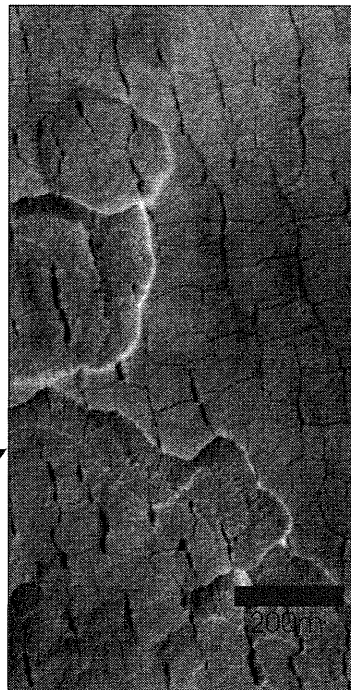


Figure B.10: Mars Orbiter Camera image M03-05694.

MOC IMAGE # M04-00990



Center latitude: 45.75°
Center longitude: 265.15°
Upper left latitude: 45.69°
Upper left longitude: 265.12°
Upper right latitude: 45.69°
Upper right longitude: 265.15°
Lower left latitude: 45.81°
Lower left longitude: 265.14°
Lower right latitude: 45.81°
Lower right longitude: 265.18°
Scaled pixel width: 3.1m
Pixel aspect ratio: 0.95
Emission angle: 0.27°
Incidence angle: 59.37°

Comments: Relatively flat topography, some raised/low features. 2 parallel chains (river pattern).

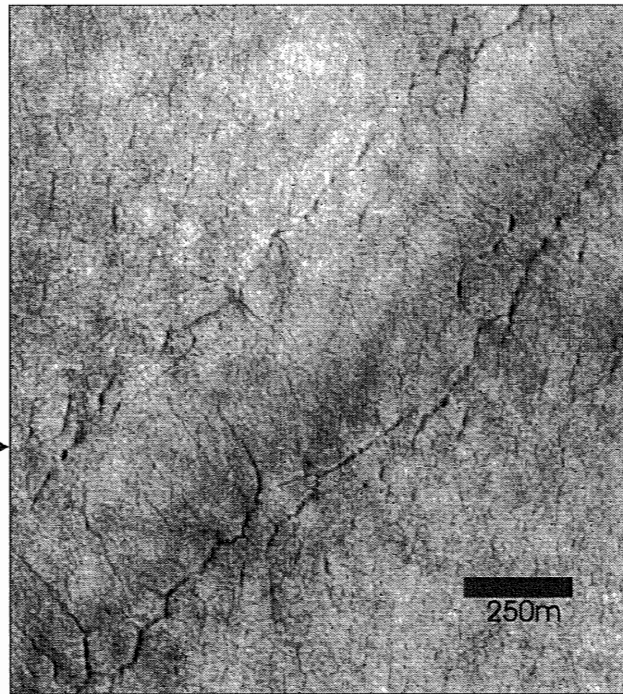


Figure B.11: Mars Orbiter Camera image M04-00990.

MOC IMAGE # M04-01440



Center latitude: 45.77°
Center longitude: 260.79°
Upper left latitude: 45.05°
Upper left longitude: 260.63°
Upper right latitude: 45.05°
Upper right longitude: 260.70°
Lower left latitude: 46.49°
Lower left longitude: 260.89°
Lower right latitude: 46.48°
Lower right longitude: 260.96°

Scaled pixel width: 6.21m

Pixel aspect ratio: 0.94

Emission angle: 0.18°

Incidence angle: 59.82°

Comments: Relatively flat topography, smooth and rough terrain
some raised/low features.

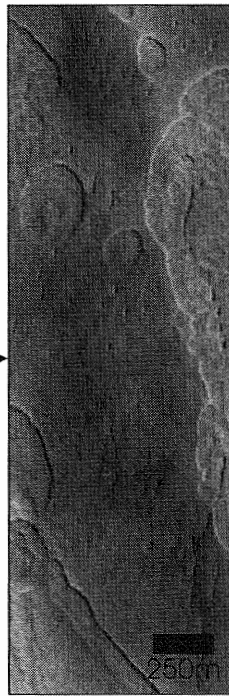


Figure B.12: Mars Orbiter Camera image M04-01440.

MOC IMAGE # M04-01631



Center latitude: 44.33°
Center longitude: 272.68°
Upper left latitude: 43.76°
Upper left longitude: 272.55°
Upper right latitude: 43.75°
Upper right longitude: 272.63°
Lower left latitude: 44.92°
Lower left longitude: 272.76°
Lower right latitude: 44.92°
Lower right longitude: 272.84°
Scaled pixel width: 6.19m
Pixel aspect ratio: 0.90
Emission angle: 0.34°
Incidence angle: 59.09°
Comments: Some raised/lowered features. 4 circular pattern

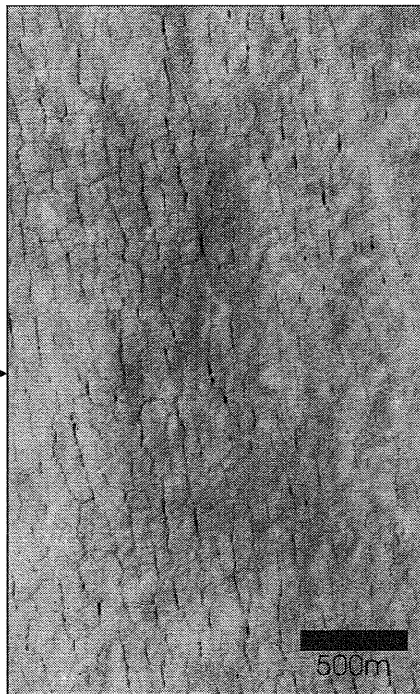
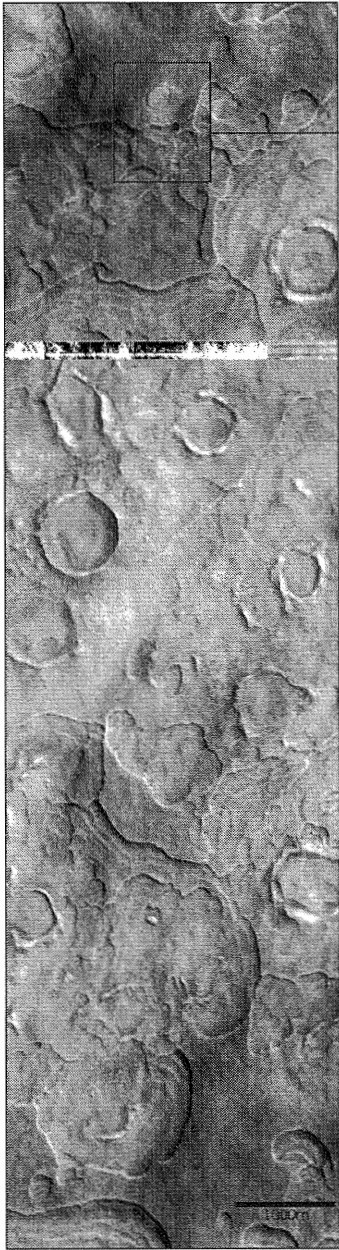


Figure B.13: Mars Orbiter Camera image M04-01631.

MOC IMAGE # M04-02077



Center latitude: 45.52 °
Center longitude: 268.56 °
Upper left latitude: 45.43 °
Upper left longitude: 268.50 °
Upper right latitude: 45.43 °
Upper right longitude: 268.58 °
Lower left latitude: 45.61 °
Lower left longitude: 268.54 °
Lower right latitude: 45.60 °
Lower right longitude: 268.61 °
Scaled pixel width: 3.10m
Pixel aspect ratio: 0.94
Emission angle: 0.18 °
Incidence angle: 60.3 °

Comments: Rough and smooth terrain, some raised/lowered features.

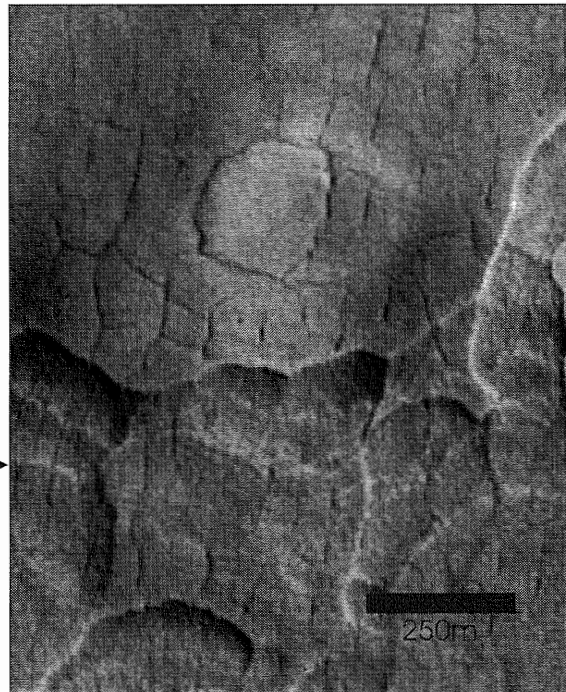
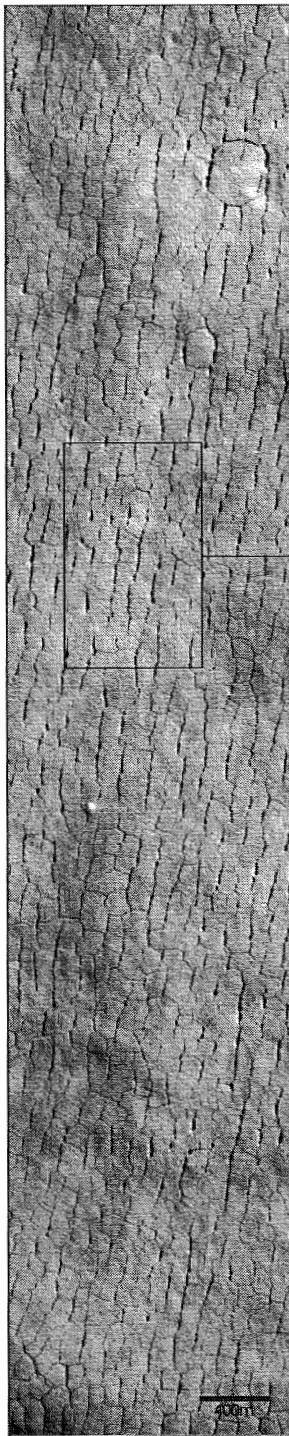


Figure B.14: Mars Orbiter Camera image M04-02077.

MOC IMAGE # M04-02704



Center latitude: 44.09 °
Center longitude: 276.14 °
Upper left latitude: 44.03 °
Upper left longitude: 276.11 °
Upper right latitude: 44.03 °
Upper right longitude: 276.15 °
Lower left latitude: 44.15 °
Lower left longitude: 276.13 °
Lower right latitude: 44.15 °
Lower right longitude: 276.17 °
Scaled pixel width: 3.09m
Pixel aspect ratio: 0.95
Emission angle: 0.15 °
Incidence angle: 59.97 °
Comments: Relatively flat topography, 1 circular pattern.

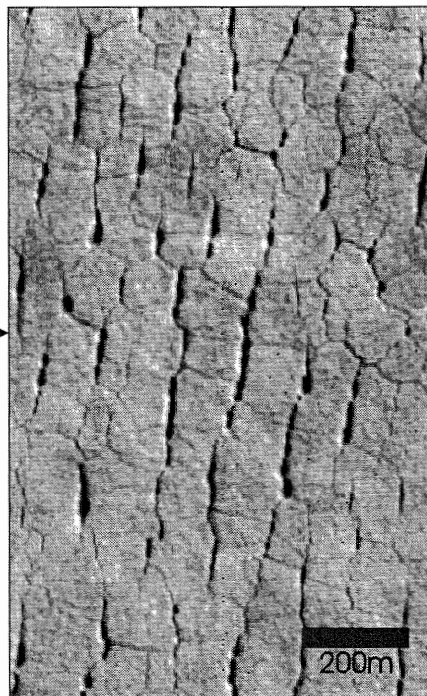


Figure B.15: Mars Orbiter Camera image M04-02704.

MOC IMAGE # M04-03810



Center latitude: 42.56°
Center longitude: 279.32°
Upper left latitude: 42.50°
Upper left longitude: 279.29°
Upper right latitude: 42.50°
Upper right longitude: 279.33°
Lower left latitude: 42.62°
Lower left longitude: 279.31°
Lower right latitude: 42.62°
Lower right longitude: 279.35°

Scaled pixel width: 3.09m

Pixel aspect ratio: 0.95

Emission angle: 0.15°

Incidence angle: 59.99°

Comments: Relatively flat topography, some raised/lowered features.

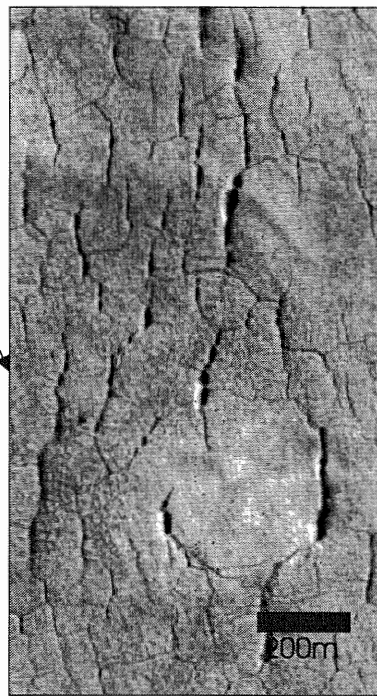
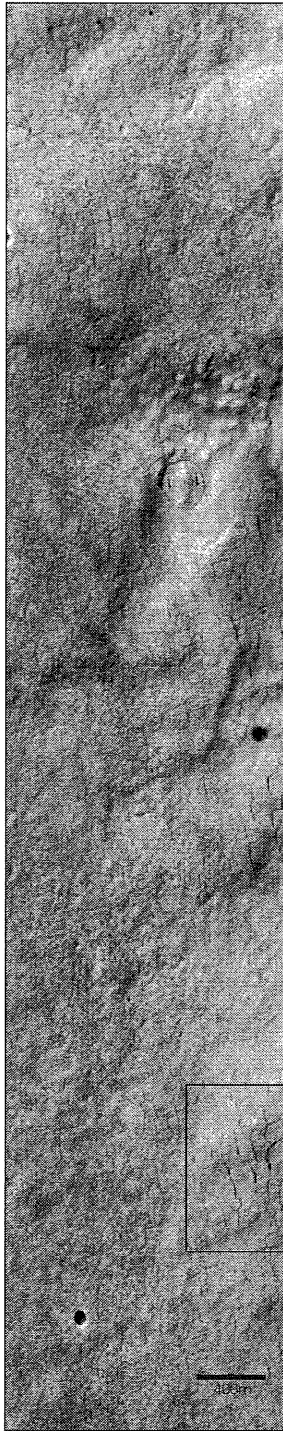


Figure B.16: Mars Orbiter Camera image M04-03810.

MOC IMAGE # M04-04181



Center latitude: 41.93 °
Center longitude: 274.87 °
Upper left latitude: 41.87 °
Upper left longitude: 274.84 °
Upper right latitude: 41.87 °
Upper right longitude: 274.88 °
Lower left latitude: 41.99 °
Lower left longitude: 274.86 °
Lower right latitude: 41.99 °
Lower right longitude: 274.90 °
Scaled pixel width: 3.08m
Pixel aspect ratio: 0.94
Emission angle: 0.10 °
Incidence angle: 59.97 °

Comments: Relatively flat topography, smooth and rough terrain. 2 circular patterns.

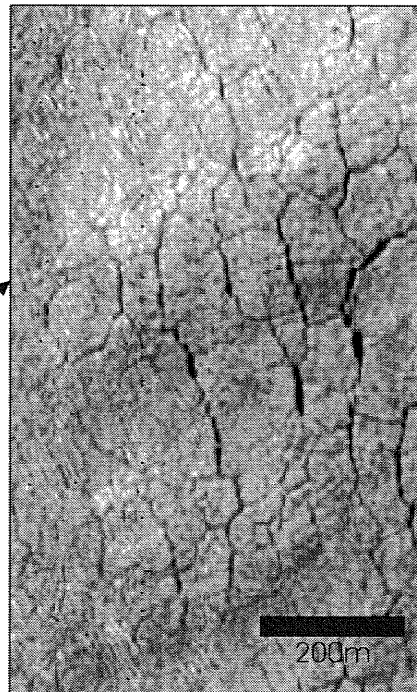
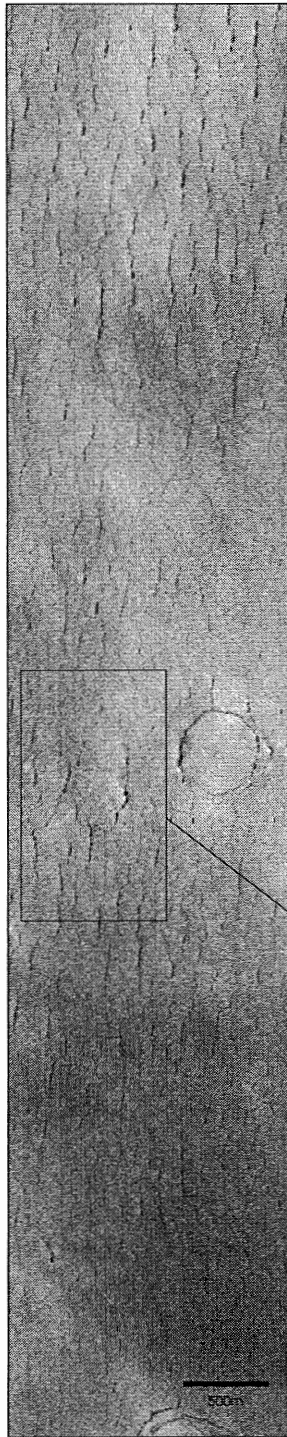


Figure B.17: Mars Orbiter Camera image M04-04181.

MOC IMAGE # M08-03534



Center latitude: 41.95°
Center longitude: 277.15°
Upper left latitude: 41.90°
Upper left longitude: 277.12°
Upper right latitude: 41.89°
Upper right longitude: 277.15°
Lower left latitude: 42.01°
Lower left longitude: 277.14°
Lower right latitude: 42.01°
Lower right longitude: 277.17°

Scaled pixel width: 3.08m

Pixel aspect ratio: 0.94

Emission angle: 0.14°

Incidence angle: 67.74°

Comments: Relatively flat topography. 1 circular pattern.

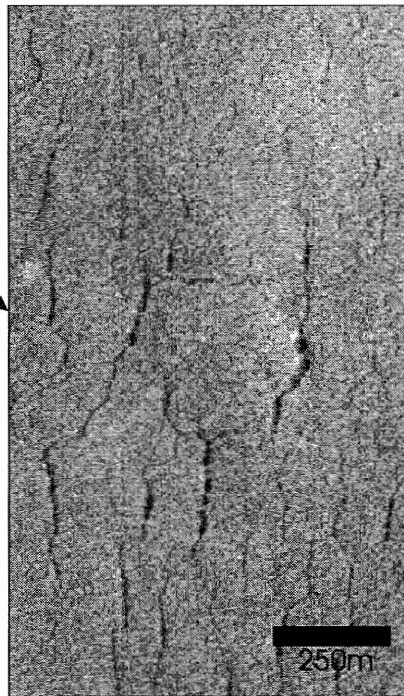


Figure B.18: Mars Orbiter Camera image M08-03534.

MOC IMAGE # M08-07602



Center latitude: 45.14°
Center longitude: 275.80°
Upper left latitude: 45.08°
Upper left longitude: 275.77°
Upper right latitude: 45.08°
Upper right longitude: 275.81°
Lower left latitude: 45.20°
Lower left longitude: 275.79°
Lower right latitude: 45.20°
Lower right longitude: 275.83°
Scaled pixel width: 3.10m
Pixel aspect ratio: 0.93
Emission angle: 0.18°
Incidence angle: 71.95°

Comments: Relatively flat topography, some raised/lowered features, beads present on all topography.

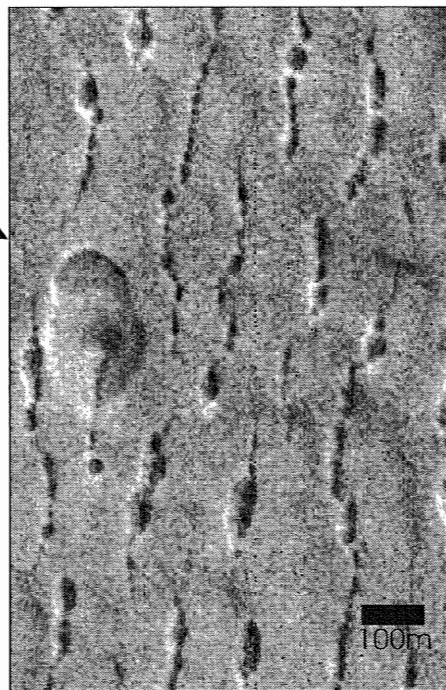
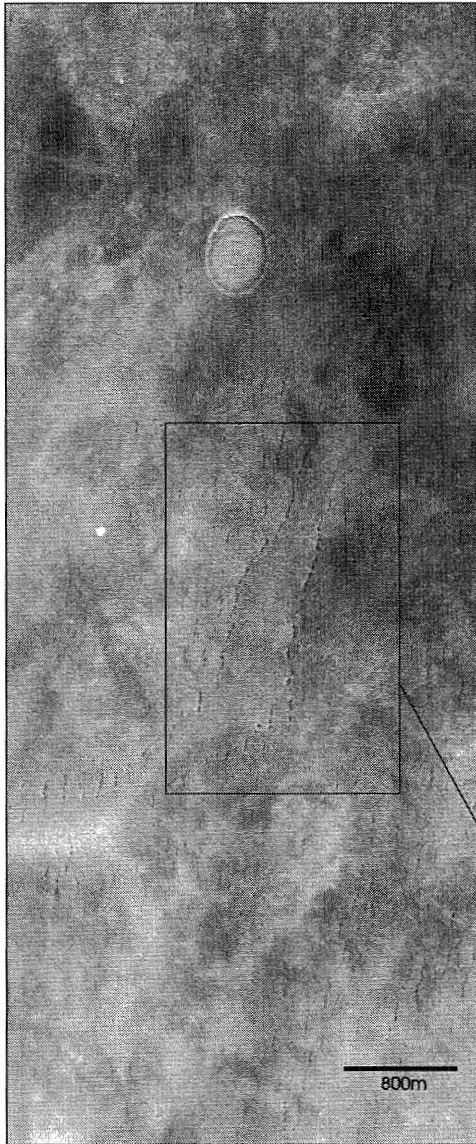


Figure B.19: Mars Orbiter Camera image M08-07602.

MOC IMAGE # M15-00675



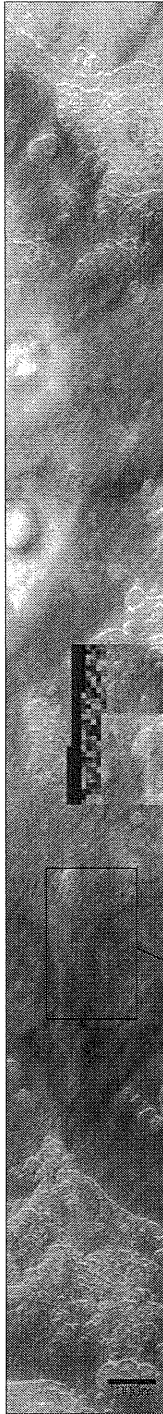
Center latitude: 45.44°
Center longitude: 263.77°
Upper left latitude: 45.38°
Upper left longitude: 263.72°
Upper right latitude: 45.38°
Upper right longitude: 263.79°
Lower left latitude: 45.50°
Lower left longitude: 263.74°
Lower right latitude: 45.49°
Lower right longitude: 263.81°
Scaled pixel width: 3.10m
Pixel aspect ratio: 0.93
Emission angle: 0.19°
Incidence angle: 51.87°

Comments: Relatively flat topography.
2 long parallel chains (river pattern).



Figure B.20: Mars Orbiter Camera image M15-00675.

MOC IMAGE # M18-00441



Center latitude: 46.25°
Center longitude: 259.9°
Upper left latitude: 46.05°
Upper left longitude: 259.90°
Upper right latitude: 46.05°
Upper right longitude: 259.98°
Lower left latitude: 46.46°
Lower left longitude: 259.98°
Lower right latitude: 46.46°
Lower right longitude: 260.06°
Scaled pixel width: 6.22m
Pixel aspect ratio: 0.93
Emission angle: 0.21°
Incidence angle: 38.18°

Comments: Beads present on both smooth and rough terrain.

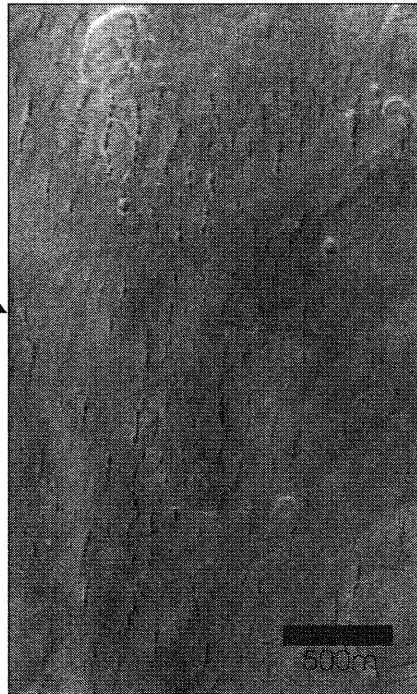


Figure B.21: Mars Orbiter Camera image M18-00441.

MOC IMAGE # M19-01326



Center latitude: 44.35°

Center longitude: 272.11°

Upper left latitude: 44.33°

Upper left longitude: 272.09°

Upper right latitude: 44.33°

Upper right longitude: 272.12°

Lower left latitude: 44.33°

Lower left longitude: 272.10°

Lower right latitude: 44.37°

Lower right longitude: 272.13°

Scaled pixel width: 1.55m

Pixel aspect ratio: 0.93

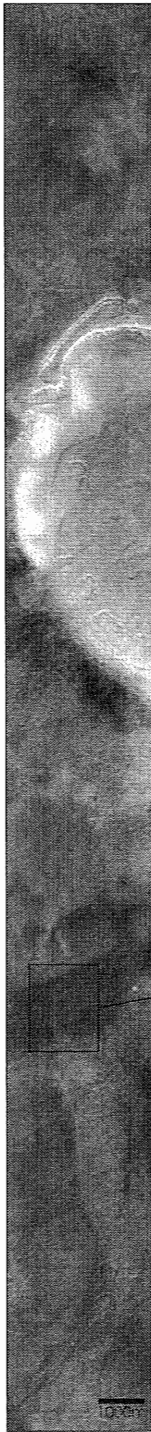
Emission angle: 0.15°

Incidence angle: 33.2 °

Comments: Relatively flat topography,
maybe a depression at the
center of the image. 1 circular
pattern

Figure B.22: Mars Orbiter Camera image M19-01326.

MOC IMAGE # M19-01929



Center latitude: 43.71°
Center longitude: 267.16°
Upper left latitude: 43.47°
Upper left longitude: 267.08°
Upper right latitude: 43.47°
Upper right longitude: 267.15°
Lower left latitude: 43.94°
Lower left longitude: 267.16°
Lower right latitude: 43.94°
Lower right longitude: 267.24°
Scaled pixel width: 6.19m
Pixel aspect ratio: 0.96
Emission angle: 0.34°
Incidence angle: 32.37°

Comments: Relatively flat topography, some raised/lowered features.
1 circular pattern and 2 parallel chains (river pattern).

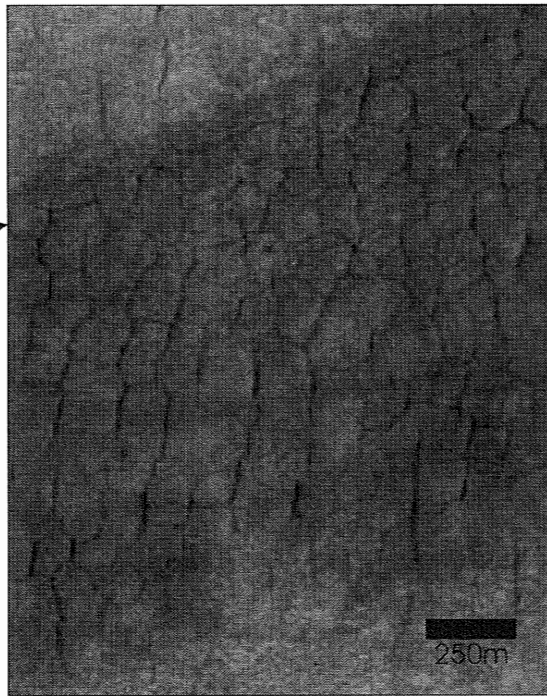
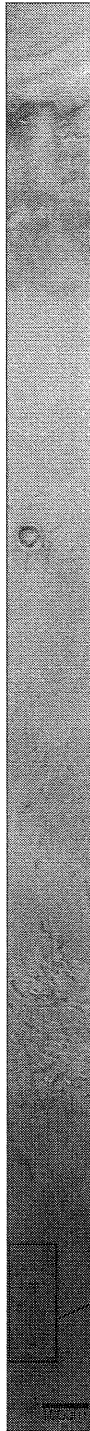


Figure B.23: Mars Orbiter Camera image M19-01929.

MOC IMAGE # M23-00151



Center latitude: 42.19 °
Center longitude: 272.59 °
Upper left latitude: 42.00 °
Upper left longitude: 272.53 °
Upper right latitude: 42.00 °
Upper right longitude: 272.57 °
Lower left latitude: 42.39 °
Lower left longitude: 272.60 °
Lower right latitude: 42.39 °
Lower right longitude: 272.64 °

Scaled pixel width: 3.09m

Pixel aspect ratio: 0.94

Emission angle: 0.28 °

Incidence angle: 31.51 °

Comments: Beads present in smooth topography.

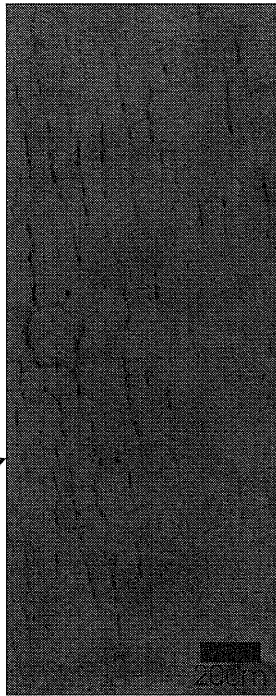


Figure B.24: Mars Orbiter Camera image M23-00151.

APPENDIX C – Global stratigraphy of Mars

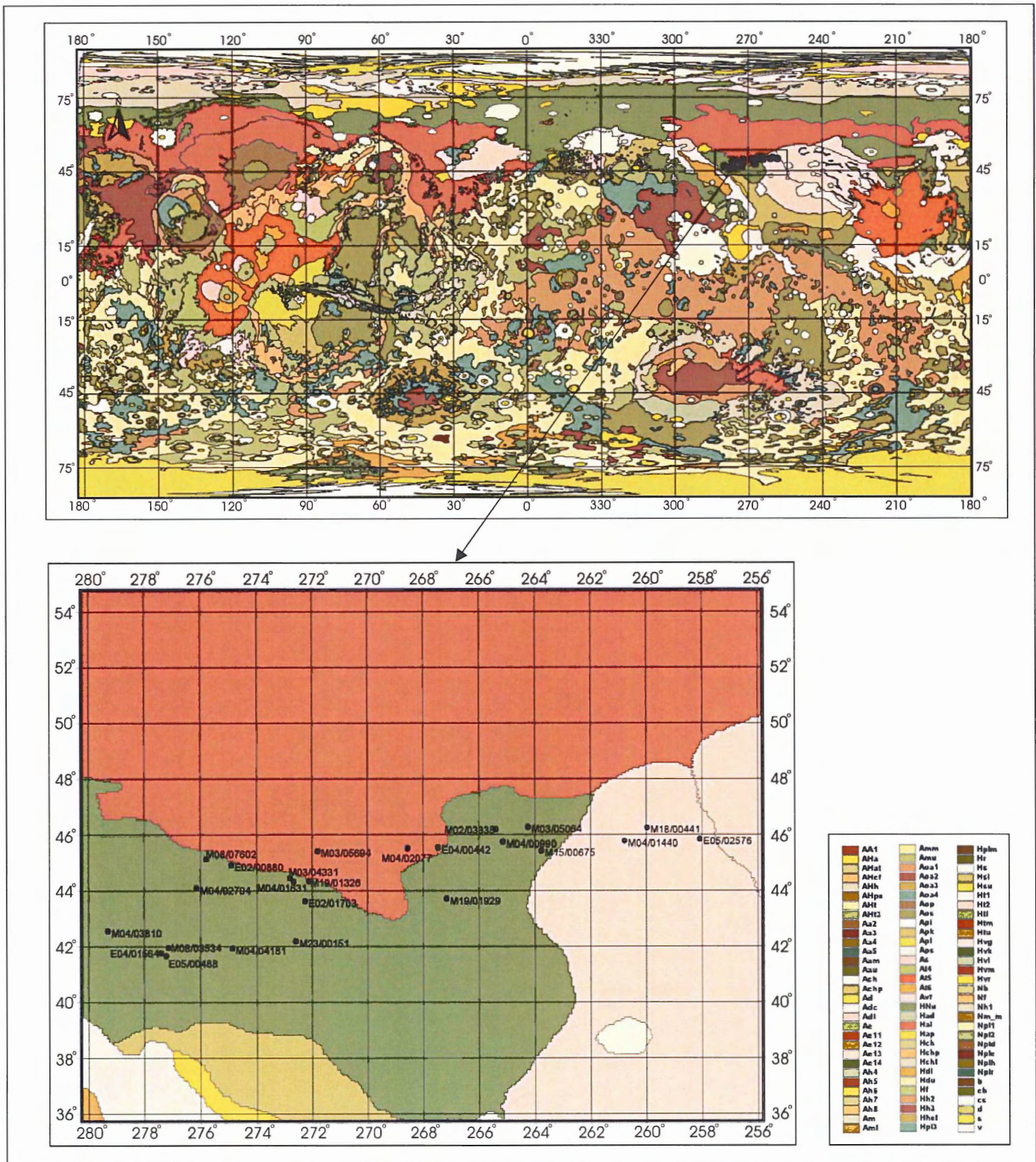


Figure C.1: Mars global stratigraphy (after Scott and Tanaka, 1986; Greeley and Guest, 1987).

Stratigraphic Unit Descriptions to Accompany Mars Global Stratigraphy Map

SURFICIAL DEPOSITS

As **SLIDE MATERIAL:** Smooth to lobate flow material associated with some scarps and crater rims; especially well developed along channel walls in Deuteronilus Mensae region. Forms aprons along scarps and around knobs and mesas; may completely cover channel floors. Primarily equivalent to third type of slide material mapped by Scott and Tanaka (1986). No specific type area. **Interpretation:** Unconsolidated material, such as debris flows, resulting from mass wasting

Achu **YOUNGER CHANNEL AND FLOOD-PLAIN MATERIAL, UNDIVIDED:** In eastern equatorial part of map area; forms plain as wide as 600 km marked by dark, sinuous, intertwining albedo patterns; appears more mottled westward. Type areas (Scott and Tanaka, 1986): lat 15° N., long 177° (younger channel material) and lat 22°N., long 171° (flood-plain material). **Interpretation:** Fluvial deposits; distinct albedo patterns probably represent channels with bars and islands; mottled zones in western part may represent deposition from ponded terminus of fluvial system

Ad **DUNE MATERIAL:** Patches of barchan and other types of dunes on crater floors. Makes up part of dunes and dune-capped material (unit Ad) of south polar region (Tanaka and Scott, 1987). Type area: lat 48° S., long 329°. **Interpretation:** Sand deposited in areas of low wind strength

LOWLAND TERRAIN MATERIALS:

Consist of all plains-forming units between highland-lowland boundary scarp and north edge of map area, as well as materials of eastern volcanic assemblage.

Northern plains assemblage Materials deposited in widespread sheets on northern plains. Within each formation, members mapped on basis of morphology, albedo, and crater size-frequency distribution; some contacts approximately located. This assemblage postdates formation of highland-lowland boundary scarp (Scott, 1979).

Aps **SMOOTH PLAINS MATERIAL:** Forms patches and regions of flat, featureless plains;lightly cratered. Type area: lat 9° N., long 222°. **Interpretation:** Probably of diverse origin; many exposures probably consist of eolian deposits

AHpe **ETCHED PLAINS MATERIAL:** Occurs as patches in Elysium Planitia. Surface characterized by irregular mesas and pits. Type area: lat 15°N., long 238°. **Interpretation:** Plains deposits mantled by eolian material that has subsequently been eroded, possibly by wind

ARCADIA FORMATION: Forms low-lying plains (1) in Arcadia Planitia east of Phlegra Montes in

east margin of map area and (2) in Acidalia Planitia as small patch in west margin. Common boundaries of older members mapped arbitrarily in places. Flows with lobate margins, ridges, and channels and small hills with summit craters visible in some areas. Members 2 and 5 as defined by Scott and Tanaka (1986) not present in map area.

Interpretation: Mostly lava flows and small volcanoes

Aa4 Member 4 In Arcadia Planitia; overlies member 3. Type area: lat 45° N., long 175° (Scott and Tanaka, 1986)

Aa3 Member 3 In and north of Arcadia Planitia along east margin of map area. Flow fronts visible in places. Type area: lat 15° N., long 155° (Scott and Tanaka, 1986)

Aa1 Member 1 Near west and east borders of map area. Type area: lat 30° N., long 40° (Scott and Tanaka, 1986)

MEDUSAE FOSSAE FORMATION: Occurs near equator in eastern part of map area. Consists of extensive, relatively flat sheets, generally smooth to grooved and gently undulating; albedo moderate (Scott and Tanaka, 1986). Locally, where upper or middle member stripped by wind, underlying member shows lineations

Amu Upper member: Surfaces smooth, flat to rolling, light in color; sculptured into ridges and grooves in places; broadly curved margins, locally eroded into serrated scarps. Type area: lat 0° N., long 160° (Scott and Tanaka, 1986).

Interpretation: Thick deposits of eolian sediments or volcanic pyroclastic deposits; wind eroded, particularly along margins, to form yardangs

Amm Middle member: Similar to upper member but in places surface is more rugged and eroded. Type area: lat 10° N., long 160° (Scott and Tanaka, 1986).

Interpretation: Poorly to moderately indurated eolian or pyroclastic deposits; wind eroded, particularly along margins

Aml Lower member: Most widespread member in map area. Surfaces smooth to rough and highly eroded, darker than those of other members. One area centered at lat 1° S., long 182° contains long, broad troughs. Type area: lat 0° N., long 174° (Scott and Tanaka, 1986).

Interpretation: Lava flows interbedded with eolian or pyroclastic deposits, in places heavily eroded

VASTITAS BOREALIS FORMATION Subpolar plains deposits of northern lowlands; members distinguished on basis of morphology and albedo contrast; placement of contacts locally arbitrary (Scott and Tanaka, 1986)

Hvm Mottled member: Major occurrence north of map boundary (Tanaka and Scott, 1987); extends as far south as about lat 430° N. Crater-ejecta blankets have higher albedo than adjacent terrain, giving mottled appearance. In places, gently rolling, closely spaced hills averaging 5 km in diameter can be distinguished. Type area: lat 550° N., long 40 (Scott and Tanaka, 1986).

Interpretation: Possibly lava flows erupted from fissures, or of alluvial or eolian origin

Hvg Grooved member: Occurs as isolated patches in several areas of lowland plains; similar to

mottled member but marked by curvilinear and polygonal patterns of grooves and troughs; closed polygons as wide as 20 km. Ridges present in center of some grooves, as at lat 53° N., long 295°. Type area: lat 45° N., long 15° (Scott and Tanaka, 1986).

Interpretation: Material same as mottled member; patterns may be due to compaction, tectonism, or periglacial processes

Hvr Ridged member: Isolated patches in northern plains. Characterized by concentric, low ridges about 1 to 2 km wide; northwest of Deuteronilus Mensae, many ridges are within depressions. In Isidis basin, member displays low mounds, many of which are aligned. Type area: lat 38° N., long 33° (Scott and Tanaka, 1986).

Interpretation: Material same as mottled member; unit appears to develop from erosion of surrounding units. Origin of ridges unknown but they may result from periglacial or erosional processes. Low mounds in Isidis basin may represent spatter cones along lines of vents

Hvk Knobby member: Similar in appearance to mottled member but generally has higher albedo and abundant small, dark, knoblike hills, some with summit craters. Crater ejecta have albedo similar to that of surrounding terrain. Type area: lat 55° N., long 5° (Scott and Tanaka, 1986).

Interpretation: Plains of diverse origins (volcanic flows, eolian mantles); hills may be small volcanoes, remnants of highland terrain or of crater rims, or pingos

Eastern volcanic assemblage

Volcanoes and lava flows in Elysium region (Greeley and Spudis, 1981).

ELYSIUM FORMATION Units associated with Elysium Mons.

Ael4 Member 4 Channel material. Type area: lat 36.9° N., long 220°. Interpretation: May be derived from lahars of members 1 and 3 (Christiansen and Greeley, 1981)

Ael3 Member 3 Forms plains having rugged relief, hummocky surfaces; lobate deposits seen at high resolution. Type area: lat 43° N., long 230°.

Interpretation: Of volcanic origin; flows possibly derived from Elysium Mons, possibly interfinger with member 1. Extensively modified by fluvial, eolian, and periglacial processes

Ael2 Member 2 Lobate deposits, with rilles, composing Elysium Mons edifice. Gradational with member 1. Type area: lat 25° N., long 215°.

Interpretation: Lava flows displaying channels and partly collapsed lava tubes

Ael1 Member 1 Lobate, plains-forming deposits that radiate from Elysium Mons and overlie and embay Albor Tholus and Hecates Tholus Formations. Type area: lat 32.5° N., long 214°.

Interpretation: Volcanic flows and related materials

AHat ALBOR THOLUS FORMATION Material forming Albor Tholus; hummocky texture, more subdued near vent. Type area: lat 18° N., long 210°.

Interpretation: Volcanic flows

Hhet HECATES THOLUS FORMATION Forms Hecates Tholus; hummocky surface cut by many narrow, sinuous channels. Type area: lat 33° N., long 209°.

Interpretation: Volcanic flows, some emplaced through lava channels

Hs SYRTIS MAJOR FORMATION: Plains-forming unit constituting Syrtis Major Planum. Characterized by many lobate deposits radiating generally from two irregular depressions (Nili Patera, centered at lat 9° N., long 293°, and Meroe Patera, centered at lat 7° N., long 291.5°); flow fronts and margins clearly recognizable; mare-type ridges trend north-northwest; many light and dark "wind" streaks on plains deposits. Type area: lat 11° N., long 295°. **Interpretation:** Lava flows erupted with low effective viscosity from central vents; rheological properties similar to those of basaltic magmas

HIGHLAND TERRAIN MATERIALS Rock units of moderate to high relief; dominate southern and near-equatorial parts of map area. Hellas assemblage Consists of units in and near Hellas Planitia.

Ah8 Knobby plains floor unit: Floor material characterized by low knobs a few kilometers across. Type locality: lat 35 S., long 295. **Interpretation:** Possibly remnants of mantle that has been differentially eroded; knobs may be small cinder cones

Ah7 Rugged floor unit: Forms undulating terrain of rugged relief on a kilometer scale in western Hellas Planitia; one occurrence mapped. Type area: lat 42° S., long 310°. **Interpretation:** Eroded mantle of possible eolian origin overlying ridged plains material (unit Hr)

Ah6 Reticulate floor unit: Plains material characterized by reticulate pattern of ridges; one occurrence mapped. Type area: lat 36° S., long 301.5°. **Interpretation:** Plains material whose high-standing remnants result from differential erosion

Ah5 Channeled plains rim unit: Plains material on east rim of Hellas basin characterized by narrow, sinuous channels and slight to moderate relief; includes widespread mesas having irregular margins and a few small knobs. Appears to fill some craters. Type area: lat 43° S., long 264°. **Interpretation:** Mantle of volcanic or eolian deposits eroded possibly by a combination of fluvial and eolian processes. Channels may be fluvial or volcanic

Ah4 Lineated floor unit: Smooth plains material characterized by straight and curvilinear lineaments; one occurrence mapped. Type area: lat 34° S., long 295°. **Interpretation:** Possible mantle modified by local tectonic processes

Hh3 Dissected floor unit: Smooth, rolling-plains material that has been deeply dissected to produce local rugged relief. Occurs in central part of Hellas Planitia. Type area: lat 40° S., long 289°. **Interpretation:** Sedimentary deposits modified by wind and minor fluvial activity; may include lava flows

Hh2 Ridged plains floor unit: Forms rolling smooth plains having sinuous to linear mare-type (wrinkle) ridges; occupies outermost Hellas Planitia as discontinuous concentric band. Type locality: lat 50° S., long 280°. **Interpretation:** Lava flows erupted with low effective viscosity; composition possibly basaltic

Nh1 Basin-rim unit: Material of the Hellas basin rim. Rugged, mountainous, heavily cratered, and modified by surficial processes, but intermontane patches have little relief. Type locality: lat 52° S., long 261°. **Interpretation:** Impact-generated unit of ancient Martian crust; consists of breccias and interbedded volcanic materials. Features normally associated with basins, such as radial troughs, not seen, probably covered by younger surficial deposits

Plateau and high-plains assemblage

Forms ancient highland terrain and local tracts of younger deposits.

OLDER CHANNEL MATERIAL AND CHAOTIC MATERIAL

- Hch Older channel material:** Occurs mainly along boundary of northern highlands of Deuteronilus Mensae but also in other highland locations, including margin of Hellas basin. Channels generally steep sided, smooth floored, and abruptly terminated on up-slope end. Type area: lat 25° N., long 60° (Scott and Tanaka, 1986). **Interpretation:** May be mixture of channel deposits and mass-wasted materials; channels may have formed by sapping
- Hcht Chaotic material:** Forms semicircular patches of closely spaced knobs of similar heights; mapped near west map border just south of lat 40° N. and near east border. Type area: lat 5° S., long 27° (Scott and Tanaka, 1986). **Interpretation:** Erosional remnants; not associated with channels within map area
- Nm MOUNTAINOUS MATERIAL:** Forms large, very rugged, isolated blocks. Scattered occurrences mostly around Hellas and Isidis basins. Equivalent in part to mountain material (mapped as "m") in south polar region (Tanaka and Scott, 1987). **Interpretation:** Mostly ancient crustal material uplifted during formation of impact basins

PLATEAU SEQUENCE: Forms rough, hilly, heavily cratered to relatively flat and smooth terrain covering most of highlands; occurs mostly in southern hemisphere.

- Hpl3 Smooth unit:** Forms flat, relatively featureless plains in southern highlands; locally embays other units of plateau sequence. Faults and flow fronts rare. Type area: lat 43° S., long 105° (Scott and Tanaka, 1986). **Interpretation:** Interbedded lava flows and sedimentary deposits of eolian or fluvial origin that bury most underlying rocks
- Hplm Mottled smooth plains unit:** Same as smooth unit but has mottled albedo patterns. Global occurrences only in southwestern part of map area. Type area: lat 38° S., long 358° **Interpretation:** Same as smooth unit except that wind-sorted sediments have produced mottled appearance
- Npl2 Subdued cratered unit:** Forms highland plains characterized by subdued and partly buried crater rims; fills some crater floors; flow fronts rare. Type area: lat 28° S., long 162° (Scott and Tanaka, 1986). **Interpretation:** Thin lava flows and sedimentary deposits that partly bury underlying rocks
- Npl1 Cratered unit:** Widespread in southern highlands; highly cratered, uneven surfaces of generally moderate, locally high relief; fractures and channels common. Type area: lat 45° S., long 148° (Scott and Tanaka, 1986). **Interpretation:** Materials formed during period of high impact flux; probably a mixture of volcanic materials, erosional products, and impact breccia
- Npld Dissected unit:** Similar in occurrence and appearance to cratered unit but more highly dissected by small channels, channel networks, and troughs. Gradational with cratered unit; placement of contact based on abundance of channels. Type area: lat 45° S., long 70° (Scott and Tanaka, 1986). **Interpretation:** Origin same as that of cratered unit but material more highly eroded by fluvial processes

- Nple Etched unit:** Similar to cratered unit but deeply furrowed by sinuous, intersecting, curved to flat-bottomed grooves, producing an etched or sculptured surface; commonly forms small mesas having irregular margins; craters and other depressions filled with smooth deposits. Occurs in several places on cratered plateaus, but is most extensive and well developed northwest of Syrtis Major Planum. Type area: lat 45° N., long 55° (Scott and Tanaka, 1986). **Interpretation:** Cratered unit that has been partly mantled by deposits of possible eolian origin and dissected by eolian erosion, decay and collapse of ground ice, and minor fluvial activity
- Nplr Ridged unit:** Resembles and is locally gradational with ridged plains material (unit Hr) where units adjoin, but ridges generally larger and farther apart, intervening areas rougher and more densely cratered. Type area: lat 15° S., long 163° (Scott and Tanaka, 1986). **Interpretation:** Flood-lava flows; ridges due to faulting, folding, or volcanic processes
- Nplh Hilly unit:** Rough, hilly, fractured material of moderately high relief. Type area: lat 12° S., long 174° (Scott and Tanaka, 1986). Forms complete or partial rims of Isidis and some other ancient basins. **Interpretation:** Ancient highland rocks and impact breccia generated during period of heavy bombardment
- HNu UNDIVIDED MATERIAL:** Forms closely spaced, conical hills a few kilometers across whose distribution indicates that they are remnants of numerous craters. Unit also forms rugged terrain on margins of cratered plateaus and isolated remnants (as west of Orcus Patera near east map border). Gradational with knobby plains material (unit Apk) where units adjoin, but hills are more closely spaced, larger, and occupy more than about 30 percent of area. No specific type area. **Interpretation:** Most hills are eroded remnants of ancient cratered terrain produced by mass-wasting processes, possibly as result of removal of ground ice; some hills may be erosional remnants of intrusive bodies (Greeley and Guest, 1978). Material may include some units of plateau sequence

HIGHLAND PATERAE

- AHt Tyrrhena Patera Formation:** Material forming Tyrrhena Patera; seen on high-resolution images to consist of several members (Greeley and Spudis, 1981), including a highly dissected basal member. Type locality: lat 22° S., long 254°. **Interpretation:** Volcanic materials erupted serially, including early-stage pyroclastic material and later lava flows
- AHa Apollinaris Patera Formation:** Material composing Apollinaris Patera. Consists of several members including deposits dissected by channels, some of which flowed over a basal scarp; forms a large fanlike feature on southeast flank. Type area: lat 9° S., long 186°. **Interpretation:** Material of multiple-stage eruptions forming shield volcano (Greeley and Spudis, 1981)
- AHh Hadriaca Patera Formation:** Material of Hadriaca Patera. Consists of smooth floor material in central depression, locally ridged along margin, surrounded by material dissected radially to depression. Type area: lat 31° S., long 268°. **Interpretation:** Material of central-vent volcano formed by multiple eruptions; possible pyroclastic deposits indicate explosive activity (Greeley and Spudis, 1981)
- Had Amphitrites Formation, dissected member:** Forms shieldlike deposit along north edges of Malea Planum (near south map border). Consists of deeply etched, ridged, lobate deposits and superposed crater material; sinuous furrows, ridges, and scarps trend toward Hellas Planitia. Type area: northern Malea Planum. **Interpretation:** Ridged plains material (unit Hr) modified

by fluvial channeling

MATERIALS OCCURRING THROUGHOUT MAP AREA

Apk KNOBBY PLAINS MATERIAL: Extensive in northern lowlands where it forms moderately to lightly cratered, generally smooth plains; several isolated occurrences in cratered highlands. Conical hills or knobs occur at irregular intervals; mare-type (wrinkle) ridges locally present. Where adjacent to undivided material (unit HNu), units are intergradational, but knobs in knobby plains unit are smaller and spaced farther apart. Type area: lat 22° N., long 263°.

Interpretation: Probably of diverse origins but appears to have formed mainly by erosion of older units. Knobs are probably erosional remnants but some may be volcanic. Intervening plains may be erosional surfaces or may consist of eolian, mass-wasted, or volcanic materials

Hr RIDGED PLAINS MATERIAL: Characterized by broad planar surfaces, rare lobate deposits, and long, parallel, linear to sinuous mare-type (wrinkle) ridges about 30 to 70 km apart. Forms plains within and outside craters throughout plateau area and lowland plains north of Orcus Patera (near east map border). Locally gradational with ridged plateau material (unit Nplr) where units adjoin. Type area: Lunae Planum, lat 10° N., long 65° (Scott and Tanaka, 1986).

Interpretation: Extensive lava flows erupted with low effective viscosity from many sources at high rates; ridges either volcanic constructs or compressional features

c, s IMPACT-CRATER MATERIALS: Yellow indicates materials of superposed craters greater than about 100 km across; brown indicates materials of partly buried craters greater than about 150 km across. May include rim crest (hachured), central ring (inner circular feature, also hachured), and central peak. Hachures also denote impact-basin rims. Symbol "c" denotes crater-rim and ejecta material. Symbol "s" and orange color denote smooth floor material; within mapped crater material, only patches larger than 30 km across are shown; elsewhere, only patches larger than about 80 km across are shown. Linear dot pattern denotes secondary craters outside crater aprons. **Interpretation:** Units resulting from impact cratering, but smooth-floor material may be of volcanic, eolian, or fluvial origin

LOWLAND TERRAIN MATERIALS

Consist of all plains-forming units between the highland-lowland boundary scarp and the north edge of the map area, exclusive of materials of the western volcanic assemblage on the Tharsis swell.

Northern plains assemblage

Materials deposited in widespread sheets on northern plains. Within each formation, members mapped at places on basis of crater density; these contacts are approximately located. Assemblage postdates highland-lowland boundary scarp (Scott, 1979).

ARCADIA FORMATION: Forms low-lying plains in Arcadia, Amazonis, and Acidalia Planitiae. Embays highland margins and partly buries outflow channels of Kasei, Shalbatana, Simud, Tiu, and Ares Valles. Members distinguished on basis of morphology, albedo, and crater density; common boundaries of older members mapped arbitrarily at places. Flows with lobate margins and small hills with summit craters visible in many places. High-resolution pictures show that sources of some flows

are small cratered cones. **Interpretation:** Mostly lava flows and small volcanoes

- Aa5 Member 5:** Relatively small areal extent. Dark, fresh-appearing flows; few superposed impact craters. Type area: lat 47° N., long 30°
- Aa4 Member 4:** In Arcadia Planitia underlies member 5 and has similar appearance; one other occurrence in channel system of Chryse Planitia. Type area: lat 45° N., long 175°
- Aa3 Member 3:** Forms smooth plains west of Olympus Mons aureoles; embays both the aureoles and fractured terra of Acheron Fossae. Flow fronts visible in places. Type area: lat 15° N., long 155°
- Aa2 Member 2:** Underlies members 3, 4, and 5 in Arcadia Planitia. Includes many small (<10-km-diameter) structures resembling volcanoes and cinder cones. Curved concentric ridges visible on surfaces of flows. Type area: lat 45° N., long 155°
- Aa1 Member 1:** Widespread in Chryse and Amazonis Planitiae. Mare-type (wrinkle) ridges common. Type area: lat 30° N., long 40°

MEDUSAE FOSSAE FORMATION- Consists of extensive, relatively flat sheets, generally smooth to grooved and gently undulating; deposits appear to vary from soft to indurated; albedo moderate. Occurs near equator in western part of map area. Total thickness may exceed 3 km

Amu Upper member: Discontinuous but widespread deposits extend from south of Olympus Mons westward across Amazonis Sulci to map boundary. Smooth, flat to rolling, light-colored surfaces; sculptured into ridges and grooves in places (as in Medusae Fossae); broadly curved margins, locally serrated. Type area: lat 0° N., long 160°. **Interpretation:** Nonwelded ash-flow or ash-fall tuff or thick accumulation of eolian debris; wind eroded, particularly along margins

Amm Middle member: Similar to upper member but in places (as at Memnonia Sulci) surface appears rougher, more deeply eroded; cut by scarps of Gordii Dorsum and transected in type area by intersecting joint sets. Type area: lat 10° N., long 160°. **Interpretation:** Welded and nonwelded pyroclastic rocks or layers of relatively soft to indurated eolian deposits

Aml Lower member: Two small occurrences in western map area. Surfaces smooth to rough and highly eroded, darker than those of other members. Type area: lat 0° N., long 174°. **Interpretation:** Lava flows interbedded with pyroclastic rocks or eolian deposits

VASTITAS BOREALIS FORMATION Subpolar plains deposits of northern lowlands. Its four members distinguished on basis of morphology or albedo contrast; placement of contacts locally arbitrary

Hvm Mottled member: Major occurrence north of map boundary (Tanaka and Scott, unpub. data, 1985); extends as far south as topographic reentrants between Acidalia and Chryse Planitiae where appears windswept. Crater-ejecta blankets have higher albedo than adjacent terrain; lobate flow fronts visible; some small hills present. Type area: lat 55° N., long 40°. **Interpretation:** Possibly consists of lava flows erupted from fissures and small volcanoes or of alluvial and eolian deposits. Mottled appearance due to contrast between generally low albedo of plains and brightness of small hills and impact-crater aprons

Hvg Grooved member: Similar to mottled member in Acidalia Planitia but marked by curvilinear and polygonal patterns of grooves and troughs; closed polygons as wide as 20 km. Type area: lat 45° N., long 15°. **Interpretation:** Material same as mottled member; patterns may be due to compaction or to tectonic or ground-ice phenomena

Hvr Ridged member: Three small occurrences of mottled plains characterized by concentric pattern of low, narrow ridges about 1 to 2 km wide. Type area: lat 38° N., long 33°; other two outcrops near lat 54° N., long 176°. **Interpretation:** Material same as mottled member; origin of ridges unknown but they may be periglacial structures or channel-meander features accentuated by differential erosion

Hvk Knobby member: Similar in appearance to mottled member but generally has higher albedo and abundant small, dark, knoblike hills, some with summit craters. Type area: lat 55° N., long 5°. **Interpretation:** Material same as mottled member; hills may be small volcanoes or remnants of highland terrain or crater rims

Channel-system materials

Deposited in outflow channels and on flood plains; exhibit both depositional and erosional features. Interpretation: Channel and flood-plain materials of alluvial origin; some surfaces sculptured by flood waters. Chaotic material formed by disruption of terrain by ground-water release.

Ach, Achp YOUNGER CHANNEL AND FLOOD-PLAIN MATERIALS: Along western margin of map area, form plain as wide as 200 km marked by dark, sinuous, intertwining channels with bars and islands; fill small channels in Arcadia Planitia, along north edge of Tempe Fossae, and in Ophir and Candor Chasmata. Crater counts and superposition relations indicate Amazonian age. Type areas: lat 15° N., long 177° (unit Ach) and lat 22° N., long 171° (unit Achp)

Hch, Hchp, Hcht OLDER CHANNEL, FLOOD-PLAIN, AND CHAOTIC MATERIALS: Mainly between Valles Marineris and Chryse Planitia, also in other highland locations. Channel deposits longitudinally striated; teardrop-shaped channel bars large and well developed. Flood-plain material occurs adjacent to channels and in lowland plains below channel mouths, smooth and featureless. Chaotic material occurs at source areas and along margins of channels and within some chasmata and craters; generally a mosaic of highland blocks in depressions. Type areas: lat 25° N., long 60° (unit Hch); lat 27° N., long 53° (unit Hchp); lat 5° S., long 27° (unit Hcht)

HIGHLAND TERRAIN MATERIALS

Rock and rock-tectonic units of moderate to high relief; dominate southern and near-equatorial parts of map area. Volcanic mountains and associated lava flows of Tharsis region, although not typical of highland terrain, are included in this physiographic classification because they are superposed on highland terrain or form high plains and locally rugged topographic features.

Western volcanic assemblage

Volcanoes and lava flows in Tharsis region of Mars (Schaber and others, 1978; Scott and others, 1981).

THARSIS MONTES FORMATION: Includes large volcanic shields and associated lava flows of Arsia Mons, Pavonis Mons, and Ascraeus Mons; lava flows similar in morphology to terrestrial basalts (Schaber and others, 1978)

At6 Member 6: Fresh-appearing lava flows form smooth, fan-shaped arrays on flanks of Arsia, Pavonis, and Ascraeus Montes, flows probably originate from fissures along major structural trends. Flanks of these volcanoes exhibit grabens, some concentric. Member also includes most recent fill within central calderas of Tharsis Montes. Type area: lat 5° S., long 117°

At5 Member 5: Widespread around Tharsis Montes volcanoes. Overlies parts of channel and flood-plain deposits (units Hch, Hchp) of Kasei Valles; contact with upper member (unit Hsu) of Syria Planum Formation northwest of Echus Chasma poorly resolved. At places forms elongate, light-colored flow lobes with abundant dark wind streaks. Cut by few faults. Type area: lat 20° S., long 120°

At4 Member 4: Exposed mostly northeast and southwest of member 5. Consists of overlapping light flows with dark wind streaks similar to those of member 5; flows elongate on steep upper slopes, broad on gentler lower slopes. High-resolution images show pressure ridges concentric with lobate flow fronts; minor faulting. Type area: lat 15° S., long 135°

AHt3 Member 3: Makes up central shields of Arsia, Pavonis, and Ascraeus Montes and embays highland terrain west of Arsia Mons and along northwest side of Claritas Fossae, where light and dark flows common. Fewer lobate fronts, pressure ridges, and dark streaks but more faults than in members 4 and 5. Type area: lat 27° S., long 127°

Ht2 Member 2: Occurs in southern and northeastern parts of Tharsis region; embays highland terrain of Tempe Fossae. Composed of relatively smooth flows having broad frontal lobes; fractures and faults common in places. Type area: lat 33° S., long 135°

Ht1 Member 1: Scattered outcrops in southern Tharsis region. Generally forms rough, hummocky surface; mare-type (wrinkle) ridges in places; faults and fractures common locally. Type area: lat 30° S., long 120°

OLYMPUS MONS FORMATION: Includes young lava flows extruded from fissures in plains east of Olympus Mons, young shield lavas of the volcano, and aureole deposits surrounding the volcano. Interpretation of aureoles: Formed by gravity spreading of materials forming a larger, earlier Olympus Mons; alternatively, could be ash or lava flows (see text)

Aop Plains member: Embays basal scarp of Olympus Mons and overlaps shield member. Consists of many overlapping smooth lava flows ranging in shape from narrow tongues to broad lobes; flows appear to be extruded from faults and fissures below scarp on southeast side of Olympus Mons. Type area: lat 20° N., long 125°

Aos Shield member: Lava flows form complex, finely textured, interfingering tongues and lobes. Channels and levees extend down flanks of Olympus Mons and across prominent basal scarp on north, east, and south sides, collapse pits common. Type area: lat 15° N., long 135°

Aoa4 Aureole member 4: Uppermost of a series of aureole units around Olympus Mons that formed prior to or contemporaneously with the volcano's basal scarp. Forms broad, semicircular, flat lobes; corrugated, cut by numerous faults that formed scarps and deep troughs and grabens.

Type area: lat 25° N., long 145°

Aoa3 Aureole member 3: Forms two lobes; similar to but underlying member 4. Type area: lat 28° N., long 134°

Aoa2 Aureole member 2: Forms three lobes; similar to members 3 and 4; underlies member 3 in relatively small area on southwest side of Olympus Mons; on east side occurs as islands surrounded by plains member. Type area: lat 14° N., long 143°

Aoa1 Aureole member 1: Forms widespread basal aureole; overlaps younger and older fractured materials (units Hf and Nf). Resembles younger aureole members but smoother and more degraded by wind. Type area: lat 15° N., long 147°

AHcf CERAUNIUS FOSSAE FORMATION: A series of overlapping flows whose surfaces are relatively smooth and even toned to mottled and streaked; trends northeast across older fractured material (unit Nf) in Ceraunius Fossae; channels with levees occur in places. Type area: lat 23° N., long 115°. **Interpretation:** Lava flows, most of which originated from fissures

SYRIA PLANUM FORMATION: Volcanic flows of intermediate age that originated from crestal area and flanks of topographic high in northern Syria Planum and Noctis Labyrinthus

Hsu Upper member: Partly encircles crest of topographic high. Consists of both long narrow lava flows and sheet flows that have prominent lobes mottled light and dark; pit craters common. Relatively smooth around Valles Marineris. Covers some fault systems of Claritas Fossae but cut by few others in Noctis Labyrinthus. Flows probably extruded from calderas near summit of Syria Planum and from fissures; gradational with lower member. Boundary with ridged plains material (unit Hr) not clearly defined, placed where member appears to overlap ridges. Type area: lat 15° S., long 100°

Hsl Lower member: Similar to upper member but more highly cratered and faulted. Type area: lat 25° S., long 90°

ALBA PATERA FORMATION: Forms low shield and extensive lava flows of Alba Patera volcano

Aau Upper member: Covers large area within and around central calderas; lava flows completely or partly bury most ring and radial structures; channels with levees common along crests of flows. Type area: lat 40° N., long 110°

Aam Middle member: Encircles crestal region and upper member; occurs as low radial ridges with summit channels and as long narrow tongues with leveed channels. Highly faulted but buries many grabens in older fractured material (unit Nf). Type area: lat 40° N., long 118°

Hal Lower member: Covers broad area around north and west flanks of Alba Patera. Flow fronts less distinct than those of younger members. Extends into plains region; appears to be overlapped in places by lowermost member (unit Aa1) of Arcadia Formation but most of boundary indistinct. Type area: lat 35° N., long 125°

Plateau and high-plains assemblage

Forms ancient highland terrain and local tracts of younger deposits.

SURFICIAL DEPOSITS

Slide material of three types

- As** (1) In Valles Marineris and other chasmata as rotational slide deposits from canyon walls, surfaces hummocky near crown scarp; distal parts commonly lobate, longitudinally striated, with long runout. Type area: lat 9° S., long 72°. Interpretation: Gas- or water-lubricated slides and debris flows
- (2) Mostly on northwest flanks of Olympus Mons and largest volcanoes of Tharsis Montes as fanlike corrugated sheets as wide as 600 km that appear to override topographic obstacles without deflection of internal structure; source areas hummocky, contain small hills and circular depressions. Type area: lat 5° S., long 125°. Interpretation: Volcanic-debris avalanches resulting from either slope failure or explosive volcanism; alternatively, may be recessional moraines of former local ice caps
- (3) Along scarps of Charitum Montes and Mareotis Fossae as smooth, sloping aprons with steep, high edges. No specific type area. Interpretation: Debris aprons produced by mass wasting and slow, glacierlike flow of ice-rich plateau material
- Ae** **Eolian deposits:** Form broad level plains chiefly on aureole deposits of Olympus Mons. Surfaces locally appear rough, deeply etched, and striated in directions of prevailing winds. Type area: lat 15° N., long 145°

VALLES MARINERIS INTERIOR DEPOSITS □ Materials within Valles Marineris and associated canyons, excluding walls and mapped landslides and channel materials

- Avf** **Floor material:** Occurs along canyon floors as smooth to hummocky and rugged material of low relief. No specific type area. **Interpretation:** Mixture of landslides and debris flows from canyon walls, eolian material, volcanic deposits, and channel and possibly lacustrine deposits
- Hvl** **Layered material:** Thinly bedded dark and light materials visible in high-resolution pictures on floors of several canyons. Forms platforms and hills of moderate to high relief. Type area: lat 7° S., long 48°. **Interpretation:** Volcanic or lacustrine material or both, deposited during intermediate to late stages of canyon development

PLATEAU SEQUENCE: Forms rough, hilly, heavily cratered to relatively flat and smooth terrain covering most of highlands, which are dominant in southern hemisphere. Several units represent transitional stages modified by erosional or depositional processes

- Hpl3** **Smooth unit:** Forms large areas of flat, relatively featureless plains in southern highlands; locally embays other units of plateau sequence. Faults and flow fronts rare. Type area: lat 43° S., long 105°. **Interpretation:** Thick interbedded lava flows and eolian deposits that bury most of underlying rocks
- Npl2** **Subdued cratered unit:** Forms plains (mostly in highlands) marked by subdued and partly buried old crater rims. Flow fronts rare. Type area: lat 28° S., long 162°. **Interpretation:** Thin interbedded lava flows and eolian deposits that partly bury underlying rocks
- Npl1** **Cratered unit:** Most widespread unit in southern highlands; locally extensive in northern plains. Highly cratered, uneven surface of moderate relief; fractures, faults, and small channels common. Type area: lat 45° S., long 148°. **Interpretation:** Materials formed during period of

high impact flux; probably a mixture of lava flows, pyroclastic material, and impact breccia

Npld Dissected unit: Similar in occurrence and appearance to cratered unit but more highly dissected by small channels and troughs. Type area: lat 45° S., long 70°. **Interpretation:** Origin same as that of cratered unit but more eroded by fluvial processes

Nple Etched unit: Similar to cratered unit but deeply furrowed by sinuous, intersecting, curved to flat-bottomed grooves that produce an etched or sculptured surface. Type area: lat 45° N., long 55°. **Interpretation:** Cratered unit that has been degraded by wind erosion, decay and collapse of ground ice, and minor fluvial processes

Nplr Ridged unit: Resembles ridged plains material (unit Hr) where units adjoin, but ridges generally larger and farther apart, intervening areas rougher and more densely cratered. Type area: lat 15° S., long 163°. **Interpretation:** Most ridges due to normal faulting but others may be volcanic constructs or compressional features

Nplh Hilly unit: Rough, hilly material that resembles in part basement complex (unit Nb) and older fractured material (unit Nf), but relief is gentler and faulting less intense. Type areas: lat 12° S., long 174° and Nereidum and Charitum Montes surrounding Argyre Planitia. **Interpretation:** Ancient highland volcanic rocks and impact breccia uplifted by tectonism and impact-basin formation during period of heavy bombardment

Hr RIDGED PLAINS MATERIAL: Major occurrences cover an area of about 4,000,000 km² extending from Solis Planum to Tempe Fossae. Characterized by broad planar surfaces with flow lobes visible in places and long, parallel, linear to sinuous mare-type (wrinkle) ridges; ridges about 30 to 70 km apart. Type area: Lunae Planum, lat 10° N., long 65°. **Interpretation:** Extensive flows of low-viscosity lava erupted from many sources at high rates, ridges either volcanic constructs or compressional features (see text)

TEMPE TERRA FORMATION: Interpreted to consist of intermediate-age lava flows extruded from small shield volcanoes, fissures, and depressions on Tempe Terra plateau. All members exhibit lobate scarps that may be edges of flows

Htu Upper member: Smooth, light-colored, partly mottled material that embays hilly, mountainous, and fractured terrain of highlands; small (<10-km-diameter) shield volcanoes visible in high-resolution pictures; few faults and fractures; embayed by a lower member (unit Ht2) of Tharsis Montes Formation and by lower member (unit Hal) of Alba Patera Formation. Type area: lat 36° N., long 86°

Htm Middle member: Similar to upper member but faults, fractures, and collapse depressions common. Type area: lat 42° N., long 80°

Htl Lower member: Smooth to rough, uneven surfaces; small faults and collapse depressions common. Overlaps hilly and cratered units (units Nplh, Npl1) of plateau sequence but is embayed by upper and middle members of Tempe Terra Formation. Type area: lat 39° N., long 84°

HIGHLY DEFORMED TERRAIN MATERIALS: The origin and composition of these rock units

are only surmised because multiple sets of fractures and grabens have obscured original characteristics. The units are interpreted to consist of impact breccia interlayered with volcanic flows and to intergrade locally

Hf Younger fractured material: Occurs mostly around Valles Marineris and Syria and Sinai Plana and northwest of Pavonis Mons. Forms relatively smooth, raised surfaces of moderate relief with fractures, grabens, and collapse depressions. Overlies other highly deformed terrain materials but is embayed and partly covered by Syria Planum Formation and other younger rock units. Type area: lat 5°S., long 103°

Nf Older fractured material: similar to fractured material but widespread, has greater relief, is more highly deformed, and faults are more complexly oriented; impact-crater outlines largely destroyed. Type area: lat 20° S., long 109°

Nb Basement complex: Undifferentiated material characterized by highly complicated structure and prominent relief. Most common in Claritas and Mareotis Fossae areas. Type area: lat 28° S., long 100°

HNu UNDIVIDED MATERIAL: Forms hills and small knobs adjacent to highland-lowland boundary scarp that extend almost to north map border. Also forms walls and interior mountains in Valles Marineris and associated canyons and channels, as well as hummocky terrain and scarps along edges of Chryse and Acidalia Planitiae. No specific type area. **Interpretation:** Erosional remnants and exposures of plateau sequence, highly deformed terrain materials, ancient crater rims, and some other materials that are older than surrounding rock units

NORTH POLAR REGION

Northern plains assemblage

Materials deposited in widespread sheets on northern plains. Boundaries between rock units commonly not well defined, in places indicated by dashed contact.

ARCADIA FORMATION: Smooth, sparsely cratered; lobate fronts visible in places. Embays all neighboring units. (Members 2, 4, and 5 (units Aa2, Aa4, and Aa5) mapped to south, not present in map area.) Interpretation: Lava flows and sediments from local sources

Aa3 Member 3: Forms isolated patches along edge of map area between long 170° and 180°

Aa1 Member 1: Forms low-lying plains surrounding Alba and Tantalus Fossae

Aps SMOOTH PLAINS MATERIAL: Forms two areas of smooth, sparsely cratered plains north of crater Lyot near edge of map area (long 315° to 340°) and near knobby, undivided material at long 193°. **Interpretation:** Probably of diverse origin, but may primarily consist of eolian deposits

VASTITAS BOREALIS FORMATION: Subpolar plains deposits. Type areas designated in western equatorial region (Scott and Tanaka, 1986)

Hvm Mottled member: Characterized by high-albedo crater deposits superposed on low-albedo, smooth-plains deposits; occurs along more than half of edge of map area; gradational with other

members, particularly with knobby member. **Interpretation:** Lava flows, possibly erupted from fissures and small volcanoes, or alluvial or eolian deposits. Mottled appearance due either to relatively fresh, light-colored material exposed during impact-crater excavation or to high-albedo eolian debris trapped within crater ejecta

Hvg Grooved member: Marked by grooves forming polygonal pattern; polygons commonly 5 to 20 km across; small patch at lat 80° N., long 60° in mouth of Chasma Boreale; eroded on south side. **Interpretation:** Degraded lava flows or sediments; grooves may be lava-cooling, periglacial, tectonic, dessication, or compaction phenomena

Hvr Ridged member: Scattered occurrences mostly in western longitudes; gradational with knobby, mottled, and smooth members; in places embayed by Arcadia Formation. Ridges about 1 to 2 km wide and several to tens of kilometers long commonly form polygons 5 to 20 km across; ridge patterns in some southern outcrops are arcuate or concentric, as at lat 56° N., long 173°. **Interpretation:** Degraded lava flows or sediments; ridge pattern may be formed by intrusion of viscous lava in grooves of grooved member or by remnants of dikes on a stripped surface; concentric ridges may result from scarp retreat caused by periglacial or erosional processes

Hvk Knobby member: Characterized by abundant, kilometer-size, dark, knoblike hills spaced generally a few kilometers apart and commonly grouped into linear chains. Occurs in broad circumpolar belt; interknob areas gradational with mottled and ridged members. **Interpretation:** Knobs probably small volcanoes and highly degraded remnants of highland material (unit HNu), crater rims, and older plains material. Interknob plains probably degraded lava flows or sediments

Channel-system and eolian materials

Depositional and erosional units within channels and plains, and dune deposits.

Ach YOUNGER CHANNEL MATERIAL: Smooth, sparsely cratered material within part of channel along edge of map area at long 58°; channel originated from Tempe Fossae region to south (Scott and Tanaka, 1986). Superposed on flood-plain material and mottled and knobby members of Vastitas Borealis Formation. **Interpretation:** Recent fluvial material

Adc CRESCENTIC DUNE MATERIAL: Forms individual and linked crescentic dunes; individual dunes as large as several kilometers across. Occurs along most of edge of Planum Boreum. **Interpretation:** Active barchan dunes made up of sand-size particles consisting of mineral grains or dust and ice aggregates. Occurrence indicates areas of moderate sand accumulation or erosion

Adl LINEAR DUNE MATERIAL: Forms linear, ripplelike patterns of dunes in north polar erg in Arion Planitia and near mouth of Chasma Boreum; wavelength of ripples about 1 to 2 km. **Interpretation:** Forms relatively stable, mature dune field; dune orientations controlled by oscillating wind directions. Presence indicates regime of large sand accumulations in topographic lows

Am MANTLE MATERIAL: Smooth to hummocky deposit, as much as several hundred meters thick; surrounds most of Planum Boreale; extent of unit may vary seasonally. Mapped only north of lat 66° N., where thick enough to obscure features characteristic of members of Vastitas Borealis Formation. **Interpretation:** Eolian deposits derived from seasonal frost and dust accumulation and perhaps erosion of polar layered deposits, polar dunes, and subpolar

plains materials

Hchp FLOOD-PLAIN MATERIAL: Smooth, moderately cratered material with longitudinal albedo streaks; occurs at edge of map area at long 60°, adjacent to younger channel material; forms north tip of flood-plain deposits along west edge of Acidalia Planitia; embayed by member 1 of Arcadia Formation. **Interpretation:** Deposits from fluvial channels south of map area (Scott and Tanaka, 1986)

Western volcanic assemblage

ALBA PATERA FORMATION

Hal Lower member: Forms gently sloping plateau that emerges from Vastitas Borealis. Marked by degraded lobate flow fronts and small impact craters; displays grabens a few kilometers across and tens to hundreds of kilometers long; embayed by member 1 of Arcadia Formation. To south, unit covers broad region containing most of Alba and Tantalus Fossae; north edge of region extends into map area. Previously mapped as cratered and fractured plains material (Dial, 1984). **Interpretation:** Older, highly degraded lava flows originating from Alba Patera and surrounding fractures

Plateau and high-plains assemblage

Consists of ancient highland terrain and local tracts of younger deposits that stand relatively high.

POLAR DEPOSITS

Api Polar ice deposits: Residual polar cap of high-albedo material imaged in late spring and summer (Ls=92 to 154), 1977; occurs on high surfaces of Planum Boreum, in irregular patches north of lat 70° N. between longs 10° and 270°, and on crater floors. **Interpretation:** Photometry and infrared thermal mapping indicate water-ice and dust composition (Kieffer and others, 1976). Covered by CO₂ frost that extends continuously as far south as lat 65°N. during winter. Some outlier deposits may be wind-streaked material composed mainly of ice or frost

Apl Polar layered deposits: Form Planum Boreum and nearby mesas south of Chasma Boreale; smooth, uncratered; moderate albedo; Planum Boreum cut by troughs in swirl pattern; troughs expose alternating light and dark layers tens of meters thick, some unconformable; total thickness estimated at 4 to 6 km (Dzurisin and Blasius, 1975) or 1 to 2 km (Wu and others, in press). Composite age of deposits uncertain. **Interpretation:** Deposits of mixed ice and dust. Light and dark layering caused by variation in dust-to-ice ratio; reflects long-term climate changes. Unconformities attributed to alternating periods of erosion and deposition that vary from place to place or to glacial surges

Hnu UNDIVIDED MATERIAL: Forms high-standing hills and irregular mesas several to more than 10 km across; largest exposures make up Scandia Colles and rims of large craters nearby. Resembles knobby member of Vastitas Borealis Formation but hills generally larger and more closely spaced. **Interpretation:** Remnants of ancient highland material projecting above plains; heavily eroded by mass wasting

SOUTH POLAR REGION

Channel-system and eolian materials

- Am MANTLE MATERIAL:** Thin, smooth, sparsely cratered material in pits of Angusti and Sisyphi Cavi. **Interpretation:** Cover of dust deposited by seasonal dust storms and perhaps material eroded from pit walls by mass wasting
- Ad DUNES AND DUNE-CAPPED MATERIAL:** Thick, circular, steep-edged deposits covered by complex linear dunes and dune chains; dune ridges concentric to edges of deposits. Unit commonly occurs on north sides of crater floors and in low areas near edge of polar layered deposits on Terrae Sirenum and Cimmeria. **Interpretation:** Locations and complex shapes suggest dunes composed of ice and fine material derived from polar layered deposits; underlying deposits may consist of polar layered material; deposited in areas of low wind strength
- Hch OLDER CHANNEL MATERIAL:** Smooth, longitudinally grooved deposits within two long sinuous channels: one channel winds through Charitum Montes and is overlain by ridged plains material in Argyre Planitia; other channel runs along border of Malea Planum and Promethei Terra. **Interpretation:** Channels cut by flowing water or ground-ice sapping; deposits may include alluvial material, glacial till, or debris flows

Plateau and high-plains assemblage

Dominates map area; consists of rock units having moderate to high relief. Includes rugged, heavily cratered materials, also volcanic and polar deposits forming high plains.

- As SLIDE MATERIAL:** Lobate, high-albedo, striated, and uncratered slope deposits extending 5 to 10 km from massifs in southern Argyre Planitia. **Interpretation:** Aprons of ice and debris eroded from highland terrain; emplaced by gelifluction, creep, or glacial flow

POLAR DEPOSITS

- Api Polar ice deposits:** Form residual high-albedo feature of Martian southern summer ($L_s=348$), 1977; offset from axial-pole position about 200 km south at long 45° surface striated. **Interpretation:** Water-ice cap, usually covered by CO_2 because of colder temperature relative to north pole; striations due to relatively strong winds
- Apl Polar layered deposits:** Smooth, sparsely cratered, moderate-albedo material that forms Planum Australe; in places characterized by alternating light and dark layers tens of meters thick; complete sequence as much as 3 km thick. Cut by curvilinear to irregular scarps and troughs, which include Chasma Australe; underlying terrain at base of troughs unscarred. **Interpretation:** Ice and dust deposits; albedo layering related to ice content that, in turn, depends on climate. Some scarps and troughs carved by prevailing wind patterns; others possibly formed by glacial surge. Lack of etching in underlying terrain indicates relative softness of layered material

PLATEAU SEQUENCE: Forms rough, heavily cratered to smooth, relatively flat terrain throughout region. Subdivision of units based on relative age and type and degree of surface modification

- Hpl3 Smooth unit:** On Argyre Planitia and within intercrater areas on plateau-sequence material, forms flat, moderately cratered, smooth plains; embays all adjacent units; flow fronts and wrinkle ridges rare. On Malea Planum, forms irregular surfaces superposed on ridged plains material; eroded into knobs along edges; preserved in broad low areas or below superposed crater ejecta (as at lat 58° S., long 327°). **Interpretation:** Lava flows from local sources or eolian deposits, except perhaps on Malea Planum, where may be remnants of ice-rich mantle material
- Npl2 Subdued cratered unit:** Forms moderately rough, uneven plains in broad, low-lying intercrater and intracrater regions; high density of craters 1 to 10 km across; large subdued crater rims common; small wrinkle ridges in places; flow fronts rare. **Interpretation:** Thin mantle of interbedded lava flows and eolian deposits
- Npl1 Cratered unit:** Most widespread highland rock unit; high density of craters >10 km in diameter, rugged surface, moderate relief; sparse distribution of channels, fractures, and small ridges. **Interpretation:** Materials formed during period of high impact flux; probably a mixture of lava flows, pyroclastic material, and impact breccia
- Npld Dissected unit:** Similar in occurrence and appearance to cratered unit, but highly dissected by networks of small channels. **Interpretation:** Origin same as cratered unit; channels produced by rain-water runoff or ground-ice sapping
- Nple Etched unit:** Similar to cratered unit, but marked by flat-bottomed troughs and knobs several kilometers in size or larger; occurs in patches in Noachis Terra and Malea Planum
Interpretation: Cratered unit degraded by wind erosion and removal of ground ice, perhaps induced by local volcanic heating
- Nplr Ridged unit:** Forms rough, moderately to heavily cratered terrain containing wide, long ridges and scarps; most occurrences form wide swath along south edge of Malea Planum and Promethei Terra. **Interpretation:** Probably interbedded volcanic rocks and impact breccia; ridges formed by volcanism or folding and normal faulting, perhaps along preexisting structures related to Hellas impact basin and other ancient crustal structures
- Nplh Hilly unit:** Hilly facies of cratered unit, but has higher relief due to pronounced crater rims, massifs, and fault scarps; forms rim of Argyre impact basin (Charitum Montes) and other hilly terrain; underlies cratered unit. **Interpretation:** Mostly rim material of Argyre impact basin, probably uplifted crustal material and impact breccia; other occurrences may be volcanic, tectonic, or impact-related mountains
- Hr RIDGED PLAINS MATERIAL:** Forms broad, planar, moderately cratered surfaces marked by long, linear to sinuous ridges resembling those on lunar maria; ridges commonly several kilometers wide and tens of kilometers long. Covers most of Malea Planum and many intercrater regions, particularly in Terrae Sirenum and Cimmeria; embays all adjacent units except for some young smooth materials. **Interpretation:** Extensive flows of low-viscosity lava erupted at high rates from local sources, including fissures and Amphitrites, and Peneus Paterae

AMPHITRITES FORMATION

- Hap Patera member:** On Malea Planum forms Amphitrites and Peneus Paterae, which are

characterized by circular patterns of both wrinkle ridges and faults. Type area: Amphitrites Patera. **Interpretation:** Material of volcanic centers and associated ring faults from which ridged plains material was extruded

Had Dissected member: Ridged plains material deeply furrowed by sinuous channels and gullies that trend downslope toward Hellas Planitia (centered at lat 45° S., long 290°); many superposed and embayed impact craters. Forms plains of northern Malea Planum; gradational with ridged plains material; embays rim material of Hellas Basin. Type area: northern Malea Planum. **Interpretation:** Relatively soft ridged plains material or mantle modified by channeling

DORSA ARGENTEA FORMATION: Forms polar plains near Angusti and Sisyphi Cavi and Promethei Rupes; embays older highland rocks and ridged plains material; underlies polar layered deposits; middle Hesperian age indicated by crater counts

Hdu Upper member: Deposits generally broad and smooth, lightly pitted in places, except at Dorsa Argentea, where deposits have sinuous, braided, kilometer-wide ridges as long as 150 km. Edges locally distinct and lobate; embays surrounding cratered terrain. Type area: Dorsa Argentea. **Interpretation:** Lava flows originating from unrecognized fissure vents in vicinity of crater Schmidt, Sisyphi Montes, and other local sources; ridges may be unusual lava-flow features or eskers

Hdl Lower member: Similar to upper member but more degraded; forms mostly smooth pitted plains around cavi. Type area: plains surrounding Angusti and Sisyphi Cavi. **Interpretation:** Eolian mantle or lava flows originating from local fractures and possible volcano at Sisyphi Cavi. Highly degraded by cavi formation, perhaps facilitated by removal of underlying ground ice

HELLAS ASSEMBLAGE □ Map units associated with impact and fill of Hellas impact basin (Greeley and Guest, 1987). Only one of these units is exposed in south polar map area

Nh1 Basin-rim unit □ Rugged to mountainous, heavily cratered and resurfaced material of Hellas Basin rim east of Malea Planum. **Interpretation:** Impact breccia and interbedded volcanic material of ancient crust; impact structures such as radial troughs not seen, probably degraded and buried by surficial deposits

Nhu UNDIVIDED MATERIAL: Rough, massive deposits exposed in walls and floors of large, irregular pits as much as a kilometer deep at Angusti and Sisyphi Cavi; forms closely spaced, rounded hills a few kilometers across; grades into etched unit of plateau sequence. Most of unit underlies Dorsa Argentea Formation. **Interpretation:** Plateau sequence and basement rocks; pitting and degradation caused by removal of ground ice, mass wasting, and eolian exhumation of poorly consolidated material

CONTACT Dashed where approximately located or gradational; queried where doubtful

FAULT OR GRABEN: Bar and ball on downthrown side of fault

RIDGE Symbol on ridge crest

SCARP Line marks top of slope; barb points downslope

NARROW CHANNEL

CALDERA

DOME Low, moderately sloping; origin and age uncertain

MOUNTAIN High, rugged; origin and age uncertain

VOLCANO Queried if origin conjectural; age uncertain

IMPACT CRATER MATERIALS Yellow if superposed, brown if partly buried. May include rim crest (hachured), central peak, smooth floor (symbol s). Symbol c denotes crater-rim and ejecta materials. Materials of impact craters less than about 100 km across not mapped. Ejecta from crater Lyot, centered at lat 50° N., long 331°, shown by symbol el.

APPENDIX D – Graphs of Mars data

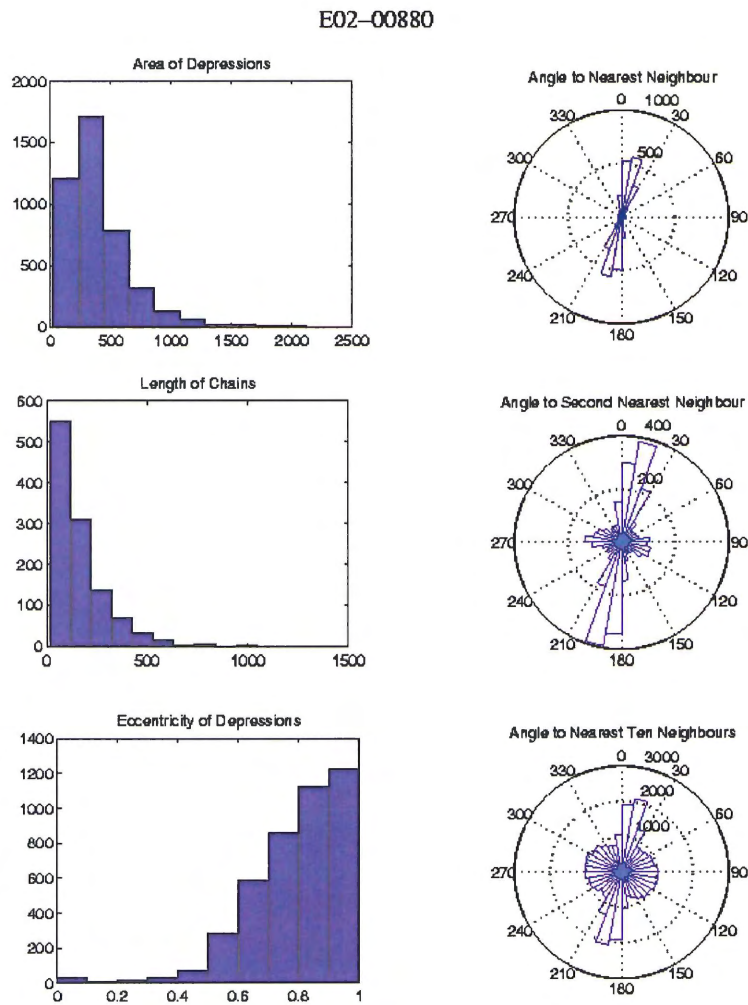


Figure D.1: Plots for MOC image E02-00880. Distribution histograms of: area on individual depressions (m^2), length of chains (m) and eccentricity of depressions (after Friend and Sinha, 1993). Rose plots of: angle to nearest neighbour, angle to second nearest neighbour and angle to the ten nearest neighbours of every depression.

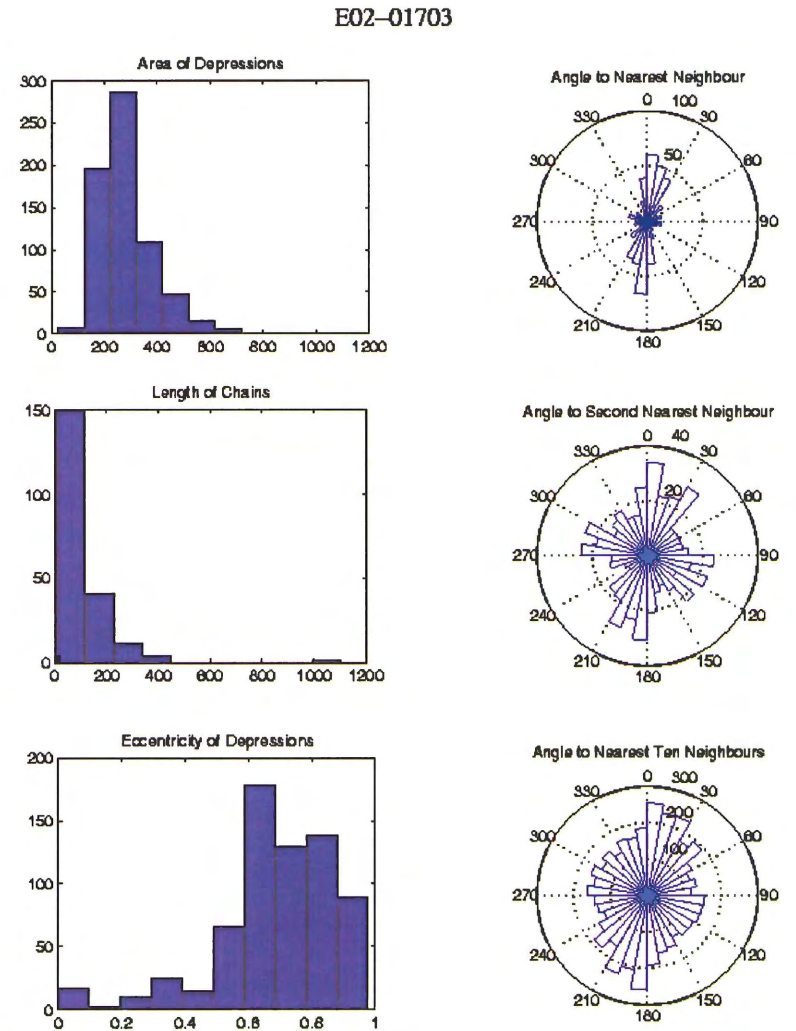


Figure D.2: Plots for MOC image E02-01703. Distribution histograms of: area on individual depressions (m^2), length of chains (m) and eccentricity of depressions (after Friend and Sinha, 1993). Rose plots of: angle to nearest neighbour, angle to second nearest neighbour and angle to the ten nearest neighbours of every depression.

E04-00442

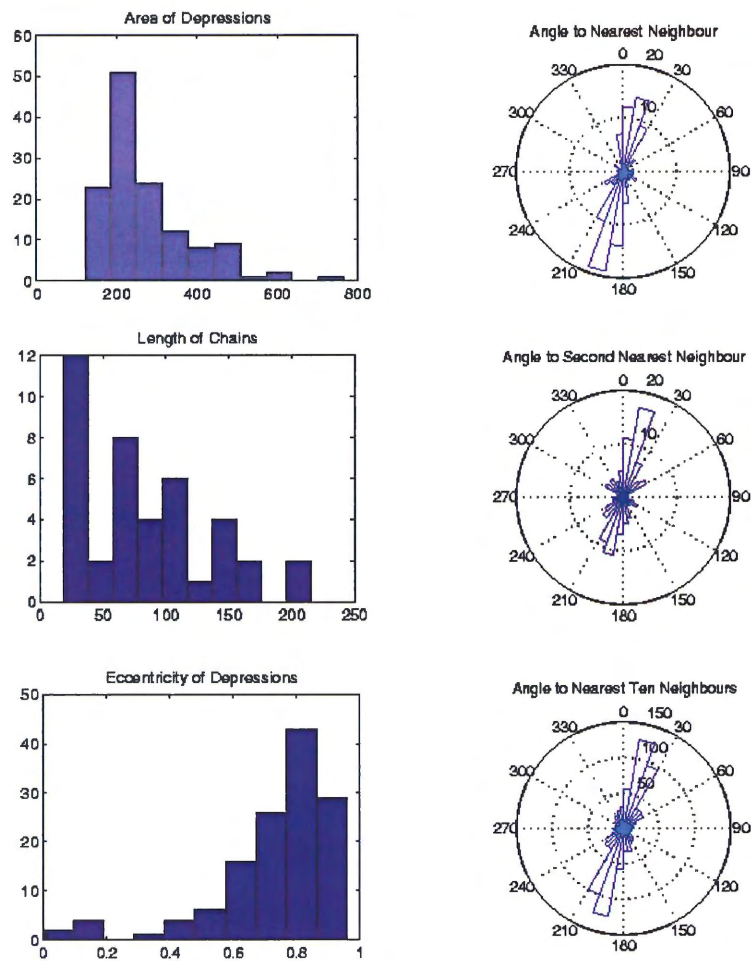


Figure D.3: Plots for MOC image E04-00442. Distribution histograms of: area on individual depressions (m^2), length of chains (m) and eccentricity of depressions (after Friend and Sinha, 1993). Rose plots of: angle to nearest neighbour, angle to second nearest neighbour and angle to the ten nearest neighbours of every depression.

E04-01564

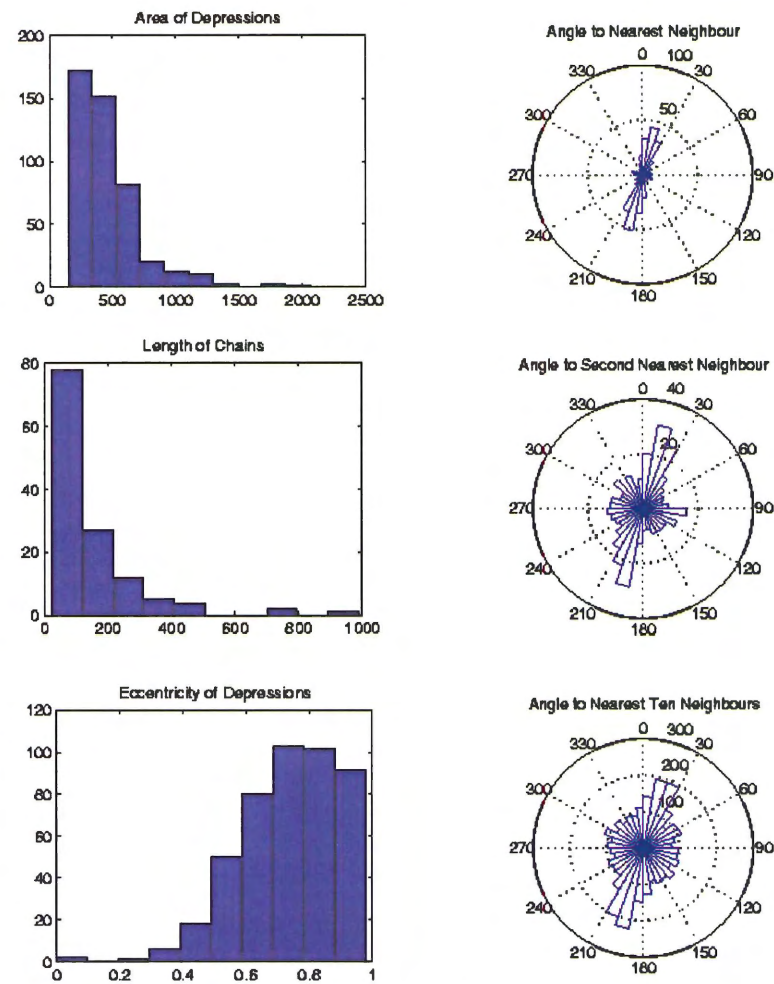


Figure D.4: Plots for MOC image E04-01564. Distribution histograms of: area on individual depressions (m^2), length of chains (m) and eccentricity of depressions (after Friend and Sinha, 1993). Rose plots of: angle to nearest neighbour, angle to second nearest neighbour and angle to the ten nearest neighbours of every depression.

E05-00488

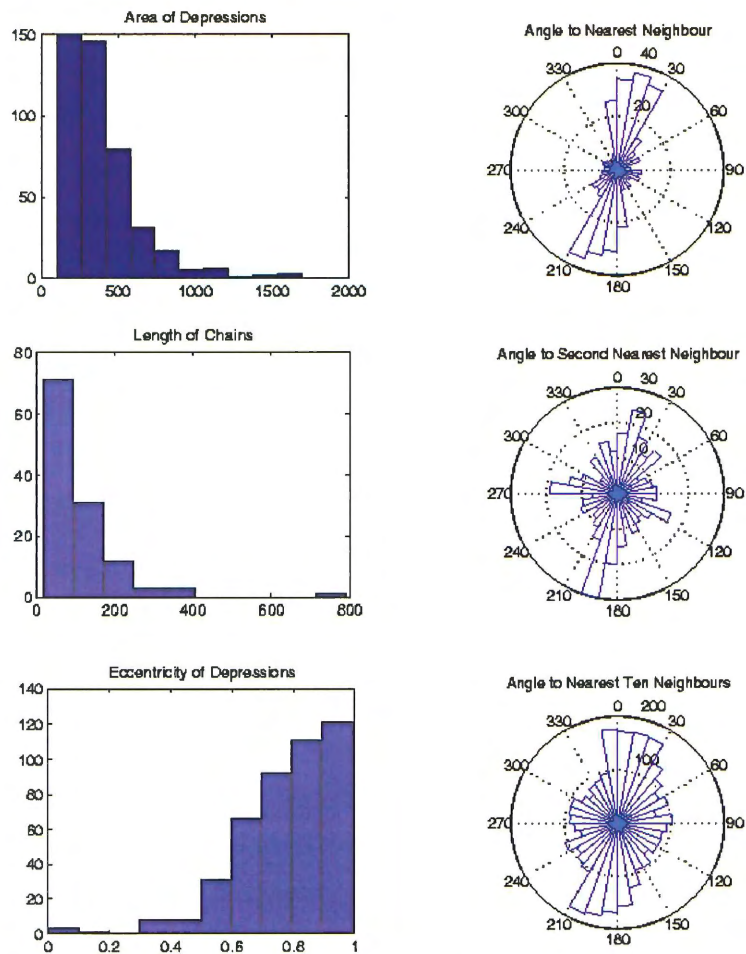


Figure D.5: Plots for MOC image E05-00488. Distribution histograms of: area on individual depressions (m^2), length of chains (m) and eccentricity of depressions (after Friend and Sinha, 1993). Rose plots of: angle to nearest neighbour, angle to second nearest neighbour and angle to the ten nearest neighbours of every depression.

E05-02576

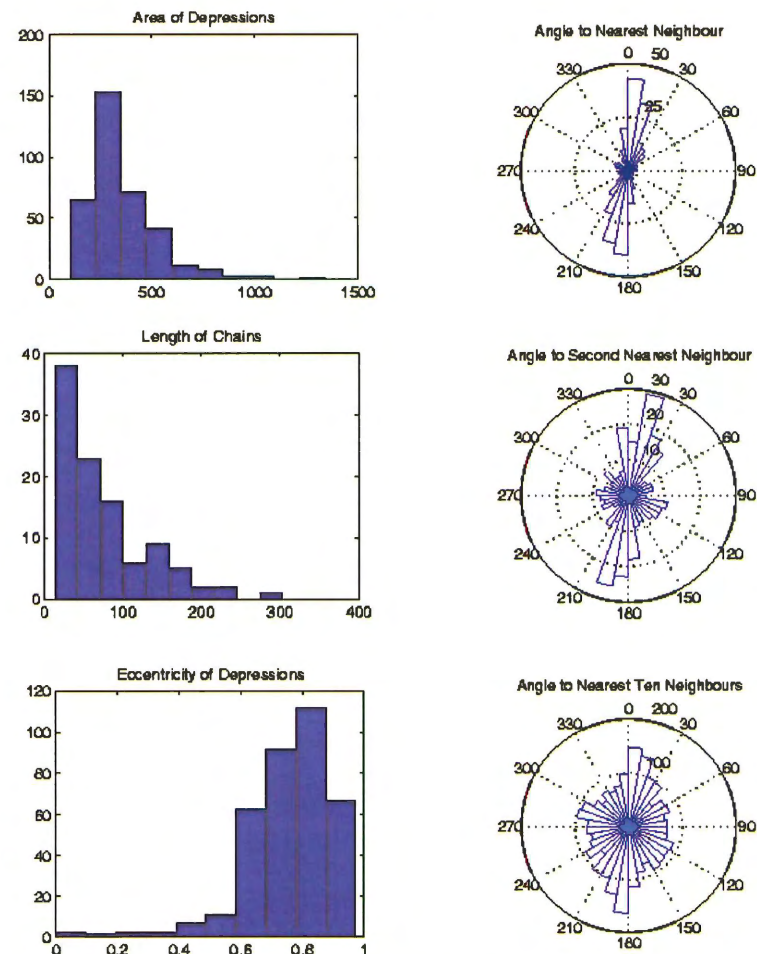


Figure D.6: Plots for MOC image E05-02576. Distribution histograms of: area on individual depressions (m^2), length of chains (m) and eccentricity of depressions (after Friend and Sinha, 1993). Rose plots of: angle to nearest neighbour, angle to second nearest neighbour and angle to the ten nearest neighbours of every depression.

M02-03335

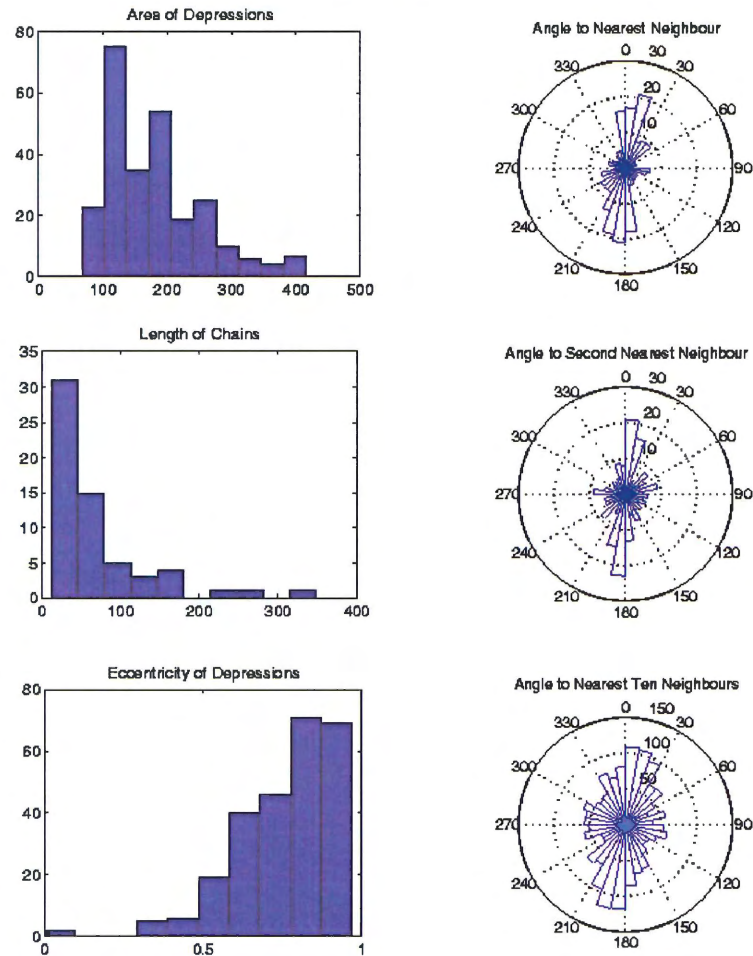


Figure D.7: Plots for MOC image M02-03335. Distribution histograms of: area on individual depressions (m^2), length of chains (m) and eccentricity of depressions (after Friend and Sinha, 1993). Rose plots of: angle to nearest neighbour, angle to second nearest neighbour and angle to the ten nearest neighbours of every depression.

M03-04331

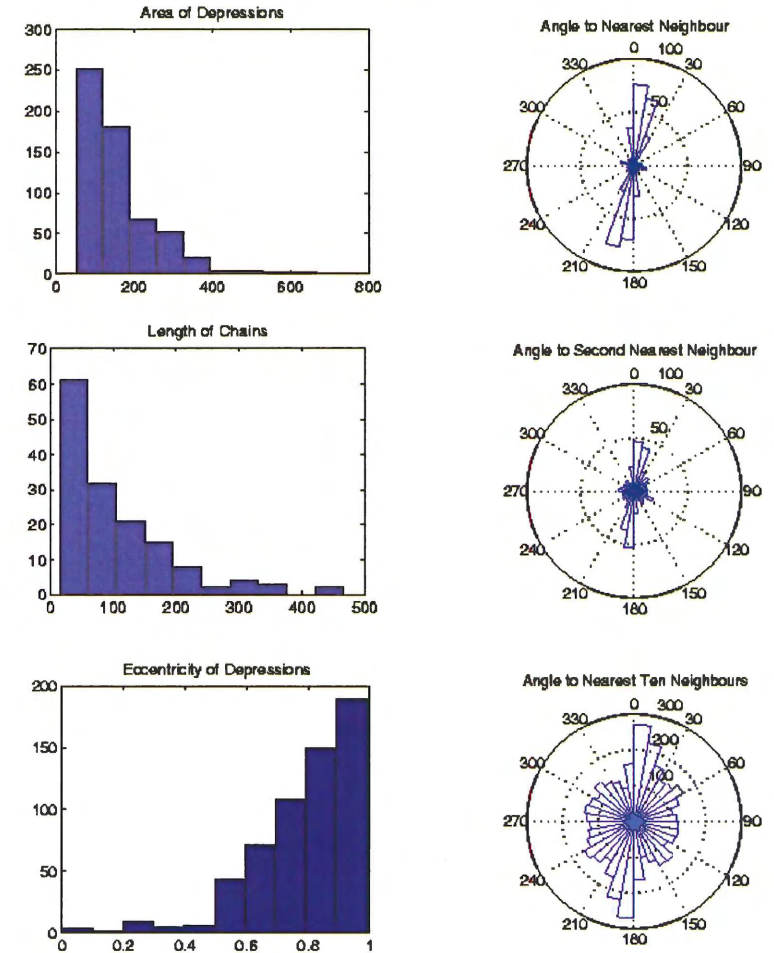


Figure D.8: Plots for MOC image M03-04331. Distribution histograms of: area on individual depressions (m^2), length of chains (m) and eccentricity of depressions (after Friend and Sinha, 1993). Rose plots of: angle to nearest neighbour, angle to second nearest neighbour and angle to the ten nearest neighbours of every depression.

M03-05064

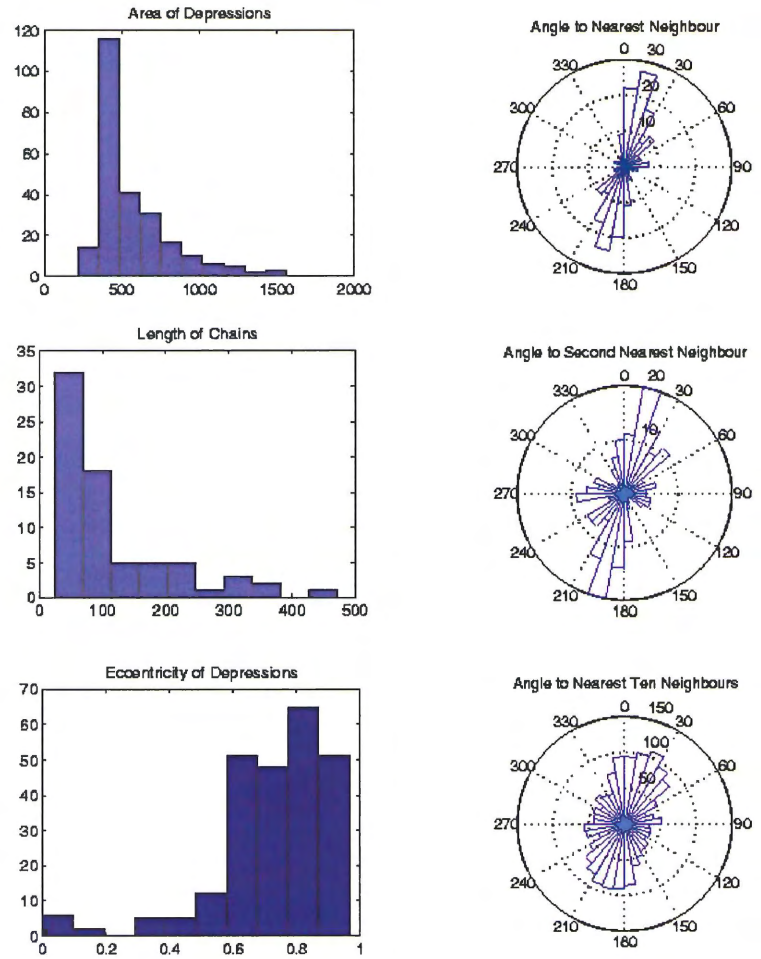


Figure D.9: Plots for MOC image M03-05064. Distribution histograms of: area on individual depressions (m^2), length of chains (m) and eccentricity of depressions (after Friend and Sinha, 1993). Rose plots of: angle to nearest neighbour, angle to second nearest neighbour and angle to the ten nearest neighbours of every depression.

M03-05694

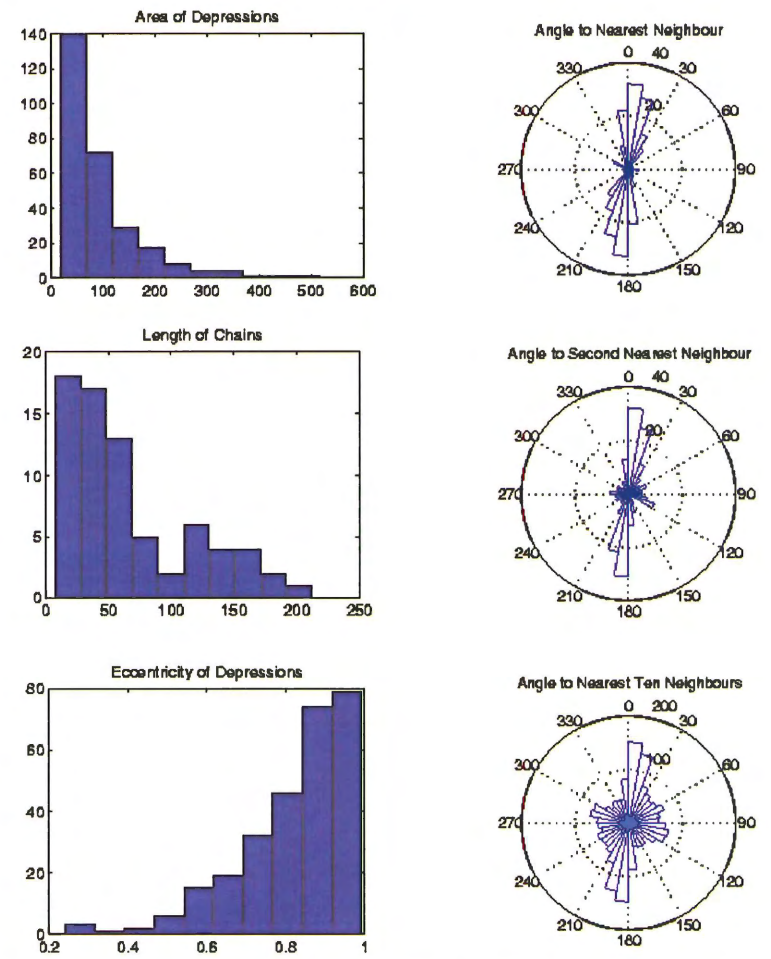


Figure D.10: Plots for MOC image M03-05694. Distribution histograms of: area on individual depressions (m^2), length of chains (m) and eccentricity of depressions (after Friend and Sinha, 1993). Rose plots of: angle to nearest neighbour, angle to second nearest neighbour and angle to the ten nearest neighbours of every depression.

M04-00990

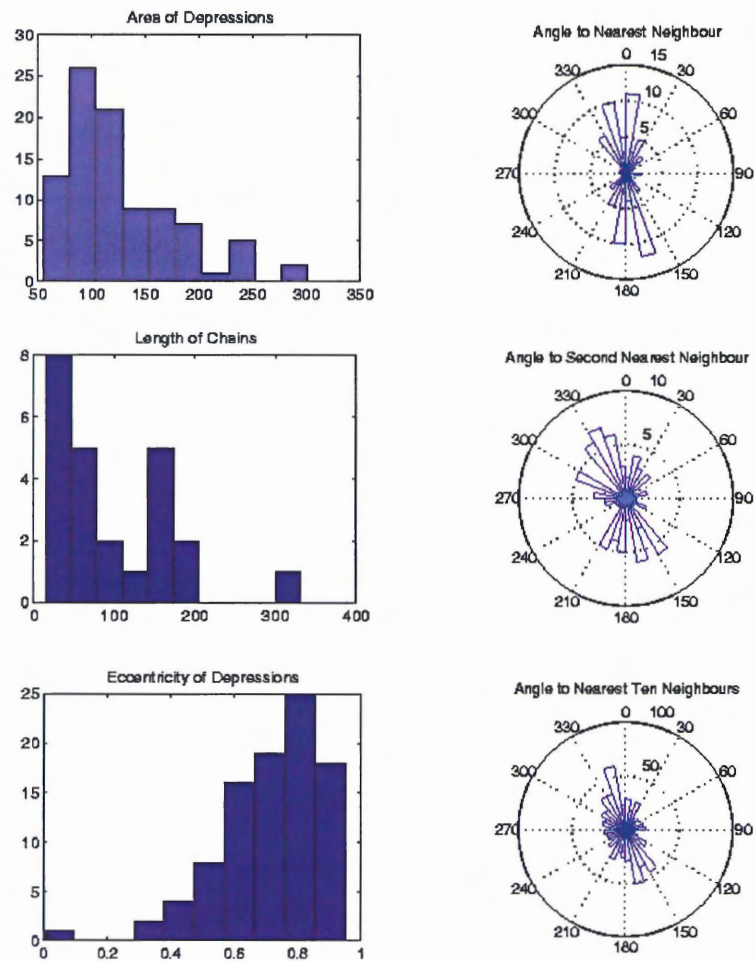


Figure D.11: Plots for MOC image M04-00990. Distribution histograms of: area on individual depressions (m^2), length of chains (m) and eccentricity of depressions (after Friend and Sinha, 1993). Rose plots of: angle to nearest neighbour, angle to second nearest neighbour and angle to the ten nearest neighbours of every depression.

M04-01440

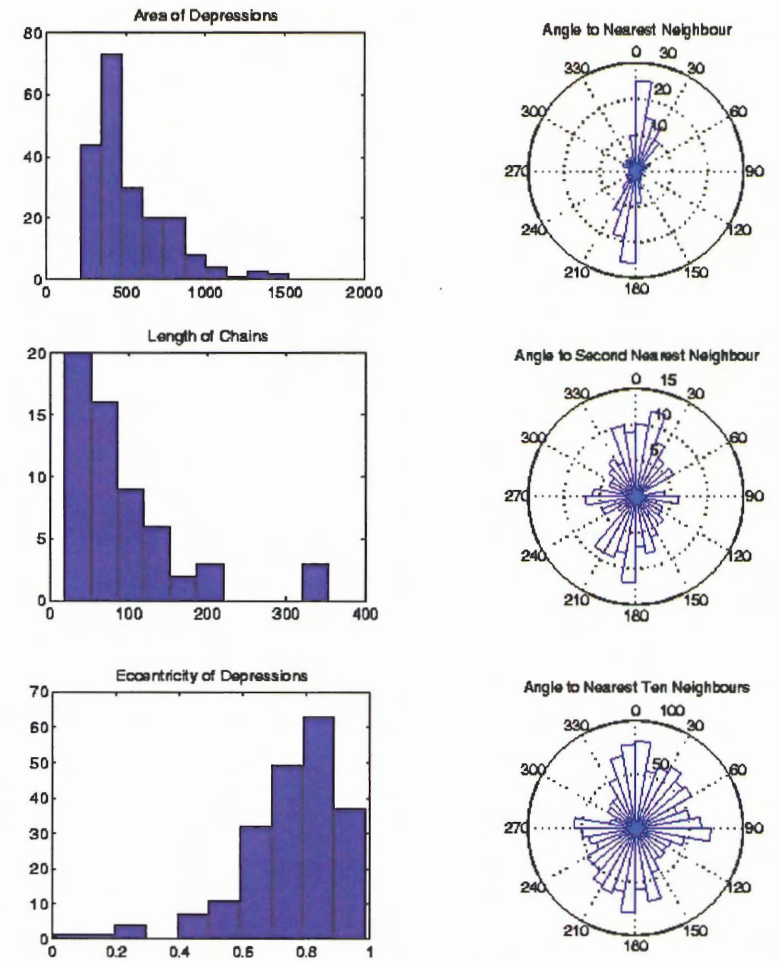


Figure D.12: Plots for MOC image M04-01440. Distribution histograms of: area on individual depressions (m^2), length of chains (m) and eccentricity of depressions (after Friend and Sinha, 1993). Rose plots of: angle to nearest neighbour, angle to second nearest neighbour and angle to the ten nearest neighbours of every depression.

M04-01631

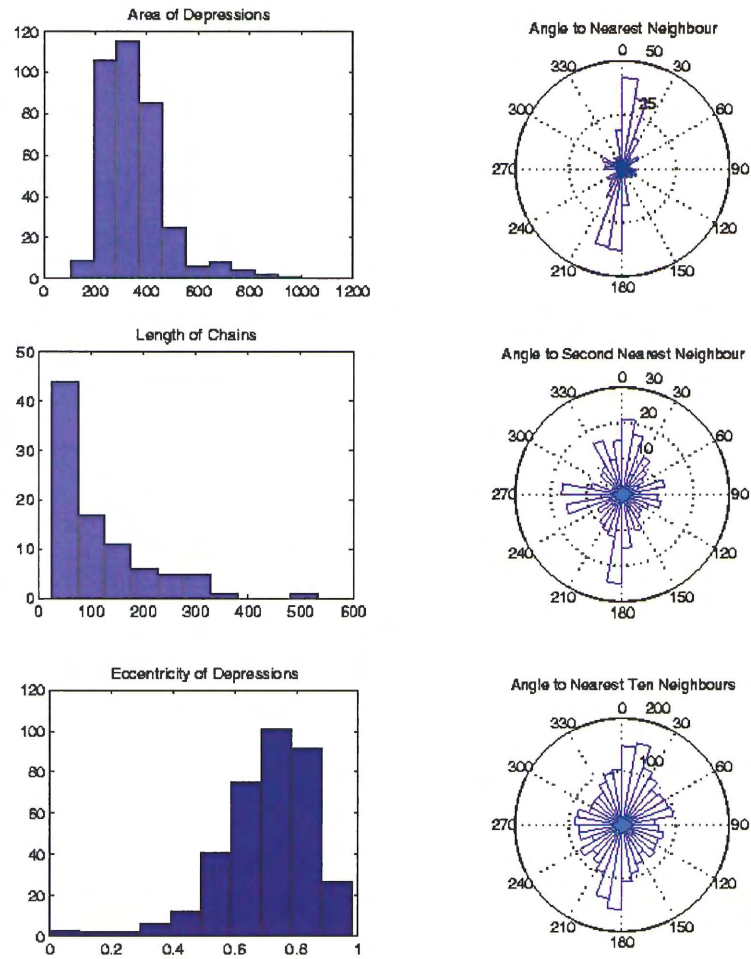


Figure D.13: Plots for MOC image M04-01631. Distribution histograms of: area on individual depressions (m^2), length of chains (m) and eccentricity of depressions (after Friend and Sinha, 1993). Rose plots of: angle to nearest neighbour, angle to second nearest neighbour and angle to the ten nearest neighbours of every depression.

M04-02077

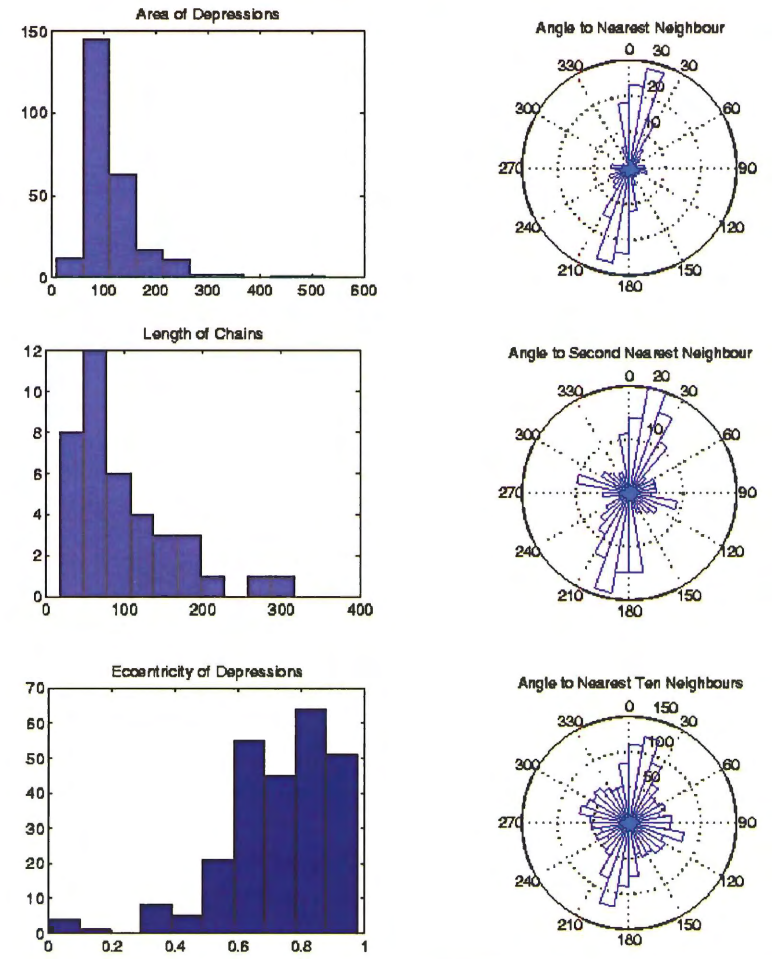


Figure D.14: Plots for MOC image M04-02077. Distribution histograms of: area on individual depressions (m^2), length of chains (m) and eccentricity of depressions (after Friend and Sinha, 1993). Rose plots of: angle to nearest neighbour, angle to second nearest neighbour and angle to the ten nearest neighbours of every depression.

M04-02704

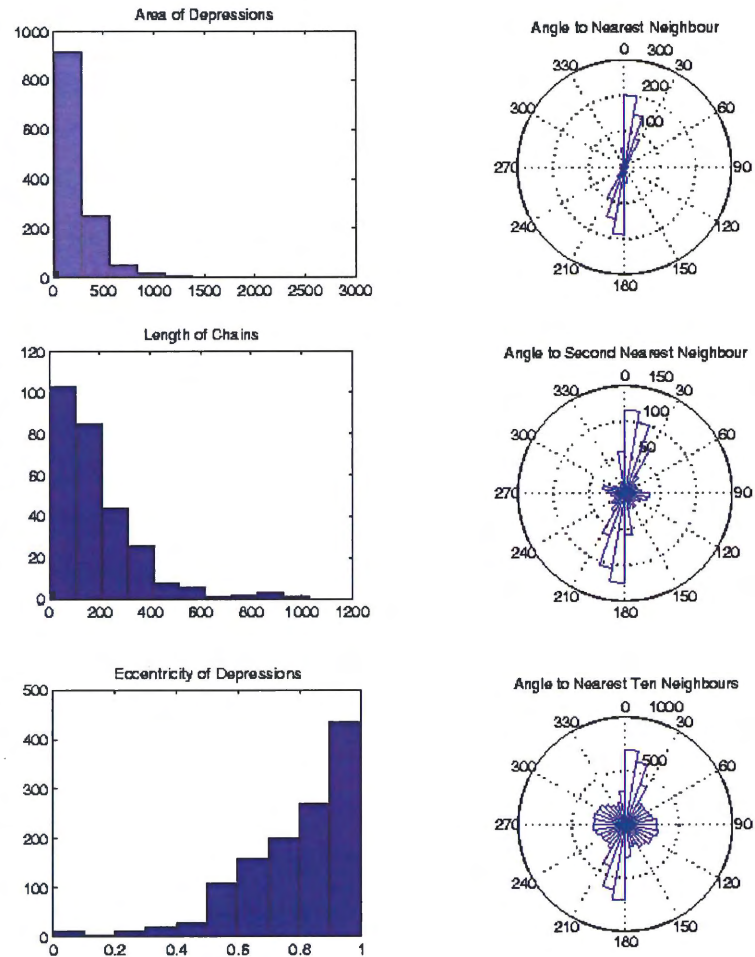


Figure D.15: Plots for MOC image M04-02704. Distribution histograms of: area on individual depressions (m^2), length of chains (m) and eccentricity of depressions (after Friend and Sinha, 1993). Rose plots of: angle to nearest neighbour, angle to second nearest neighbour and angle to the ten nearest neighbours of every depression.

M04-03810

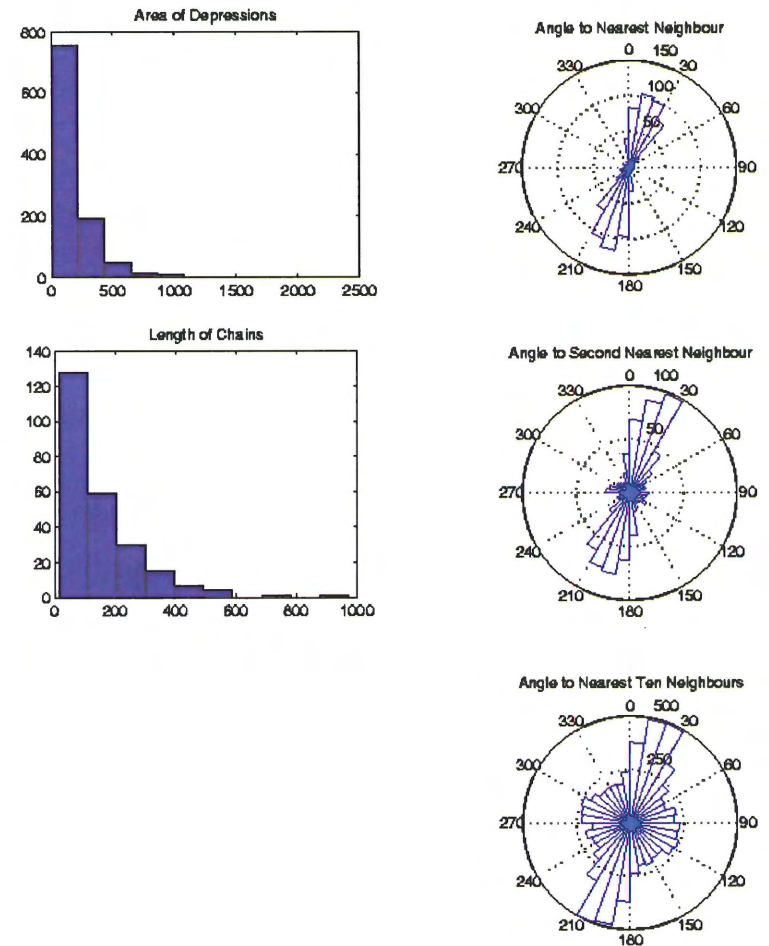


Figure D.16: Plots for MOC image M04-03810. Distribution histograms of: area on individual depressions (m^2), length of chains (m). Rose plots of: angle to nearest neighbour, angle to second nearest neighbour and angle to the ten nearest neighbours of every depression.

M04-04181

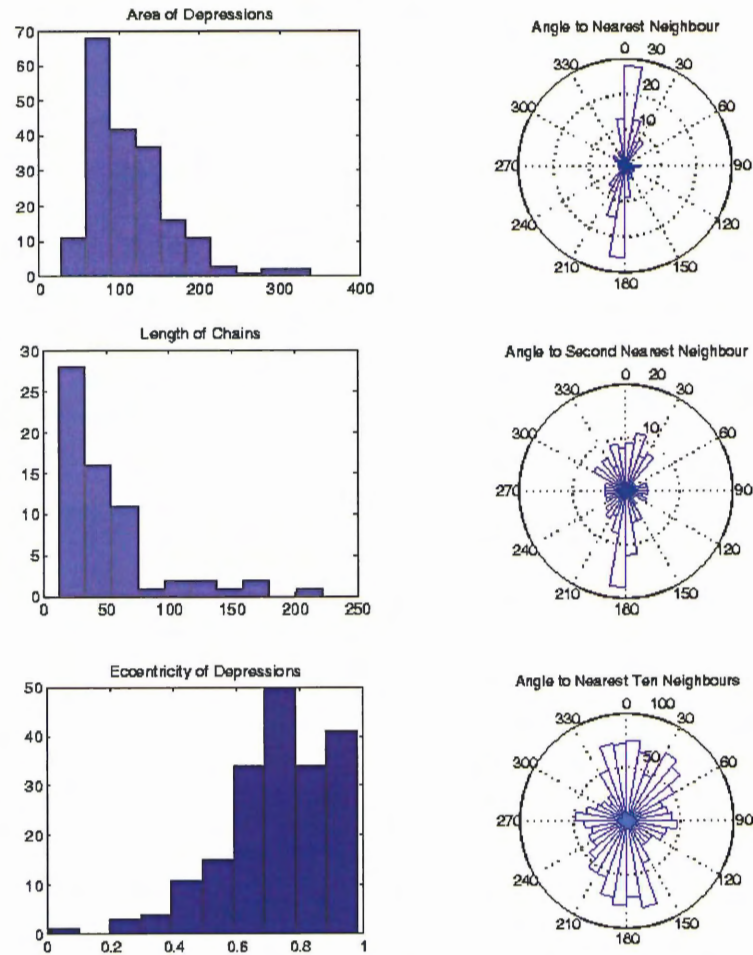


Figure D.17: Plots for MOC image M04-04181. Distribution histograms of: area on individual depressions (m^2), length of chains (m) and eccentricity of depressions (after Friend and Sinha, 1993). Rose plots of: angle to nearest neighbour, angle to second nearest neighbour and angle to the ten nearest neighbours of every depression.

M08-03534

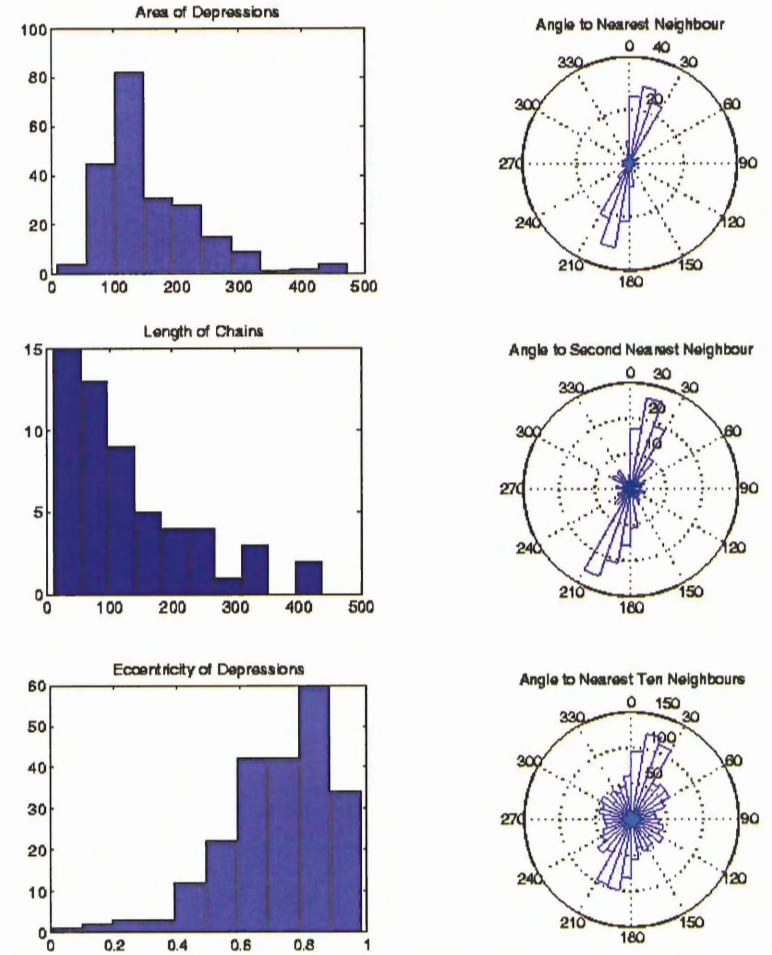


Figure D.18: Plots for MOC image M08-03534. Distribution histograms of: area on individual depressions (m^2), length of chains (m) and eccentricity of depressions (after Friend and Sinha, 1993). Rose plots of: angle to nearest neighbour, angle to second nearest neighbour and angle to the ten nearest neighbours of every depression.

M08-07602

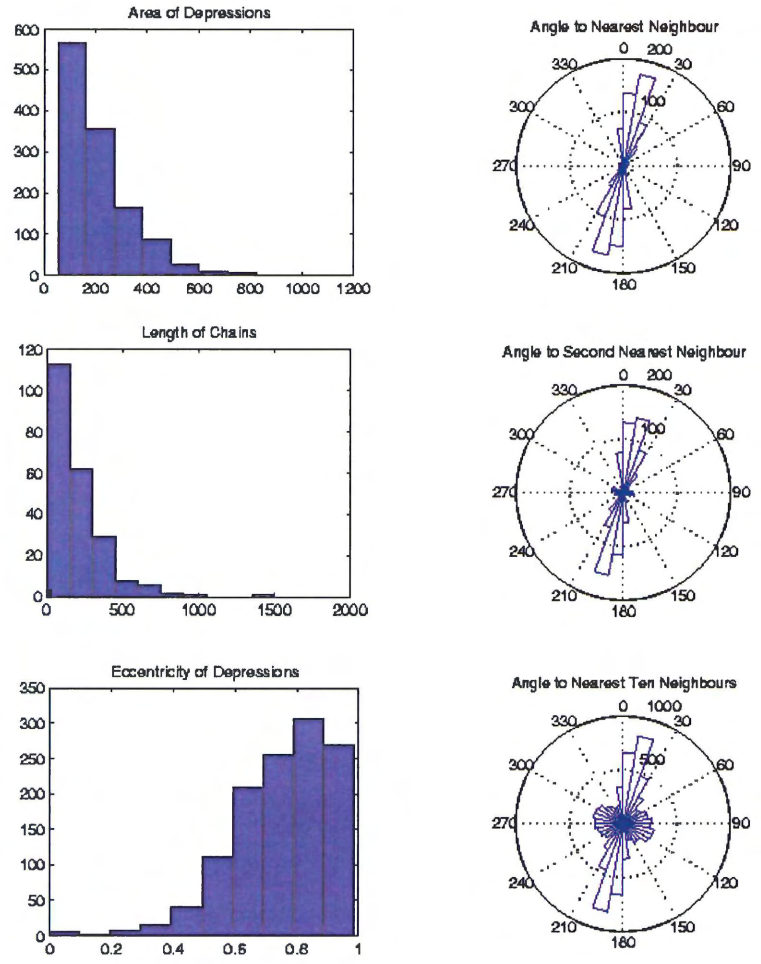


Figure D.19: Plots for MOC image M08-07602. Distribution histograms of: area on individual depressions (m^2), length of chains (m) and eccentricity of depressions (after Friend and Sinha, 1993). Rose plots of: angle to nearest neighbour, angle to second nearest neighbour and angle to the ten nearest neighbours of every depression.

M15-00675

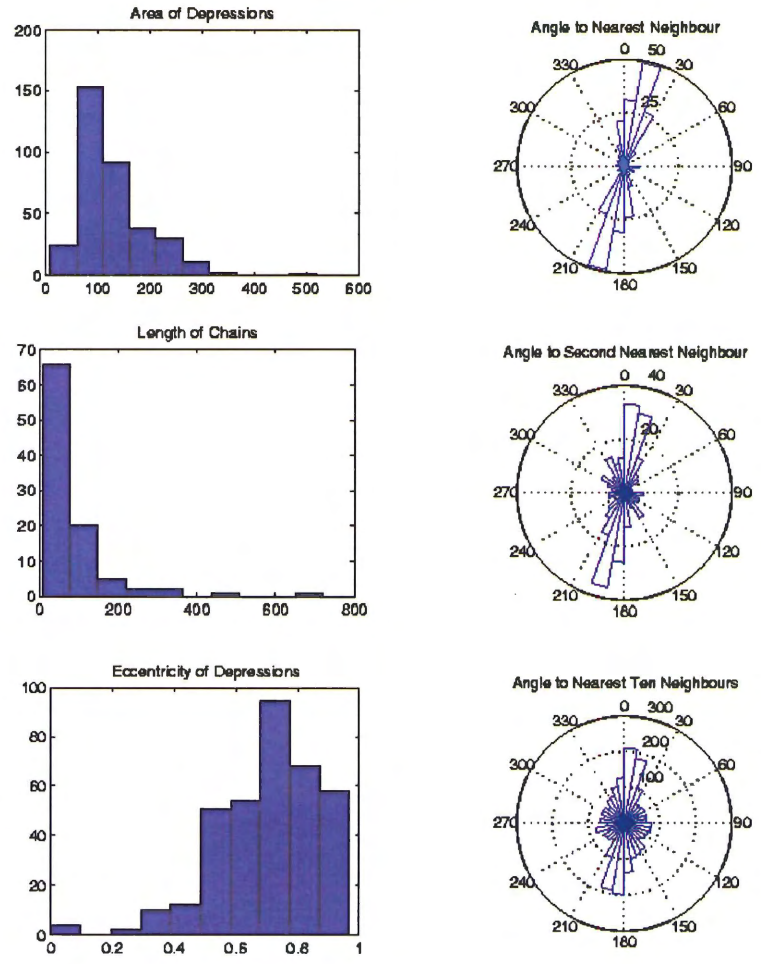


Figure D.20: Plots for MOC image M15-00675. Distribution histograms of: area on individual depressions (m^2), length of chains (m) and eccentricity of depressions (after Friend and Sinha, 1993). Rose plots of: angle to nearest neighbour, angle to second nearest neighbour and angle to the ten nearest neighbours of every depression.

M18-00441

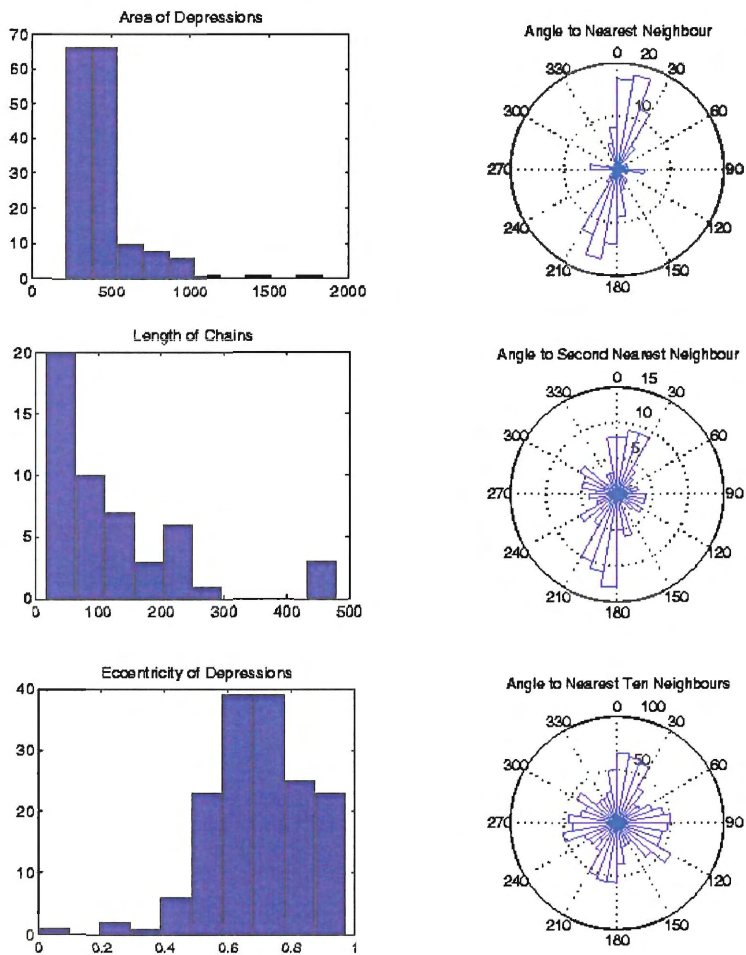


Figure D.21: Plots for MOC image M18-00441. Distribution histograms of: area on individual depressions (m^2), length of chains (m) and eccentricity of depressions (after Friend and Sinha, 1993). Rose plots of: angle to nearest neighbour, angle to second nearest neighbour and angle to the ten nearest neighbours of every depression.

M19-01326

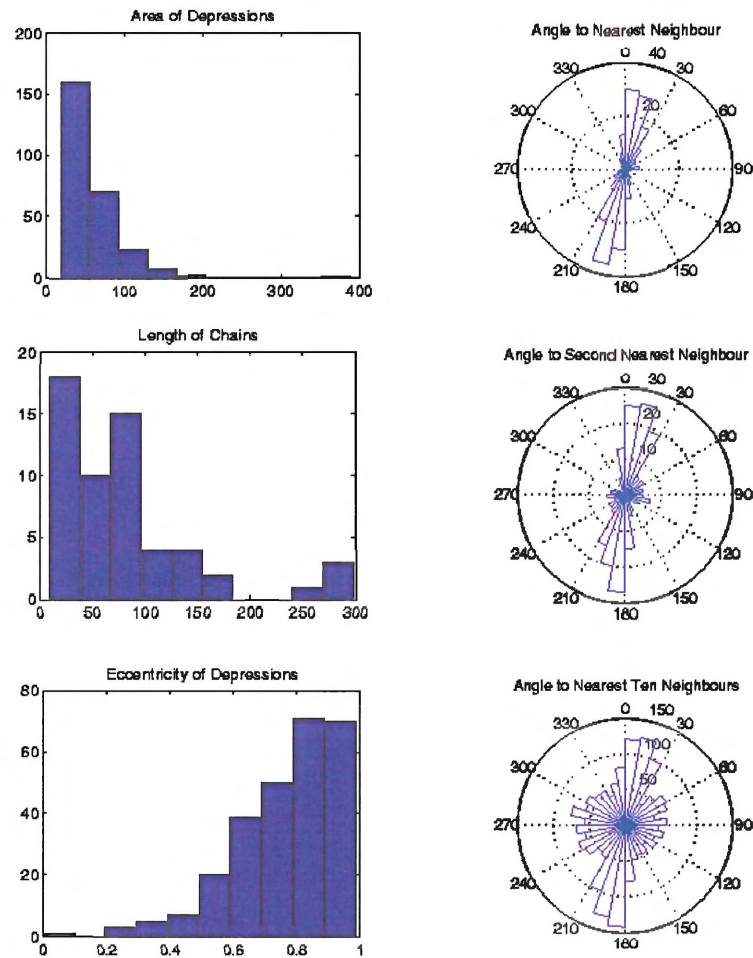


Figure D.22: Plots for MOC image M19-01326. Distribution histograms of: area on individual depressions (m^2), length of chains (m) and eccentricity of depressions (after Friend and Sinha, 1993). Rose plots of: angle to nearest neighbour, angle to second nearest neighbour and angle to the ten nearest neighbours of every depression.

M19-01929

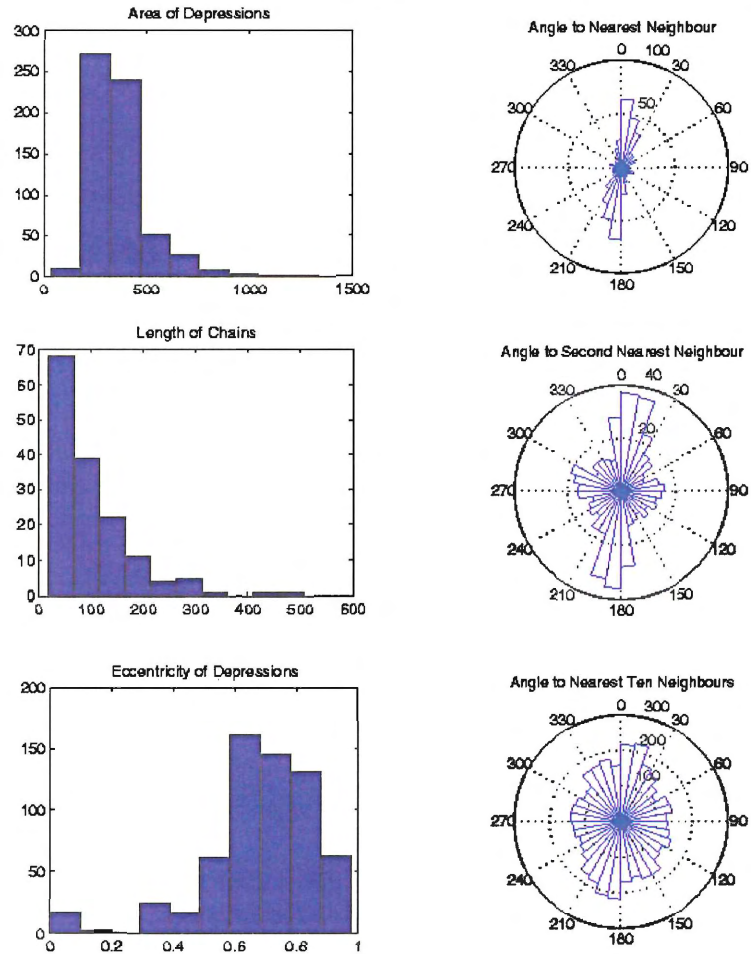


Figure D.23: Plots for MOC image M19-01929. Distribution histograms of: area on individual depressions (m^2), length of chains (m) and eccentricity of depressions (after Friend and Sinha, 1993). Rose plots of: angle to nearest neighbour, angle to second nearest neighbour and angle to the ten nearest neighbours of every depression.

M23-00151

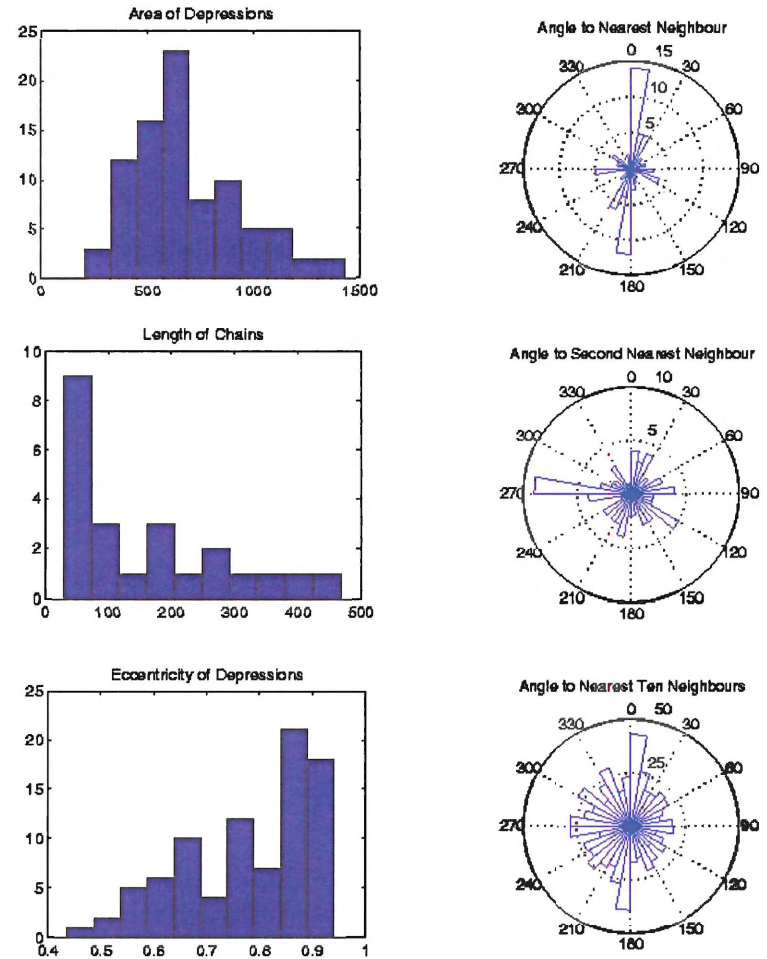


Figure D.24: Plots for MOC image M23-00151. Distribution histograms of: area on individual depressions (m^2), length of chains (m) and eccentricity of depressions (after Friend and Sinha, 1993). Rose plots of: angle to nearest neighbour, angle to second nearest neighbour and angle to the ten nearest neighbours of every depression.

APPENDIX E – Graphs for terrestrial pattern model

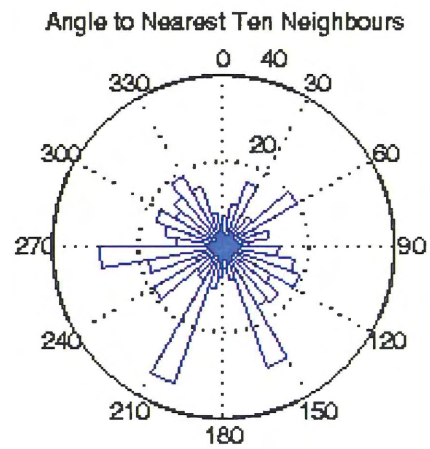
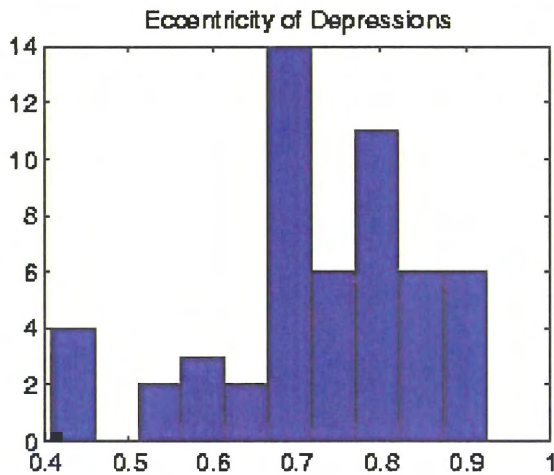
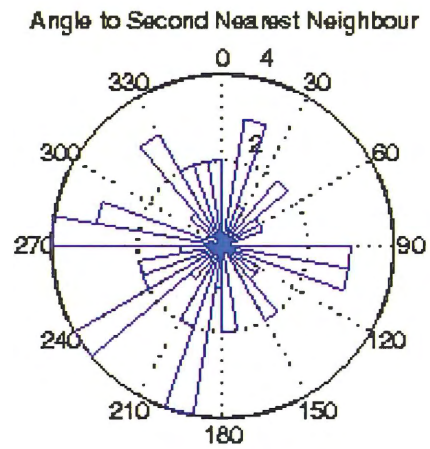
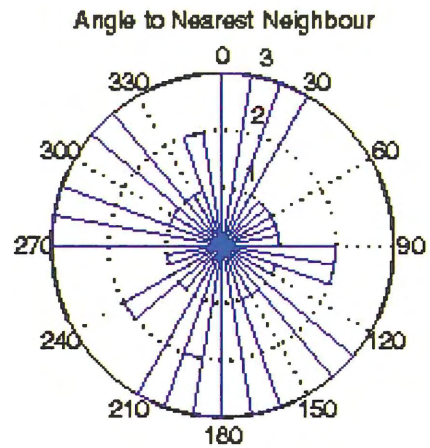
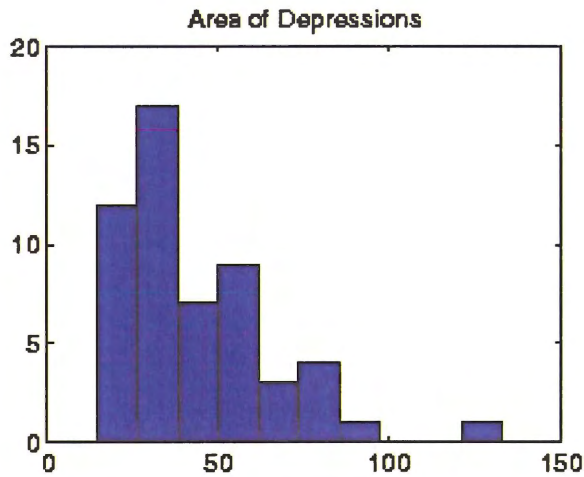


Figure E.1: Plots for Aerial photograph 19F2487. Distribution histograms of: area of individual depressions (m^2), length of chains (m) and eccentricity of depressions (after Friend and Sinha, 1993). Rose plots of: angle to nearest neighbour, angle to second nearest neighbour and angle to the ten nearest neighbours of every depression.

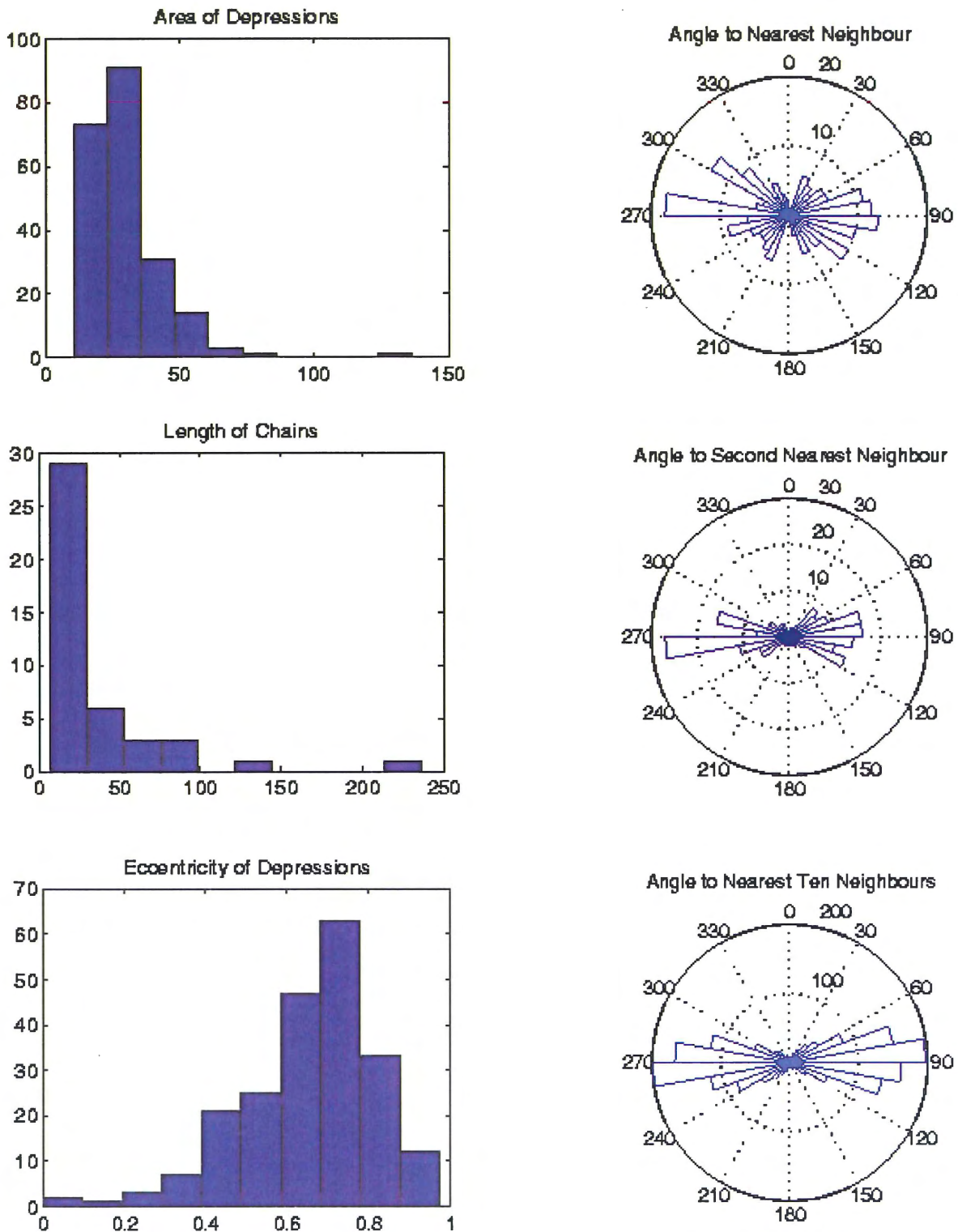


Figure E.2: Plots for Aerial photograph 20F2421. Distribution histograms of: area of individual depressions (m^2), length of chains (m) and eccentricity of depressions (after Friend and Sinha, 1993). Rose plots of: angle to nearest neighbour, angle to second nearest neighbour and angle to the ten nearest neighbours of every depression.

20F2423

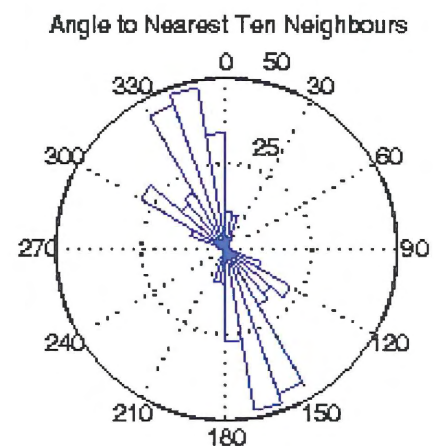
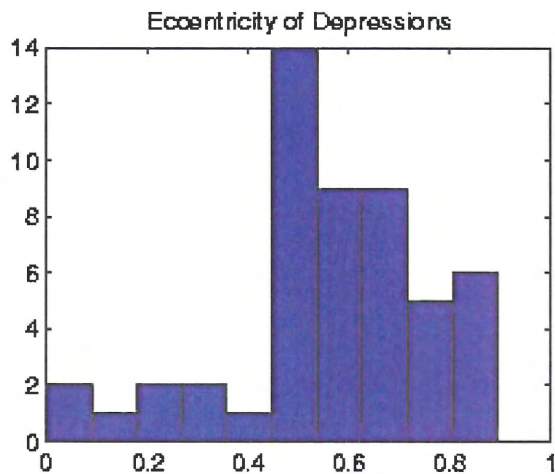
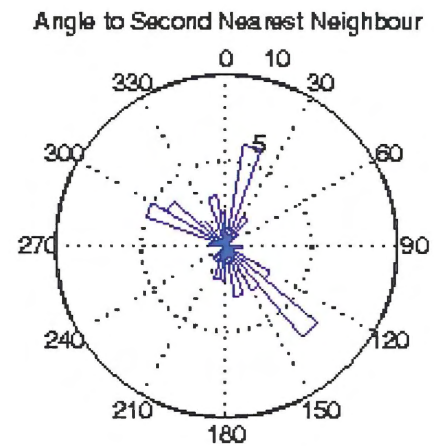
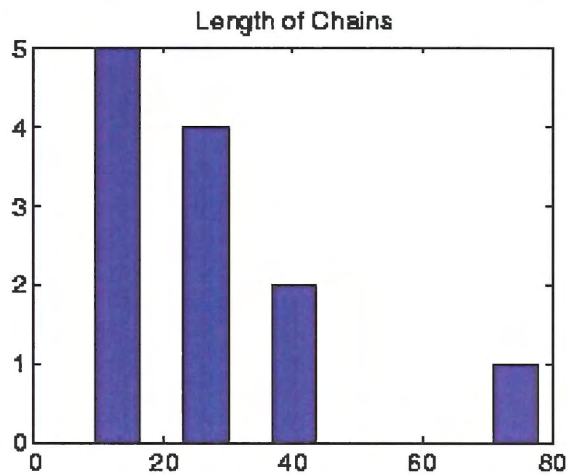
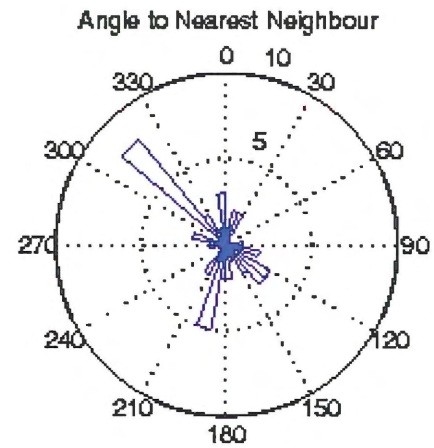
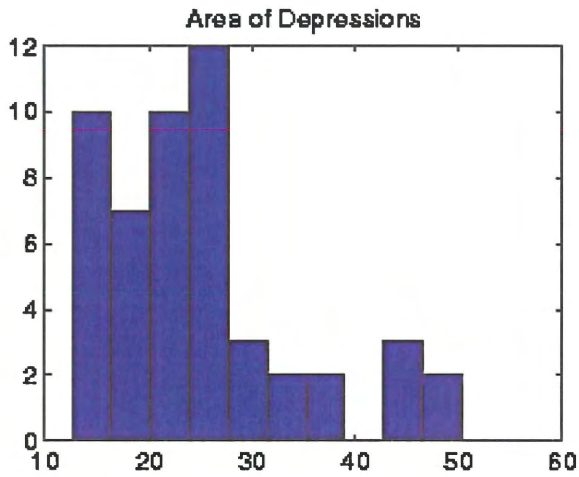


Figure E.3: Plots for Aerial photograph 20F2423. Distribution histograms of: area of individual depressions (m^2), length of chains (m) and eccentricity of depressions (after Friend and Sinha, 1993). Rose plots of: angle to nearest neighbour, angle to second nearest neighbour and angle to the ten nearest neighbours of every depression.

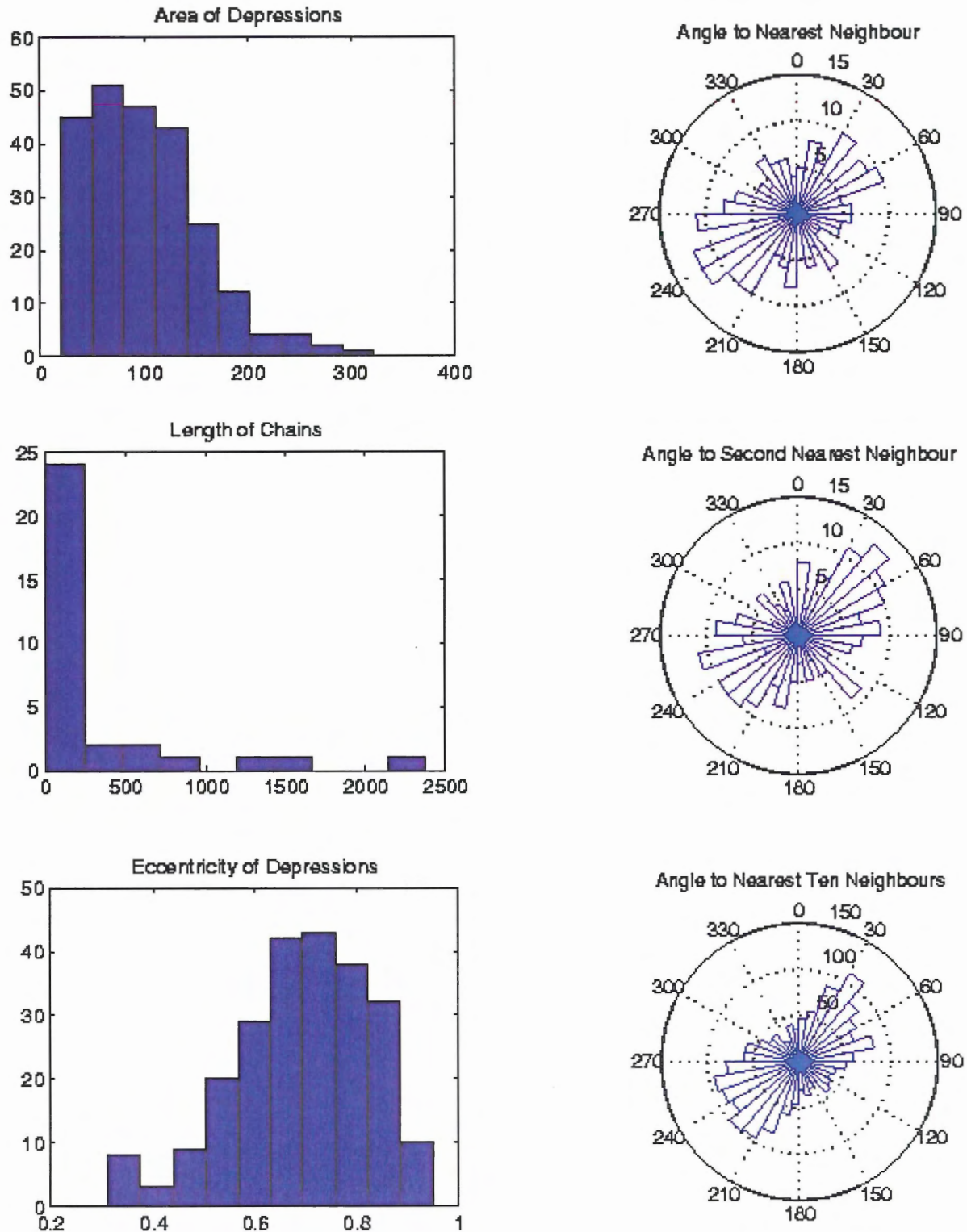


Figure E.4: Plots for Aerial photograph 23F5766. Distribution histograms of: area of individual depressions (m^2), length of chains (m) and eccentricity of depressions (after Friend and Sinha, 1993). Rose plots of: angle to nearest neighbour, angle to second nearest neighbour and angle to the ten nearest neighbours of every depression.

APPENDIX F – Graphs for synthetic model patterns

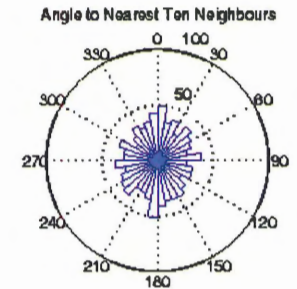
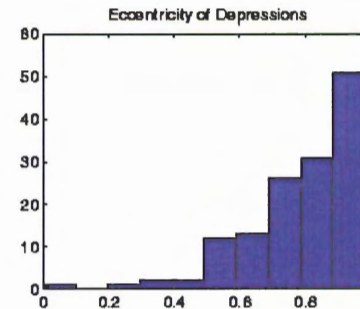
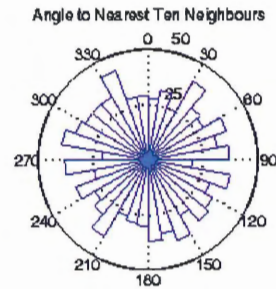
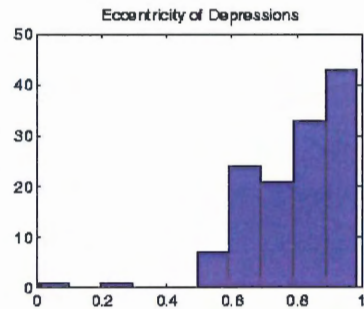
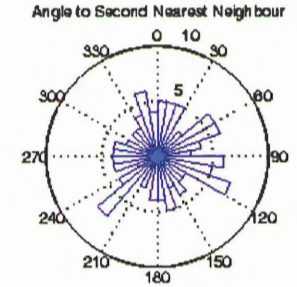
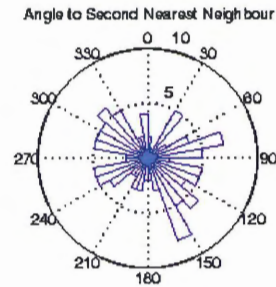
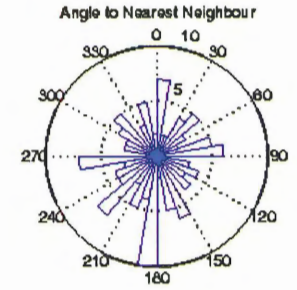
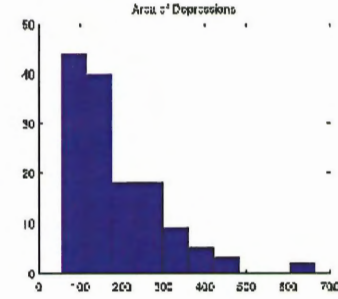
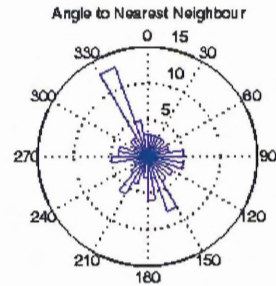
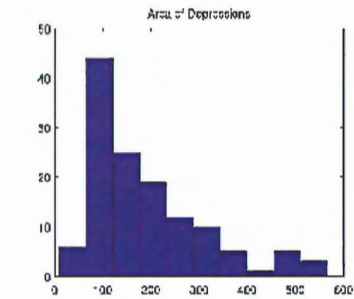


Figure F.1.a: Plots for MOC image E02-00880 model 1, randomly distributed depressions. Distribution histograms of: area of individual depressions (m^2) and eccentricity of depressions (after Friend and Sinha, 1993). Roseplots of: angle to nearest neighbour, angle to second nearest neighbour and angle to the ten nearest neighbours of every depression.

Figure F.1.b: Plots for MOC image E02-00880 model 2, random distribution of depressions along a polygonal network. Distribution histograms of: area of individual depressions (m^2) and eccentricity of depressions (after Friend and Sinha, 1993). Roseplots of: angle to nearest neighbour, angle to second nearest neighbour and angle to the ten nearest neighbours of every depression.

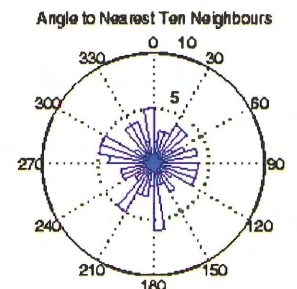
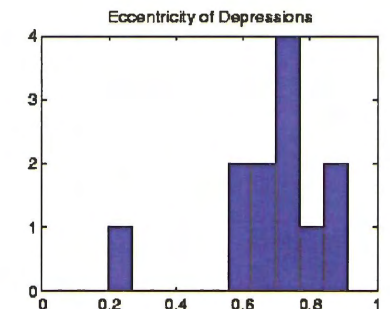
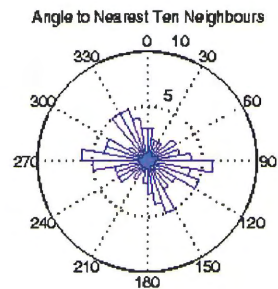
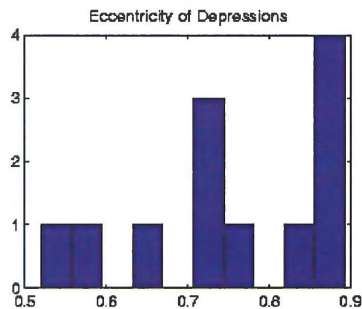
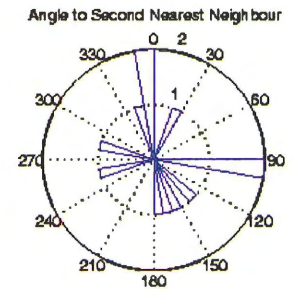
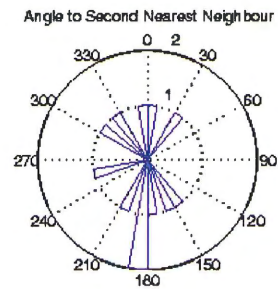
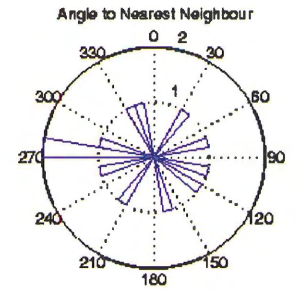
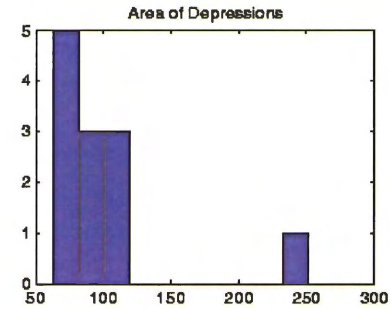
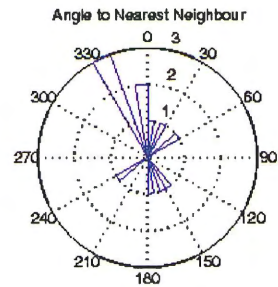
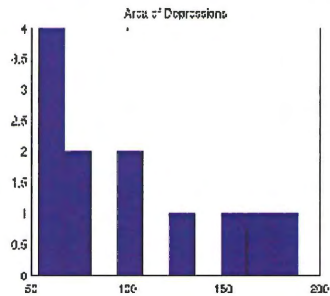


Figure F.2.a: Plots for MOC image E02-01703 model 1, randomly distributed depressions. Distribution histograms of: area of individual depressions (m^2) and eccentricity of depressions (after Friend and Sinha, 1993). Roseplots of: angle to nearest neighbour, angle to second nearest neighbour and angle to the ten nearest neighbours of every depression.

Figure F.2.b: Plots for MOC image E02-01703 model 2, random distribution of depressions along a polygonal network. Distribution histograms of: area of individual depressions (m^2) and eccentricity of depressions (after Friend and Sinha, 1993). Roseplots of: angle to nearest neighbour, angle to second nearest neighbour and angle to the ten nearest neighbours of every depression.

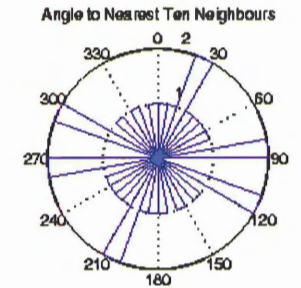
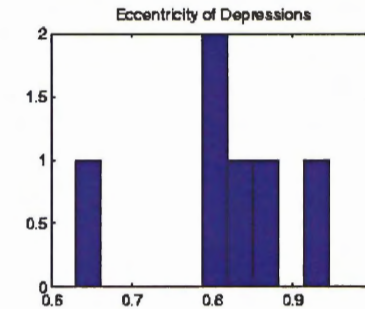
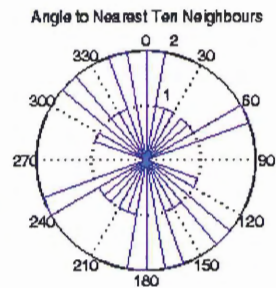
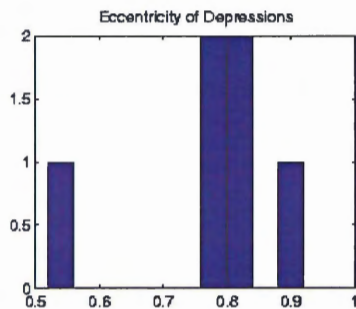
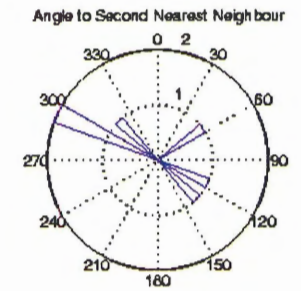
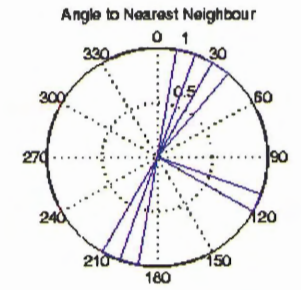
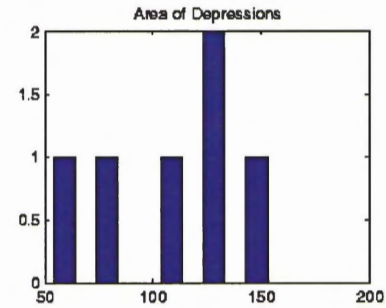
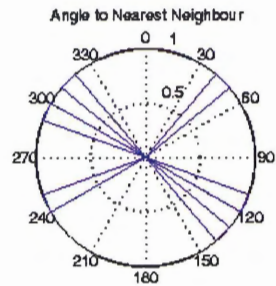
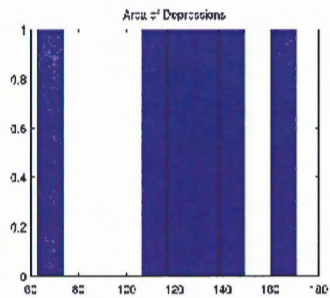


Figure F.3.a: Plots for MOC image E04-01564 model 1, randomly distributed depressions. Distribution histograms of: area of individual depressions (m^2) and eccentricity of depressions (after Friend and Sinha, 1993). Roseplots of: angle to nearest neighbour, angle to second nearest neighbour and angle to the ten nearest neighbours of every depression.

Figure F.3.b: Plots for MOC image E04-01564 model 2, random distribution of depressions along a polygonal network. Distribution histograms of: area of individual depressions (m^2) and eccentricity of depressions (after Friend and Sinha, 1993). Roseplots of: angle to nearest neighbour, angle to second nearest neighbour and angle to the ten nearest neighbours of every depression.

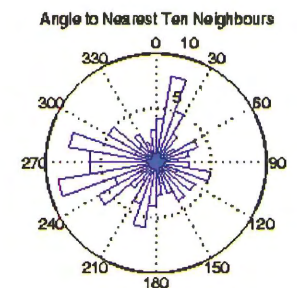
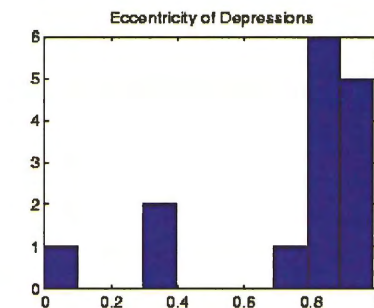
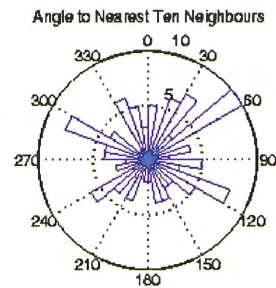
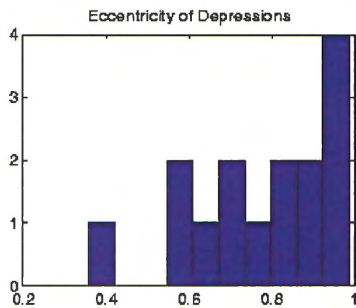
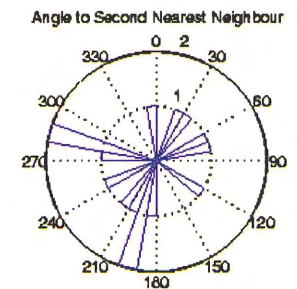
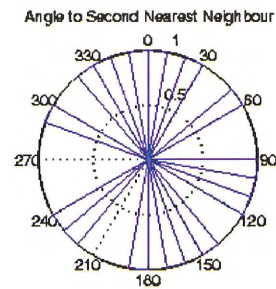
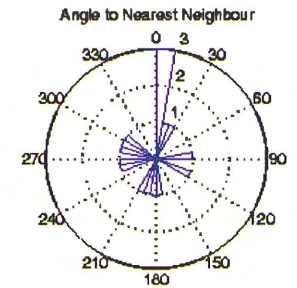
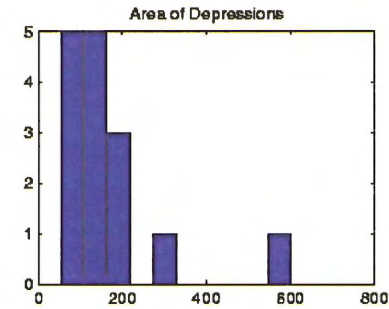
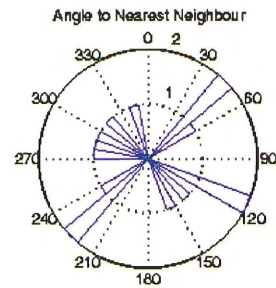
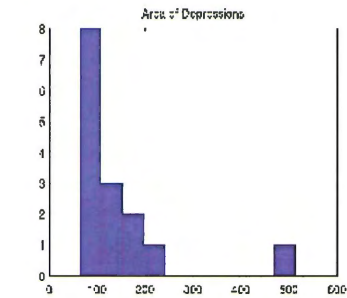


Figure F.4.a: Plots for MOC image E05-00488 model 1, randomly distributed depressions. Distribution histograms of: area of individual depressions (m^2) and eccentricity of depressions (after Friend and Sinha, 1993). Roseplots of: angle to nearest neighbour, angle to second nearest neighbour and angle to the ten nearest neighbours of every depression.

Figure F.4.b: Plots for MOC image E05-00488 model 2, random distribution of depressions along a polygonal network. Distribution histograms of: area of individual depressions (m^2) and eccentricity of depressions (after Friend and Sinha, 1993). Roseplots of: angle to nearest neighbour, angle to second nearest neighbour and angle to the ten nearest neighbours of every depression.

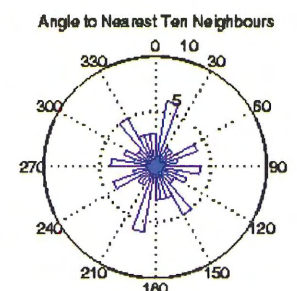
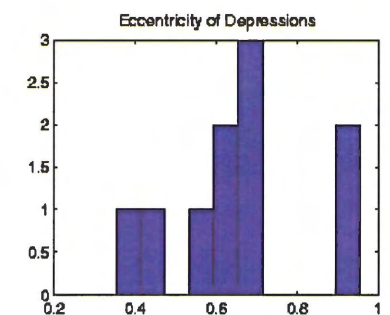
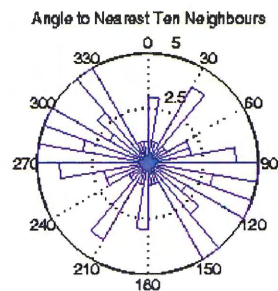
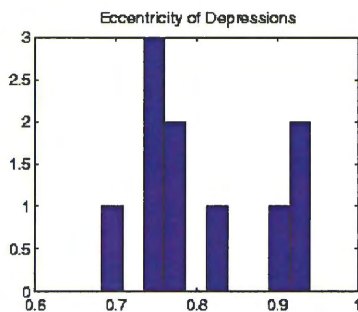
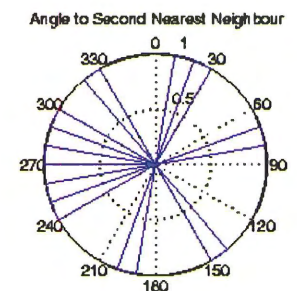
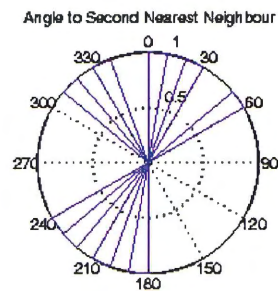
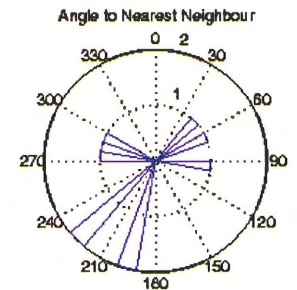
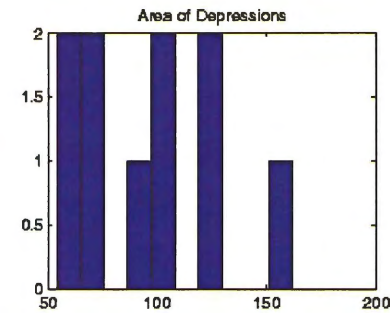
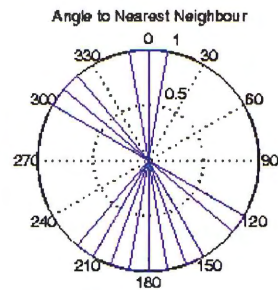
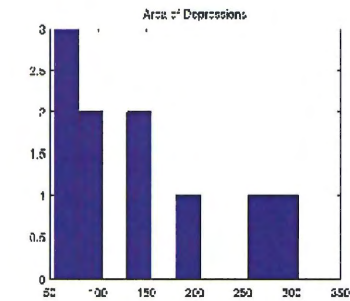


Figure F.5.a: Plots for MOC image E05-02576 model 1, randomly distributed depressions. Distribution histograms of: area of individual depressions (m^2) and eccentricity of depressions (after Friend and Sinha, 1993). Roseplots of: angle to nearest neighbour, angle to second nearest neighbour and angle to the ten nearest neighbours of every depression.

Figure F.5.b: Plots for MOC image E05-02576 model 2, random distribution of depressions along a polygonal network. Distribution histograms of: area of individual depressions (m^2) and eccentricity of depressions (after Friend and Sinha, 1993). Roseplots of: angle to nearest neighbour, angle to second nearest neighbour and angle to the ten nearest neighbours of every depression.

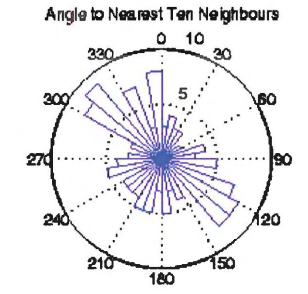
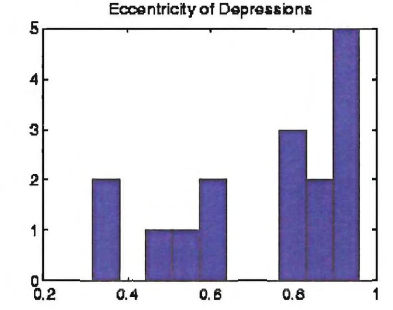
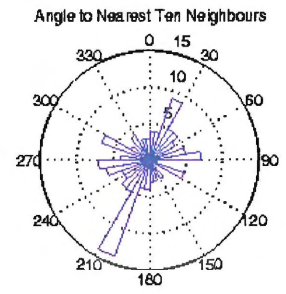
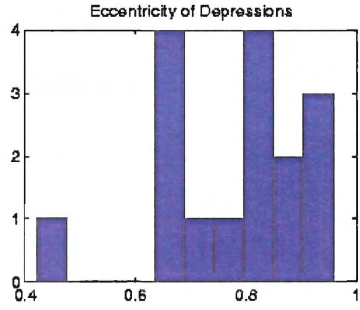
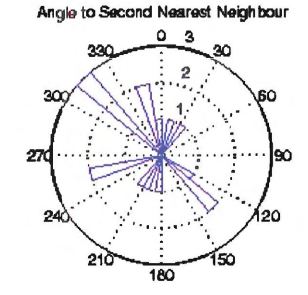
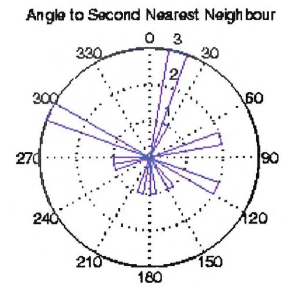
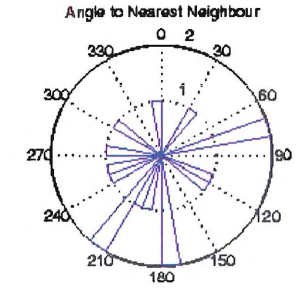
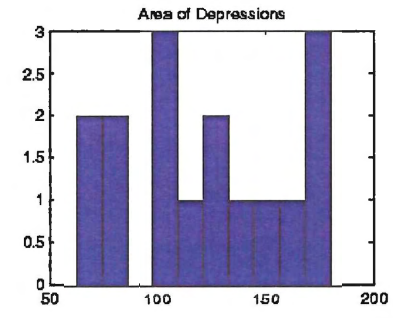
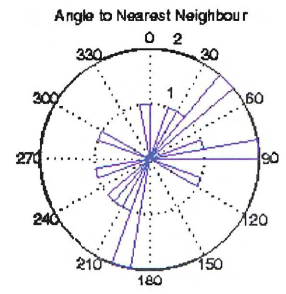
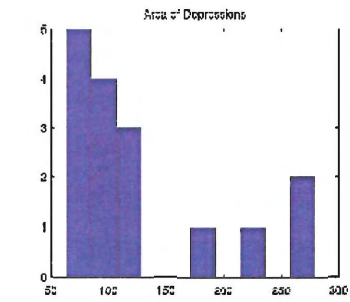


Figure F.6.a: Plots for MOC image M02-03335 model 1, randomly distributed depressions. Distribution histograms of: area of individual depressions (m^2) and eccentricity of depressions (after Friend and Sinha, 1993). Roseplots of: angle to nearest neighbour, angle to second nearest neighbour and angle to the ten nearest neighbours of every depression.

Figure F.6.b: Plots for MOC image M02-03335 model 2, random distribution of depressions along a polygonal network. Distribution histograms of: area of individual depressions (m^2) and eccentricity of depressions (after Friend and Sinha, 1993). Roseplots of: angle to nearest neighbour, angle to second nearest neighbour and angle to the ten nearest neighbours of every depression.

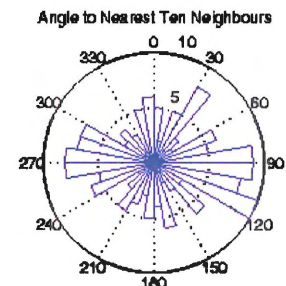
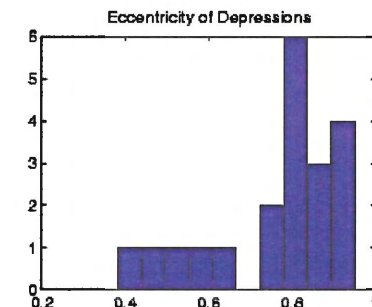
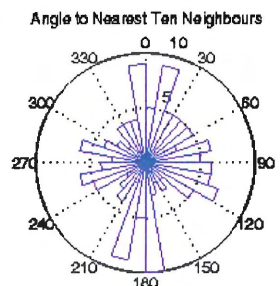
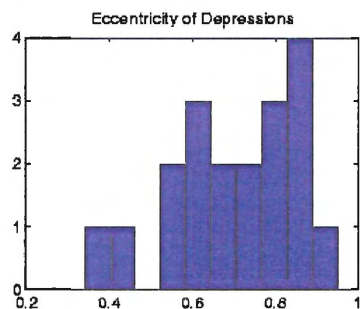
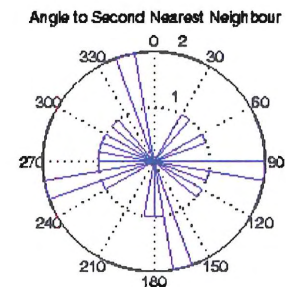
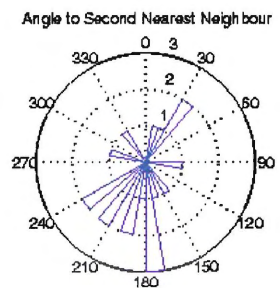
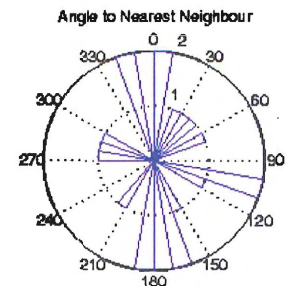
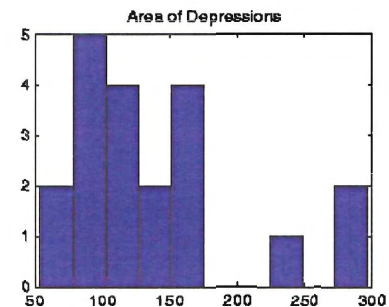
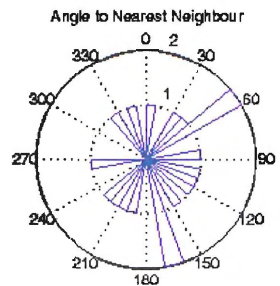
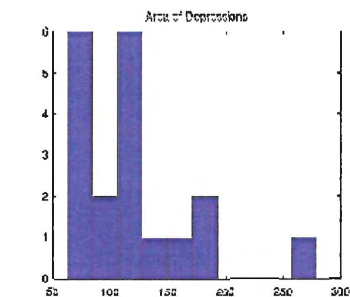


Figure F.7.a: Plots for MOC image M04-00990 model 1, randomly distributed depressions. Distribution histograms of: area of individual depressions (m^2) and eccentricity of depressions (after Friend and Sinha, 1993). Roseplots of: angle to nearest neighbour, angle to second nearest neighbour and angle to the ten nearest neighbours of every depression.

Figure F.7.b: Plots for MOC image M04-00990 model 2, random distribution of depressions along a polygonal network. Distribution histograms of: area of individual depressions (m^2) and eccentricity of depressions (after Friend and Sinha, 1993). Roseplots of: angle to nearest neighbour, angle to second nearest neighbour and angle to the ten nearest neighbours of every depression.